Doctoral theses at NTNU, 2017:331

Espen Vinge Fanavoll

Microfluidic flow cells for the analysis of electrocatalytic reactions

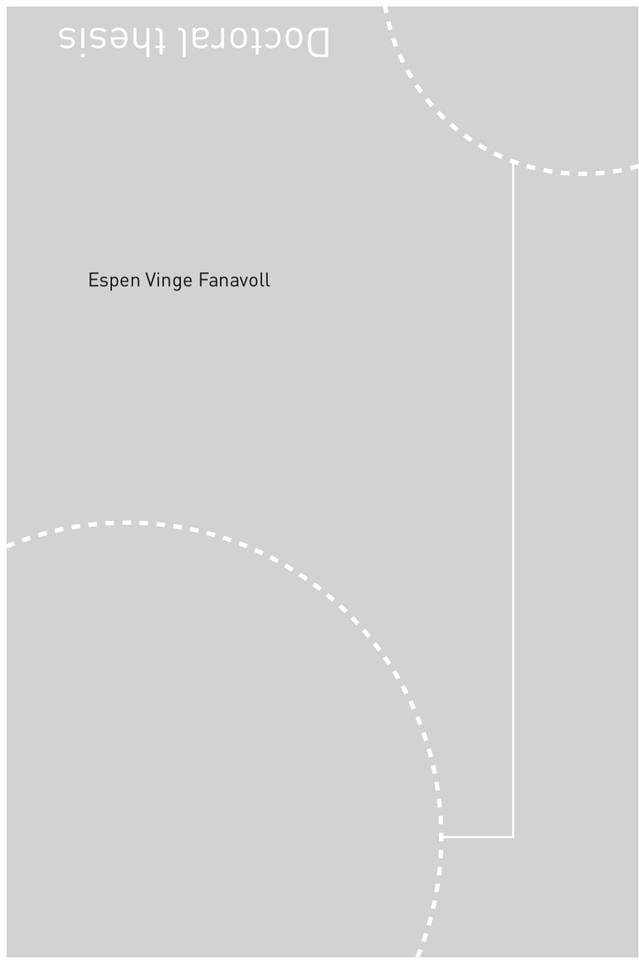

ISBN 978-82-326-2730-1 (printed ver.)
ISBN 978-82-326-2731-8 (electronic ver.)
ISSN 1503-8181

NTNU
Norwegian University of
Science and Technology

NTNU
Norwegian University of Science and Technology
Thesis for the Degree of
Philosophiae Doctor
Faculty of Natural Sciences
Department of Materials Science and
Engineering

Doctoral theses at NTNU, 2017:331

NTNU
Norwegian University of
Science and Technology

Espen Vinge Fanavoll

Microfluidic flow cells for the analysis of electrocatalytic reactions

Thesis for the Degree of Philosophiae Doctor

Trondheim, December 2017

Norwegian University of Science and Technology
Faculty of Natural Sciences
Department of Materials Science and Engineering

NTNU
Norwegian University of
Science and Technology

NTNU
Norwegian University of Science and Technology

Thesis for the Degree of Philosophiae Doctor

Faculty of Natural Sciences
Department of Materials Science and Engineering

ISBN 978-82-326-2730-1 (printed ver.)
ISBN 978-82-326-2731-8 (electronic ver.)
ISSN 1503-8181

Doctoral theses at NTNU, 2017:331

Printed by NTNU Grafisk senter

Preface

This thesis is the result of research work performed during my PhD program at the Department of Materials Science and Engineering at the Norwegian University of Science and Technology (NTNU) from 2013 to 2017. This includes a four month research stay at the Department of Chemistry at the University of Victoria (UVic) in BC, Canada during the spring of 2015. The project was funded by the Research Council of Norway (221899). The Research Council is also acknowledged for the support to the Norwegian Micro- and Nano-Fabrication Facility, NorFab (245963).

All experimental work in this thesis, including fabrication of microfluidic cells, was performed by me. David A. Harrington, Svein Sunde, Frode Seland and Gurvinder Singh have made contributions to the planning and writing. Part of this work is published in Electrochimica Acta [1], and is presented here in chapters 5 and 6. The text and figures were modified for this thesis to make the chapters stand-alone.

Acknowledgements

First of all I would like to thank my main supervisor Svein Sunde and co-supervisor Frode Seland for giving me this opportunity. You have both been great mentors, providing the ideas, insights and discussions that made this thesis possible.

I would also like to thank my co-supervisor David A. Harrington for his invaluable contributions in both the planning and the writing of this thesis, and for allowing me to run loose in his lab at UVic for a semester.

I want to thank the technical and administrative staff at the Department of Materials Science and Engineering, as well as NanoLab. You are all great enablers that deserve credit for the research that is done here at NTNU. Special thanks to Magnus Følstad for maintaining order in the electrochemical labs.

I would like to thank Thomas Holm and Mats Ingdal, who made significant contributions to the developments in the fabrication of microfluidic flow cells and the electrochemical setup in the beginning phase of this project.

To all my co-workers at the department. DoktorandØL drinkers, BergLan players and secret santas. The social community at this department plays a big part in making a PhD worth doing.

To my parents, Torun and Stein. Thank you for always supporting me.

Trondheim, 08. November 2017

Espen Vinge Fanavoll

Summary

The electro-oxidation of small organic molecules such as methanol could play an important role in the transition from fossil fuels to renewable energy sources. For real applications the direct methanol fuel cell has been limited by the sluggish reactions, limited durability and high cost, and further development is needed for the DMFC to be cost-effective compared to other technologies.

Microfluidic flow cells are flow cells that can manipulate small volumes of fluids, and typically have channel dimensions on the micrometer scale. The microfluidic flow cell could be a very useful tool in the investigations of electrochemical reactions. While microfluidic flow cells have been extensively used in other fields of research, such as biology and analytical chemistry, their application in the electroanalytical toolbox has so far been limited. The attractive features of performing electrochemical experiments in a microchannel is that the laminar flow profile gives well-described mass transport processes, the ability to work with very small electrolyte volumes, and the ability to switch between electrolytes much faster than conventional cells.

In this thesis we demonstrate a method to reproducibly fabricate microfluidic flow electrochemical cells with high quality noble metal thin-film electrodes using photolithographic methods. The flexibility of these methods means that a cell design can go from concept to fully operational cell in less than a week. The design of the electrodes can be tailored for different mass transport properties, such as high collection efficiency and fast mass transit between electrodes. Working-sense electrode mass transit times, i.e. the time it takes for a species produced at the working electrode to reach the downstream sense electrode, down to 3 ms were demonstrated.

The integrated palladium hydride thin-film electrode is demonstrated to be a suitable reference electrode for the microfluidic electrodynamics cell. Fabricated by the same method as the other thin-film electrodes and charged in situ, the main advantages of this reference electrode are the simplicity of the design and operation and that it does not contaminate the analyte. While the longevity of the PdH reference electrode is lower than the conventional alternatives, it was found to provide stable potentials for at least 5 hours. This, and the ability to recharge the electrode in a short time, means that it was suitable for all the electrochemical measurements in this thesis. Being able to place the reference electrode upstream of the other electrodes meant that the

potential distribution in the microchannel, which was found to be a problem when using an external reference electrode, could be much better managed.

A reduction of the width of the electrodes and the distance between them resulted in short transit times, and enabled novel measurement techniques to be attempted. By applying a periodic perturbation at the working electrode, the same signal could be detected and isolated at the sense electrode through the changes in the concentration of the species. This method may have the potential to be developed further to filter out both periodic and steady noise from the target signal.

The microfluidic flow electrochemical cell was applied to the study of the methanol oxidation reaction through measurement of the soluble intermediates formic acid and formaldehyde, using an electrode design with a platinum working electrode located upstream of a palladium sense electrode. First, the oxidation reactions of formic acid and formaldehyde on palladium were investigated, with the goal of using this electrode for in situ quantitative measurements. Palladium does not oxidize methanol in acidic electrolytes, and is a good catalyst for formic acid oxidation. Using a fast potential step technique, oxidation of formic acid at rates close to the mass transport limited rate, with negligible contribution to the current from formaldehyde, were demonstrated. This technique was then applied to in situ measurement of formic acid released from the upstream platinum electrode, showing that a substantial fraction of the methanol oxidized at the smooth Pt electrode is released downstream as formic acid.

Table of Contents

Symbols and abbreviations

Abbreviations

CA	Chronoamperometry
CE	Counter electrode
CP	Chronopotentiometry
CV	Cyclic voltammetry
DMFC	Direct methanol fuel cell
FEP	Fluorinated ethylene propylene
MFFC	Microfluidic flow cell
MOR	Methanol oxidation reaction
OCP	Open circuit potential
ORR	Oxygen reduction reaction
PDMS	Polydimethylsiloxane
PE	Polyethylene
PEEK	Polyether ether ketone
PFA	Perfluoroalkoxy alkane
PP	Polypropylene
PTFE	Polytetrafluoroethylene
RE	Reference electrode
RHE	Reversible hydrogen electrode
SE	Sensing electrode

WE	Working electrode	

Greek letters

δ_{resist}	Photoresist film thickness	m
η	Dynamic viscosity	Pa s
ν	Kinematic viscosity	m^2/s
ν	Potentiodynamic scanrate	V/s
ρ	Electrolyte resistivity	$\Omega\,\text{m}$
Φ_{sol}	Solution potential	V

Latin letters

Pe	Peclet number	
Re	Reynolds number	
A	Microchannel cross-section	m^2
c	Concentration	mol/L
D	Diffusion coefficient	m^2/s
d	Electrode gap (edge-to-edge)	m
d_{c}	Electrode gap (center-to-center)	m
D_{H}	Hydraulic diameter	m
E	Electrode potential	V
E^0	Standard reduction potential	V
E_{p}	Peak potential	V
$E_{1/2}$	Half-wave potential	V
F	Faraday constant	96 485 C/mol
h_{ch}	Channel height	m
I	Current	A
I_{lim}	Mass transport limited current	A
I_{pre}	Conditioning current	A

I_p	Peak current	A
I_{step}	Current step	A
L_0	Hydraulic characteristic length	m
L_E	Hydraulic entrance length	m
N	Collection efficiency	
n	Cycle number	
p	Pressure	Pa
Q	Volumetric flow rate	m^3/s
R_{hyd}	Hydraulic resistance	$Pa\,s/m^3$
v	Fluid velocity	m/s
v_{av}	Average fluid velocity	m/s
v_{max}	Maximum fluid velocity	m/s
w_{ch}	Channel width	m
w_{el}	Electrode width	m

Chapter 1
Introduction

1.1 Energy storage

The transition to clean and sustainable energy sources is possibly the greatest challenge facing modern society. Most of the world's energy demand is currently provided by fossil fuels such as coal, petroleum and natural gas, which are of limited quantity, non-renewable, and have been utilized at a great cost to the environment and climate. The energy demands of the future will need to be covered by renewable energy sources such as solar, hydroelectric, wind, geothermal and biomass, as well as nuclear energy.

Using renewable energy sources comes with a new set of challenges in terms of energy storage. The conversion to usable energy typically requires large scale installations, or is often intermittent. This means that there is a demand to store and transport the energy to *where* and *when* it is being used. The methods used to store energy are generally either mechanical or chemical. Examples of mechanical energy storage are flywheels, where the energy is stored as kinetic energy, and pumped hydroelectric storage, where the energy is stored as gravitational potential of water in a reservoir. In chemical energy storage, the energy is stored in the molecular bonds and electrochemical potentials of molecules.

Petroleum based fuels and the internal combustion engine have dominated the automotive sector completely since its development more than a century ago. This is despite the fact that combustion engines are not very energy efficient, with less than a quarter of the chemical energy stored in the fuel actually being converted to useful kinetic energy [2]. Electrochemical energy conversion devices such as fuel cells, supercapacitors and batteries combined with an electric motor represent alternative ways of converting chemical energy stored in fuels to vehicle propulsion, and are the main candidates to pave the way for renewable energy to replace fossil fuels [3]. These different energy conversion devices have different advantages and disadvantages. Supercapac-

itors have a high efficiency, can deliver a lot of power and are very stable over many charge/discharge cycles, but are limited in terms of storage capacity and discharge over longer periods of time. Rechargeable batteries also have good efficiency, good stability and high storage capacity, but are ultimately limited by the size and weight of the system as the capacity increases. Fuel cells have the *potential* to replace or complement batteries as a mobile energy source. The energy storage capacity of fuel cells is more scalable, as the fuel cells and storage are separate. The power supplied by the fuel cell scales with the available electrode area, while the capacity scales with the volume of the fuel. The real application of fuel cells have been limited by their low durability, sluggish electrochemical reactions involved leading to much lower efficiencies and the cost requirement to compete with existing technologies.

Batteries are definitely the most mature technology, and the development of battery powered electric vehicles with improved range has led to them taking an increasing share of the new car market. Fuel cells generally need more research and development to become a reliable alternative in this sector.

1.1.1 Fuel cells

The fuel cell is an electrochemical cell where the oxidant and the reductant are continuously fed to the cathode and anode of the cell, converting chemical energy in reactant molecules to electrical energy powering an external circuit. The anode and cathode compartments are separated by an electrolyte, which selectively allows ions to travel while preventing electrical contact and fuel crossover. Figure 1.1 shows a schematic of one type of cell, the direct methanol fuel cell.

Different types of fuel cells are characterized by the electrolytes and fuels used, and there is a large range of device sizes and operation conditions [4]. The most common fuel is hydrogen gas, which can be generated electrochemically from water splitting or from hydrocarbons. H_2 has an excellent gravimetric energy density but poor volumetric energy density, even when heavily compressed. Hydrogen is used commercially in fuel cells ranging from small scale polymer electrolyte membrane fuel cells (PEMFC) at relatively low temperatures, to large scale solid oxide fuel cells (SOFC) operating at temperatures up to 1000 °C. One of the advantages of the higher temperature fuel cells is that they are relatively efficient without requiring expensive noble metals to catalyze the reaction. The elevated temperatures introduces some new challenges for the material selection, and is more suited for stationary grid level energy storage than transportation.

The direct methanol fuel cell (DMFC) is a variation of the PEMFC using methanol as the fuel instead of hydrogen. It should be distinguished from the reformed methanol fuel cell (RMFC) in that the methanol is used directly in the electrochemical reaction instead of reformed to hydrogen. Methanol has a higher volumetric energy density than hydrogen, solving some of the storage

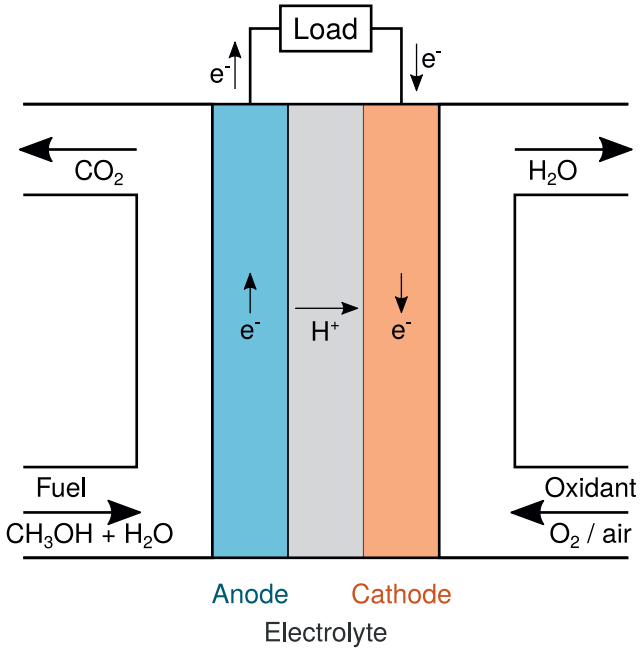

Figure 1.1: Schematic of the direct methanol fuel cell.

issues with the latter.

In the carbon neutral energy economy, methanol could be produced from biomass. In the case of energy abundance, methanol can also be produced by conversion of CO_2 from air using electrochemically generated hydrogen [5, 6].

Another noteworthy type of fuel cells are the redox flow batteries. Instead of hydrogen or hydrocarbon based primary fuels, these use secondary fuels, typically two redox couples such as VO_2^+/VO^{2+} and V^{3+}/V^{2+}, which are electrochemically generated and used in the same manner as a rechargeable battery, but with the increased scalability that is inherent to fuel cells.

1.1.2 Methanol oxidation

The total reaction for the direct methanol fuel cell is given below [7, 8]. Methanol and water are fed to the anode, where it is ultimately oxidized to CO_2 in the methanol oxidation reaction (MOR), releasing six electrons to the external circuit and six protons to be transported through the electrolyte to the cathode side of the cell. The fundamental reaction steps of the MOR is shown in figure 1.2. At the cathode, oxygen gas combines with the protons to form water in the oxygen reduction reaction (ORR).

$$\text{Total :} \quad CH_3OH + \frac{3}{2}O_2 \longrightarrow CO_2 + 2H_2O \qquad E^0_{\text{cell}} = 1.21\,\text{V} \quad (1.1)$$

$$\text{Anode :} \quad CH_3OH + H_2O \longrightarrow CO_2 + 6H^+ + 6e^- \qquad E^0 = 0.02\,\text{V} \quad (1.2)$$

$$\text{Cathode :} \quad O_2 + 4H^+ + 4e^- \longrightarrow 2H_2O \qquad E^0 = 1.23\,\text{V} \quad (1.3)$$

The methanol oxidation reaction has been extensively studied [9–11] by various in situ and ex situ methods such as infrared spectroscopy [12, 13], thermal desorption mass spectrometry [14] and differential electrochemical mass spectrometry (DEMS) [15, 16].

While methanol is the simplest alcohol, the process to oxidize it to CO_2 involves the transfer of 6 electrons, which complicates the reaction mechanism and leads to the existence of various partially oxidized solution and surface species. At least two reaction pathways are known to be active on platinum, and the generation of formaldehyde and formic acid, as well as adsorbed CO, have been measured. CO is known as to adsorb strongly and act as a poison to the Pt electrode. Complete oxidation of methanol to CO_2 (or to formic acid) requires a source of oxygen, as the CH_3OH molecule only contains one. Consequently, the surface activity of water and OH plays a key role in the reaction mechanism [11].

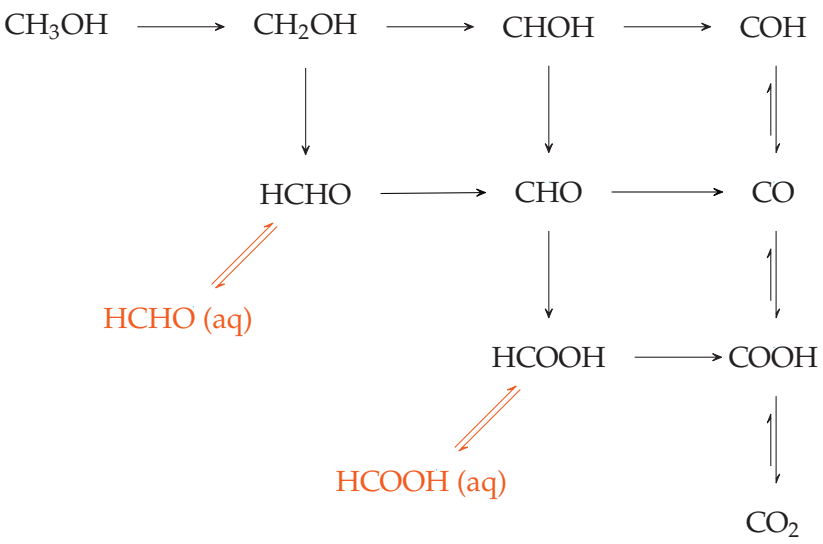

Figure 1.2: Fundamental steps in the oxidation of methanol to CO_2. The steps to the right are dehydrogenation steps, while steps down involve oxidation of the carbon atom. Adapted from the Bagotzky mechanism [17].

Formic acid also has a known homogeneous reaction with methanol forming methyl formate, though this reaction is slow, and later findings argue

that methyl formate is instead formed during the catalytic reaction on the Pt surface [18].

The simplified scheme of the reaction steps is shown in figure 1.2, adapted from the Bagotzky mechanism [17], where the steps to the right involve dehydrogenation and the steps downward are oxidation steps. The species along the hypotenuse, i.e. formaldehyde (HCHO) and formic acid (HCOOH) are stable and soluble, and may be transported away from the electrode before they are oxidized further. On a smooth electrode under flow there is a chance for the molecule to return to the same electrode at a downstream point, or be swept further downstream. While this is a faradaic loss, it may also serve as a window into the reaction taking place at the electrode surface.

Studying the methanol oxidation reaction through the soluble intermediates at different conditions and catalysts should give an increased understanding of the process, and aid in the logical development of new electrocatalysts.

1.2 Microfluidic flow cells

Microfluidics is a rapidly expanding cross-disciplinary field of research. The defining feature of microfluidic devices is that liquids are manipulated in very small volumes, where at least one of the dimensions are on the sub-millimeter scale. The main advantage of working with fluids at this scale is that the flow is laminar, and may thus be manipulated in a predictable way. This means that the functionality of several laboratory instruments can fit into one "Lab on a chip", in which the species in the fluid are manipulated and analyzed in situ.

The introduction and development of microfluidic systems was mainly driven forwards by the fields of analytical chemistry and biology [19], using photolithographic fabrication methods borrowed from microelectronics and microelectromechanical systems. The possibilities for parallelization and automation within lab on a chip systems are vast, and the devices may include both pumping systems [20–22] and valves [23–25] on the chip itself. The size of components in a microfluidic device range from the millimeter scale to tens of nanometers.

More recently the coupling between electrochemical methods and microfluidics has been of particular interest, especially for applications in the energy sector [26]. The laminar flow in the microchannel means that there is very low mixing in the directions normal to the fluid flow. This has been utilized in membraneless fuel cells, which use multi-stream laminar flow to separate the reductant from the oxidant, and eliminate the need for a solid electrolyte membrane or separator [27]. Microfluidic fuel cells have been investigated both with primary fuels such as hydrogen, methanol and formic acid [28–30] as well as secondary fuels such as the vanadium redox couples [31–33].

Other applications of electrochemical microfluidic devices include biosensors [34–37], velocimetry [38, 39], electrosynthesis [40–42], water treatment [43,

44], fuel reformers [45], CO_2 conversion [46] and recently, investigations of electrocatalytic reactions [47–49].

Microfluidic devices have the potential to be a valuable addition to the electrochemistry toolbox. Key advantages include highly controllable and well described convective mass transport conditions, the ability to work with electrolyte volumes below 1 mL, and the ability to rapidly switch the electrolyte using microchannels with multiple inlets. The cells can be designed to include several downstream microband electrodes for detection of soluble reaction products and intermediates. Microfluidic cells can be rapidly prototyped using photolithography and metal evaporation techniques, supporting cell designs with micron-level precision, and multiple electrodes of different composition. Deposition of catalyst particles on the microband electrodes is also possible, enabling the study of electrocatalytic reactions in these kinds of cells.

Compared to the conventional electrochemical cells with rotating ring-disk electrodes, microfluidic cells offer a greater range of mass transport rates [47], as well as the ability to customize the cell geometry towards the desired properties, such as high collection efficiencies and/or very fast mass transport to and between multiple electrodes. The microfluidic cell also does not recycle the oxidation products back into the analyte solution. The main challenge with electrochemical experiments in microchannels is the ohmic resistance due to the restricted volume.

1.3 Aim of thesis

The aim of this thesis can be summarized in two main points:

1. Develop the microfluidic electrochemical cell as an alternative to conventional cells for investigations of aqueous electrochemical reactions.
    - Utilize the facilities available at NTNU NanoLab to fabricate microfluidic flow cells with high quality noble metal electrodes and with high fabrication yield.
    - Tackle the challenge of potential distribution and reference electrode placement in the microchannel.
    - Investigate the influence of the experimental setup on the electrochemical measurements.
    - Demonstrate the properties and capabilities of microfluidic electrochemical cells, particularly in terms of mass transport, using a reversible model system.
2. Investigate the methanol oxidation reaction on platinum through electrochemical measurement of the reaction products, using the microfluidic electrochemical cell as a generator-sensor setup.

1.4 Outline of thesis

This thesis is written as a monograph. The chapters are self-contained, and knowledge of the previous chapters is recommended, but not required. The thesis is divided into two parts reflecting the aim of thesis, Part I (chapters 3 to 7) and Part II (chapters 8 and 9).

This chapter has served as an introduction to the two topics of methanol oxidation and microfluidic electrochemical cells, and the motivation and aim for this thesis.

In chapter 2, the fabrication of microfluidic cells is described in detail, including a short discussion on cell design and materials selection. The electrochemical setup for microfluidic flow cells is presented, and the electrochemical techniques used in this thesis are explained. The finer details of the experimental techniques used in the work presented in each chapter are described in a smaller experimental section in each chapter.

Chapter 3 presents the electrochemical characterization of the platinum and palladium microband electrodes by cyclic voltammetry.

In chapter 4 the theory behind the mass transport processes in microchannels is presented and correlated with experimental measurements in microfluidic electrochemical cells. Important parameters such as collection efficiency and transit times are discussed. The effects of the experimental setup and equipment on the mass transport phenomena and electrochemical measurements are discussed.

In chapter 5 the design and implementation of an integrated palladium hydride reference electrode in the microfluidic electrochemical cell is presented.

In chapter 6 the effects of solution resistance in the microchannel is discussed. The placement of the reference electrode in relation to the main electrodes becomes very important when performing electrochemical experiment in a constrained volume. A method to verify the effects causing potential shifts when working with multiple electrodes at moderate to high current densities is presented.

The results of chapters 5 and 6 are published in Electrochimica Acta [1]. The text and figures have been modified for this thesis, in order to make the chapters stand-alone.

Chapter 7 shows how the fast mass transport between microband electrodes may be used to generate and measure alternating concentration profiles, recording separate AC and DC signals through mass transport.

Chapter 8 is a practical investigation of the oxidation of formic acid and formaldehyde on the palladium electrode, with the focus towards application of the palladium sense electrode for analysis of formic acid and formaldehyde released during methanol oxidation.

In chapter 9 the downstream palladium electrode is used for in situ measurement of reaction products released from the methanol oxidation reaction at

the upstream platinum electrode, using fast cyclic voltammetry and potential stepping.

Chapter 2
Experimental methods

2.1 Fabrication of microfluidic flow cells

The fabrication of the microfluidic flow cells was performed in the NorFab NanoLab cleanroom facility at NTNU Trondheim. The facility includes an ISO 5 grade area with equipment for both photolithography and e-beam lithography, as well as physical vapor deposition of materials by e-beam or sputtering, chemical vapor deposition, reactive ion etching and focused ion beam microscopy.

The cells were fabricated from two components: The electrode slide made by lift-off lithography and physical vapor deposition, and the channel slab made by soft lithography. The instruments and chemicals used in the fabrication are listed in tables 2.1 and 2.2.

Table 2.1: Instruments.

Type	Model	Manufacturer
Plasma cleaner	Femto	Diener Electronics
Spin coater		SUSS MicroTec
Mask aligner	MA6	SUSS MicroTec
Maskless aligner	MLA 150	Heidelberg Instruments
E-beam evaporator	Classic 500	Pfeiffer Vacuum
E-beam evaporator	ATC-2200V	AJA International
Profilometer	Dektak 150	Veeco

2.1.1 Electrode fabrication

Standard microscope glass slides (VWR) were used as the substrate for the electrodes. The glass slides were cut in half ($25 \times 35\,\text{mm}$) by scoring them across with a diamond scriber, and then snapping cleanly into two pieces,

Table 2.2: Chemicals.

Type	Name	Manufacturer
Photoresist	ma-N 405	micro resist technology
Photoresist	ma-N 440	micro resist technology
Photoresist	SU-8 2100	Microchem
Photoresist	SU-8 3050	Microchem
Photoresist	SU-8 5	Microchem
Developer	ma-D 331/S	micro resist technology
Developer	ma-D 332/S	micro resist technology
Developer	mr-Dev 600	micro resist technology
Remover	mr-Rem 660	micro resist technology
PDMS base	Sylgard 184	Dow Corning
PDMS curing agent	Sylgard 184	Dow Corning

taking care to avoid damaging the glass surface. The glass slides were then loaded into a stainless steel holder and cleaned in acetone in an ultrasonic bath at medium to high power for 10 minutes. After drying off using a nitrogen gun, the ultrasonic cleaning was repeated in isopropanol. Beyond this point it is important to handle the slides with care to avoid contaminating or scratching the glass surface. After drying the slides in nitrogen, the glass slides were further cleaned using oxygen plasma at 50 W for 10 minutes. For an even more thorough cleaning procedure, a piranha etch (H_2SO_4 and H_2O_2 in a 3:1 ratio) may be used, but this was found to be unnecessary with the cleaning procedure above.

Table 2.3: ma-N photoresist parameters.

Resist	δ_{resist}	ω_{spin}	t_{spin}	T_{softbake}	t_{softbake}	Exposure
ma-N 405	0.5 µm	1000 rpm	30 s	100 °C	1 min	400 mJ/cm^2
ma-N 440	4.1 µm	3000 rpm	30 s	100 °C	4 min	1300 mJ/cm^2

After cleaning, the glass slides were baked at 200 °C for 10 minutes to remove moisture. After cooling down to room temperature, the slides were spin-coated with the negative photoresist. One of two different negative photoresists were used for the electrodes: ma-N 405 and ma-N 440. These are in the same resist series, but with different viscosities giving different thickness in the developed photoresist. Both are well suited for lift-off electrode fabrication due to good adhesion to glass and good thermal properties. The fabrication parameters for the two resists are listed in table 2.3. The ma-N 440 is thicker, and requires longer softbake and a higher exposure dose.

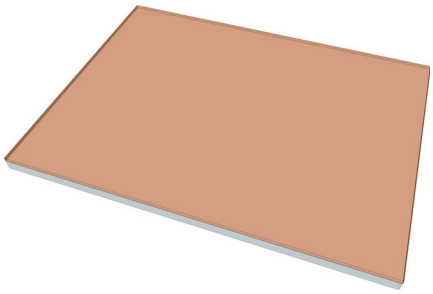

Figure 2.1: Spin coated.

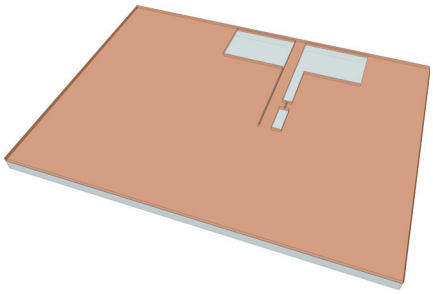

Figure 2.2: Developed.

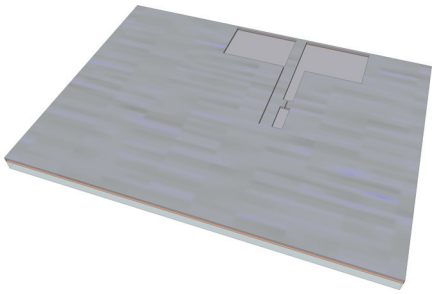

Figure 2.3: Metal deposited.

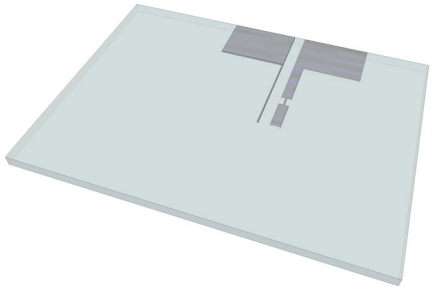

Figure 2.4: Lift off.

After spin-coating, the slides were put on a hotplate to softbake the photoresist. After cooling down to room temperature the photoresist was patterned using either a mask aligner or a maskless aligner. The difference between these are commented on below, in section 2.2. The main principle of these is the same: The photoresist is cross-linked by exposure to UV radiation ($\lambda = 405\,\text{nm}$), and the pattern decides which parts are not exposed and thus not cross-linked. The cross-linked photoresist becomes darker after the exposure, and the pattern should be clearly visible.

The exposed slides were then put in a beaker with the developer (ma-D 332/S for the ma-N 440 resist). This is perhaps the most critical step, and was the main source of low yields and disappointing fabrication results in the early stages of the project. Underdeveloped photoresist would lead to spotty metal deposition, as the metal did not bond properly to the glass. The development time is sensitive to both the strength of the developer and the condition of the photoresist, so the development time stated by the resist manufacturer should be taken as a guideline, not a rule. Slightly different softbake parameters, and also the age of the photoresist may influence the development time. The solution to this was to always monitor the development process. As the non cross-linked photoresist was gradually removed by the developer, the resist thin-film could be monitored by looking at the refraction of light through the film when viewed at the right angle. It was possible to see relatively easily when the last of the resist was removed, leaving clean glass. The resist film was thickest

at the edges, and was thus last removed there. Typical development time was around 2 minutes. After the development was completed, the cells were immediately and carefully rinsed in deionized water for at least 15 seconds, before drying with a nitrogen gun.

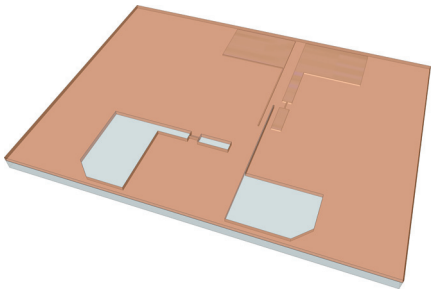

Figure 2.5: Second photoresist layer

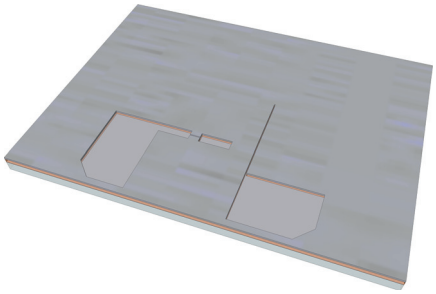

Figure 2.6: Second metal deposition.

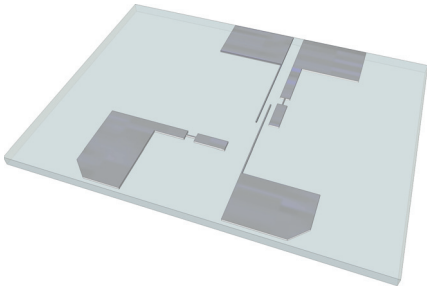

Figure 2.7: Final multi-metal electrode slide.

All slides were inspected using an UV-filtered yellow light microscope after development. If any underdeveloped photoresist was found, the slide was returned to the developer beaker to finish. Slides with defects, such as broken photoresist, particles or other visible damage to the photoresist were disposed of. Before metal deposition, the slides were cleaned in oxygen plasma at 50 W for 5–10 minutes. The slides were mounted to a 4 inch silicon wafer to be loaded into the e-beam evaporator. One wafer had room for 5 electrode slides. A nitrogen gun was used to blow away any potential particles from the glass before deposition.

In the e-beam evaporator, a high voltage (8 kV) electron beam is swept over a source material target to evaporate the target atoms, which are then deposited on the sample (and the walls of the vacuum chamber). The deposition rate is monitored by a quartz crystal microbalance. The metal films were typically deposited at a rate of 5 Å/s, and the sample holder was rotated for even deposition. A 10 nm layer of titanium was always deposited first. Titanium provides good adhesion both to the glass, and to the metals deposited on top of it. Alternatively, chrome may be used for the same effect. The adhesion layer was followed by typically 190 nm of the target electrode metal.

After metal deposition the slides were put in a beaker with a solvent-based remover. This removes all the photoresist along with the excess metal on top of it. The removal process took up to 15 minutes, and was aided by using a small brush. The slides were finished off in clean remover in a separate beaker

to make sure all the photoresist and metal particles were removed, and then rinsed in acetone, dried using nitrogen, and rinsed again in deionized water.

The whole process was repeated to fabricate electrode slides with multiple electrode materials. As long as the slides were thoroughly re-cleaned before the second round, no adverse effects were found by performing the lithography process on the previously metallized slides. When the gap between the electrodes was large enough (i.e. when only the reference electrode needed to be palladium), Kapton tape was used to manually mask off the electrodes, avoiding the second round of photoresist patterning.

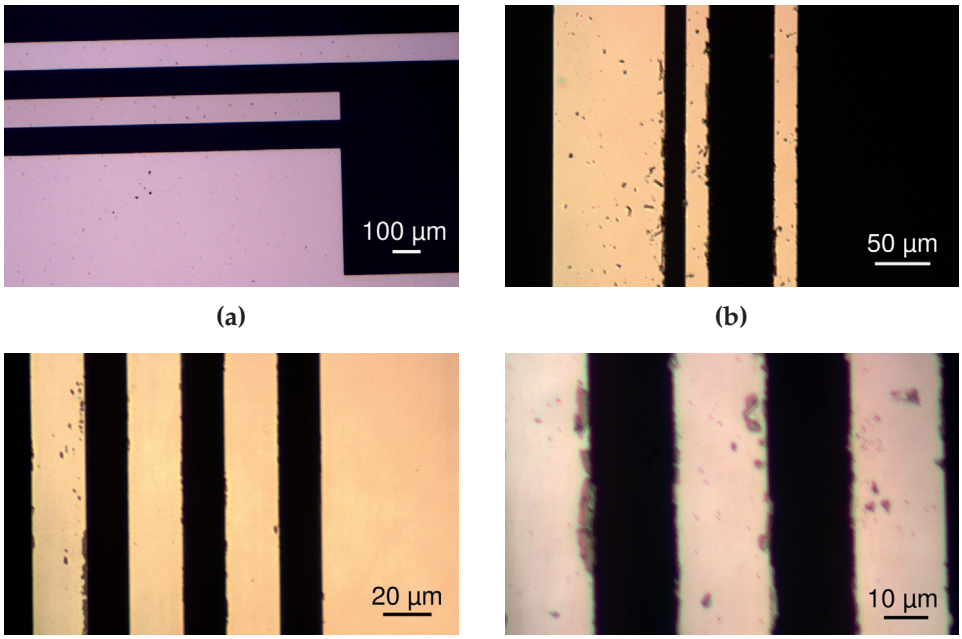

Figure 2.8: Optical microscope images of finished electrode slides. (a) Typical electrode quality. In this case the top electrode is a 100 µm Pt electrode, and the middle is a 100 µm Pd electrode. (b) Redeposited particles on 100 and 20 µm electrodes after lift off process. (c) Good quality 20 µm Pt electrodes. (d) Metal redeposition on 20 µm Pt electrodes.

All slides were examined using an optical microscope to check the integrity and cleanness of the electrodes. Figure 2.8a shows an optical microscope image of the typical electrode quality. A relatively common defect was holes in the electrodes, with sizes ranging from sub micron to the width of the electrodes. These may stem from particles on the slide prior to metallization, but are more likely due to damage or imperfections in the glass surface. Another common defect was redeposition of removed metal particles on the electrodes. Examples of these can be seen in figures 2.8b and 2.8d. Once the electrode slide was dry, these particles were very difficult to remove.

Redeposition of removed metal was found to be especially prominent for gold thin-films. One solution to this was to use scotch tape to remove most of the deposited gold film before the chemical lift-off. The gold thin-film would have stronger adhesion to the tape than the photoresist, and be removed with it, leaving less particles in the remover. However, this requires strong film adhesion to the glass, otherwise the electrodes might be damaged as well.

A profilometer was used to verify the deposited metal thickness. The measured thickness was typically within 10 % of the target thickness.

Electrode slides that did not meet a certain standard of deposition thickness and electrode quality were not used in electrochemical experiments. The electrodes in figures 2.8b and 2.8d are examples of quality below the required standard due to redeposition. However the total yield from fabrication was at least 80 % for electrode slides with critical features at 100 µm and above, and above 50 % for slides with 20 µm features. The electrode slides were finally cleaned in isopropanol in an ultrasonic bath before assembly.

A commonly used optional step to improve the adhesion between the photoresist and the glass is to use a layer of hexamethyldisilazane (HMDS) as an adsorption promoter. This was found not to be necessary for the photoresists used if the steps above, most notably plasma cleaning and dehydration baking before resist coating, were followed.

2.1.2 Channel fabrication

The channels were fabricated by casting PDMS over a channel master, which is a fast, flexible and relatively inexpensive method for fabricating both simple and more complicated patterns. A 2 inch silicon wafer (University Wafer) was used as the substrate for the channel master. The wafer was cleaned in acetone and then isopropanol in an ultrasonic bath in the same manner as described for the glass substrates above. The wafer was then cleaned in oxygen plasma at 50 W for 10 minutes and dehydration baked at 200 °C before spin-coating the photoresist. A nitrogen gun was used to blow off any particles.

Three different SU-8 photoresists were used to make different channel heights. The fabrication parameters for the different resists to make channel heights (h_{ch}) are shown in tables 2.4 and 2.5. In general, thicker resist layers require longer baking time and higher exposure doses. The thicker SU-8 resists needed to be spread on the wafer with a plastic spoon, as they were too viscous to spread by themselves. It was important to do this carefully to avoid creating too many air bubbles in the resist, though some bubbles were unavoidable with the thick resists. The wafer was then ramped at 250 rpm/s to 500 rpm and kept for 10 s before the spin speed was increased to the final spin speed ω_{spin}, where it was held for t_{spin} to obtain the target resist film thickness δ_{resist}.

If there were too many air bubbles in the resist surface after spin-coating, the wafer was cleaned in developer and the process was started again. A few bubbles are acceptable, as long as it is possible to avoid them when aligning the

Table 2.4: SU-8 pre-exposure parameters.

Resist	δ_{resist}	ω_{spin}	t_{spin}	Softbake			
				T_1	t_1	T_2	t_2
SU-8 2100	90 µm	3000 rpm	30 s	65 °C	5 min	95 °C	25 min
SU-8 3050	55 µm	2500 rpm	40 s	65 °C	5 min	95 °C	15 min
SU-8 5	22 µm	1500 rpm	30 s	65 °C	5 min	95 °C	10 min

Table 2.5: SU-8 post-exposure parameters.

Resist	δ_{resist}	Exposure	Post-exposure bake				t_{dev}
			T_1	t_1	T_2	t_2	
SU-8 2100	90 µm	240 mJ/cm	65 °C	5 min	95 °C	10 min	10 min
SU-8 3050	55 µm	200 mJ/cm	65 °C	5 min	95 °C	10 min	10 min
SU-8 5	22 µm	150 mJ/cm	65 °C	5 min	95 °C	5 min	5 min

channel master. The coated wafer was put on a hot plate to softbake the photoresist. Thick photoresist layers like SU-8 require more gradual temperature changes, otherwise the resist layer may lose adhesion to the silicon substrate due to thermal shock. The wafer was first baked for 5 minutes at 65 °C before ramping the hot plate up to 95 °C. After the softbake was completed, the hot plate was turned off and the wafer was slowly cooled to under 40 °C before taking it off the hot plate. The photomask with the channel was aligned to avoid any air bubbles in the cross-linked resist, and the wafer was exposed with the 405 nm lamp.

The exposed pattern was not visible directly after the exposure, but gradually became visible during the post-exposure bake. The same principle as for the softbake was followed, starting at 65 °C before ramping up the temperature, and slowly cooling the wafer down again by leaving it on the hot plate to avoid thermal shock. After reaching room temperature, the wafer was developed in the mr-Dev 600 developer, which removes the non-cross-linked photoresist. It was easy to see when the development was finished, leaving a clean Si surface. The wafer was then rinsed in clean developer, followed by acetone and isopropanol before being blown dry with a nitrogen gun.

The height and uniformity of the channel master was checked using a profilometer. Due to evaporation of the photoresist solvent over time, it can be difficult to get the exact resist film thickness from the specifications of the resist manufacturer, so it is necessary to measure this in order to know the actual channel height. Following the specification for 50 µm thickness gave a final resist thickness of 55 µm one time, and 57 µm the following time.

Figure 2.9 shows the profilometer measurements for the 55 µm channel master used in this work. There is less than 2 µm variation in height along the

whole 2 cm length of the channel, and the cross section is practically uniform.

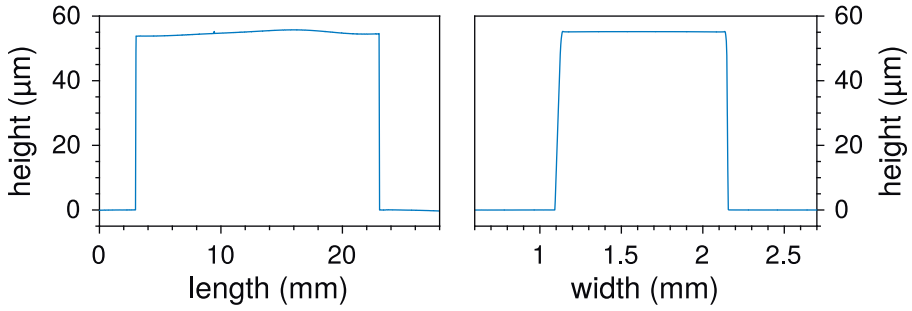

(a) Full length. **(b)** Cross section.

Figure 2.9: Profilometer measurements of the height of a 55 µm SU-8 channel master.

An optional step to increase adhesion between the SU-8 and the substrate is to use an adhesion layer of thinner resist, typically SU-8 2, which is softbaked, exposed, and post-exposure baked before spinning the final resist. This was not found to be strictly necessary, as the single layer SU-8/silicon channel masters were mechanically robust and could be used repeatedly without damage.

The channel slab itself was made of polydimethylsiloxane (PDMS). Uncured PDMS will easily spread and contaminate other samples and equipment, so all PDMS work was done in a designated fume hood within the cleanroom. The polymer base and curing agent were mixed in a 10:1 ratio and stirred for at least 1 minute to homogenize the mixture. The PDMS mixture was then degassed under vacuum for 30 minutes or until most of the air bubbles were gone. About 15 g of the mixture was poured over the 2 inch master wafer. The PDMS was then degassed again for at least 40 minutes to remove all air bubbles before curing at 80 °C for 40 minutes. The cured polymer was cut into the final channel slab, and holes for the electrolyte inlets and outlet were made using a hole puncher from the channel side of the slab. The diameter of the hole puncher used was slightly smaller than the outer diameter of the inlet tubing, and the holes were made as straight and clean as possible, to make sure PDMS and inlet tubing would seal properly. For the 1⁄16 inch (1.59 mm) OD inlet tubing, a 1.25 mm hole puncher was used.

2.1.3 Assembly

The finished PDMS slab was thoroughly cleaned of any PDMS or dust particles using scotch tape. Both the electrode slide and the PDMS slab were put in the plasma cleaner for 24 s at 50 W and oxygen flow. This activates the PDMS surface, allowing a strong bond to the glass. The PDMS slab and electrode slide were quickly joined within 1 minute of activation, making sure the channel was

placed accurately over the electrodes according to the design. This treatment was typically found to create a partial irreversible bond between the two parts, and attempting to peel off or realign the channel slab would rip the PDMS apart leaving pieces attached to the surface. The joined cell was baked at 80 °C for at least 20 minutes to complete the bonding. After the bake, the whole PDMS slab was found to be irreversibly bonded to the glass, and any effort short of treatment with concentrated sulfuric acid would not remove the PDMS from the glass. The PDMS did not bond irreversibly to the metal.

Tin plated copper wire was soldered to the electrode contact plates using lead-free solder. A scalpel blade was used to scratch the surface of the contact plates to improve the wetting between the solder and the electrode metal, and the contact plates were tinned with a small amount of solder before making a solder ball, in order to achieve a durable solder joint. Palladium and gold contact plates were more difficult to solder than palladium as the thin-film would quickly alloy with the tin, and care was taken not to melt the thin-film off the glass slide.

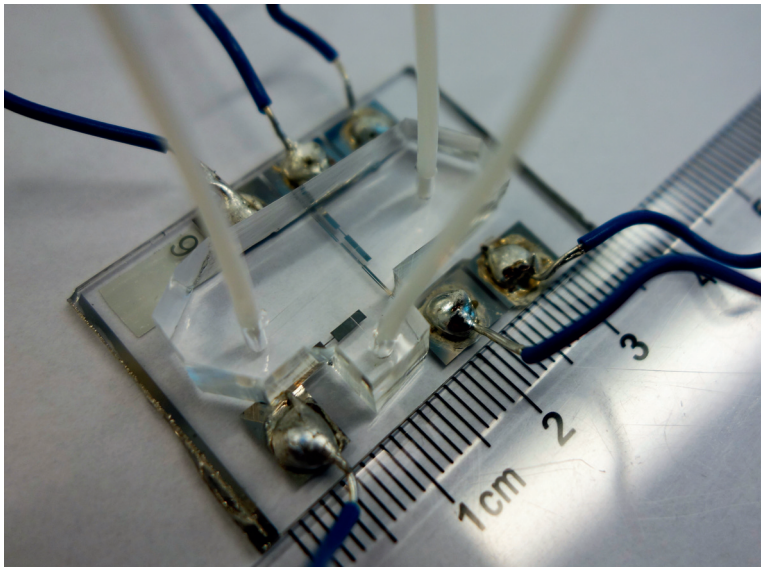

Figure 2.10: Assembled 6-electrode microfluidic cell. At this scale the four working electrodes ($3 \times 20\,\mu m$ and $1 \times 100\,\mu m$) are not individually distinguishable.

PTFE microbore tubing (e.g. 1/16 inch OD - 1/32 inch ID, Elveflow) was cut to appropriate lengths with a scalpel blade, and used for the electrolyte inlets and outlet. It is important to consider the tube size, as it represents almost all of the dead volume in the microfluidic cell. Isopropanol was used to lubricate the insertion, to avoid the PDMS cracking. No silicone was required to seal the connection, as the PDMS formed a good seal with the slightly larger PTFE tubing. The cell was baked at 60 to 80 °C to evaporate the IPA, and the standard cleaning procedure (see section 2.3.1) was run before the cells were used.

2.2 Cell design

The fabrication of microfludic electrochemical cells begins with drawing the cell design in CAD software, such as AutoCAD (Autodesk). Figure 2.11 shows an example of a finished microfluidic cell design, including the size of the glass slide and an overlay of the channel. The functional area, where the electrodes intersect with the channel, includes some leeway to make aligning the channel slab and electrode slide easier.

The geometric size of the electrodes are determined by the channel width and the width of the electrode. The lower limit of electrode sizes was found to be mostly determined by the size of defects after fabrication. Electrode widths of 10 µm, or even smaller, are available with acceptable yields. For smaller features, increasing the substrate quality and preventing metal redeposition should be looked into. There is also an upper limit to the electrode sizes that can be functionally used. This is an effect of the solution resistance, and is further discussed in section 3.3.3. As a rule of thumb, electrode widths should not be larger than 4 times the height of the channel for electrodes used as the working electrode in potentiodynamic experiments.

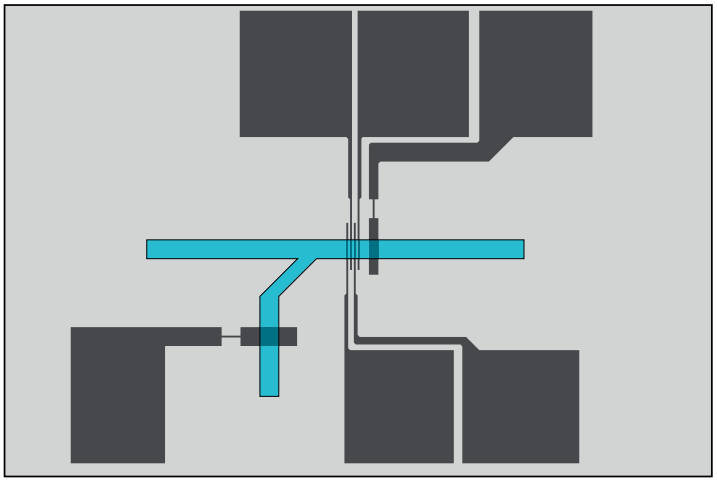

Figure 2.11: Microfluidic cell design as drawn to scale in AutoCAD. This cell includes four 100 µm working electrodes, a 500 µm counter electrode and a 1 mm reference electrode in a branched channel. Channel width 1 mm.

Away from the channel, the electrode connector may be widened to reduce the ohmic resistance between the electrode and the contact plate. However, wider metal traces under the PDMS can lead to problems with electrolyte leakage, as the internal pressure in the channel may overcome the relatively weak Van der Waals forces and allow electrolyte to leak out between the metal and PDMS. One solution to this is to restrict a section of the metal

trace close to the functional area of the electrode, as can be seen from the reference and counter electrode in figure 2.11. This significantly increases the pressure required for electrolyte to flow out over those electrodes, while not compromising the conductance too much. For the cells used in this work, all electrode traces wider than 100 µm were restricted down to 100 µm for 1 mm, and no problems with electrolyte leakage were found with those cells.

Fabricating microfluidic electrochemical cells with multiple electrode materials requires some extra consideration in the cell design, as the photolithography and alignment process must be performed twice. When drawing the electrodes for a photomask, the parts must be separated, and alignment crosses are needed to position the electrodes correctly when patterning the electrode slide the second time. An example of this mask design, and the most used design in this work, is shown in figure 2.12. Alignment marks were made by having a target on one layer, and an alignment cross on the other, with a 20 µm gap between the edges of the cross and the target. Alignment marks should be drawn close to, but not obstructing the functional area.

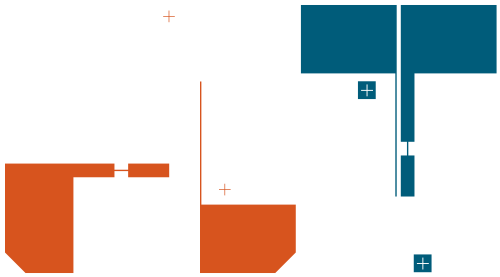

Figure 2.12: Electrode components on photomask. Blue layer with Pt WE and CE, and red layer with Pd RE and SE. Main channel flow direction to the right.

Figure 2.13: Branched and double-branched microchannel designs used in this thesis.

Using the alignment marks, the second layer could be aligned within a few microns of the intended design. A drawback with using photomasks is that there is limited space for different designs on a single mask. Especially when making masks for multiple electrode materials, blank space is needed to prevent overlap between the different designs.

A maskless aligner was acquired by NanoLab in the spring of 2017. This greatly improved the flexibility in the design of electrode slides, as it was no

longer necessary to use a printed photomask. The maskless aligner operates by scanning a laser over the photoresist, turning it on and off rapidly to expose the pattern. To align different layers with the maskless aligner, the different elements should be in different layers in the same CAD file. The alignment marks must then be added by the aligner software, and are automatically detected for the second layer. Using the maskless aligner it is possible to have an assembled microfluidic electrochemical cell ready to use a few days after conceiving the device design.

There is no real limit to how many functional electrodes can be put in the cell. The main limiting factor is the space for contact plates, which in this work were made to be at least 6×6 mm to make it easy to solder a wire, leaving room for maybe 10 contact plates. The metal traces on the electrode slide must also make room for the placement of the channel, with some extra room for easier alignment and enough area to have strong PDMS to glass bonding around the channel.

The microchannels used in this thesis were designed with a 1 mm wide straight main channel, with a branch for the reference electrode, and optionally a secondary electrolyte inlet for the main channel, as seen in figure 2.13.

2.2.1 Electrode materials

A large range of materials are available for deposition by electron beam. The list currently provided by NanoLab is shown in table 2.6. A more extensive list of materials, their properties and their suitability for e-beam evaporation can be found in literature [e.g. 50]. Most suitable materials are pure elements, salts or oxides. It is also possible to deposit alloys, but due to differences in the saturation vapor pressures of the alloy elements, the deposited layer may end up having a different composition than the target [51].

Table 2.6: The materials currently available for e-beam evaporation at NanoLab.

Ag	Al	Au	C	Co	Cr	Cu	Fe	Ge	In	ITO
MgO	Ni	NiFe	Pd	Pt	Si	SiO_2	Ta	Ti	TiO_2	

Structured surfaces, such as cylinders or other shapes may be made from photolithographic methods [52], by using either several deposition steps of the same material, or chemical/physical etching.

It is also possible to perform sputtering instead of e-beam evaporation. In sputtering, the target atoms are physically knocked loose by high energy plasma, to be deposited on the sample. Sputtering is more suitable for alloys, though the deposited layer may still be different in composition from the target, due to differences in the atomic mass of the elements. Sputtering also typically gives a film with more even coverage of steps, so it may be less

suitable for lift-off lithography, and requires control over the resist undercut after development.

A way to modify already deposited electrodes is to use electrochemical deposition. This can be performed both before and after assembly of the cell. One advantage of doing this after assembly is that it is possible to use very small volumes, in the case of prohibitively expensive precursors. Another advantage is that less stable materials may be deposited directly before the measurements, using a branched electrolyte inlet to quickly switch between electrolytes.

When performing electrochemical deposition in the microfluidic cell it is often necessary to protect the other electrodes from contamination. This could be done by keeping them at a passive potential, using the counter electrode or another sacrificial electrode.

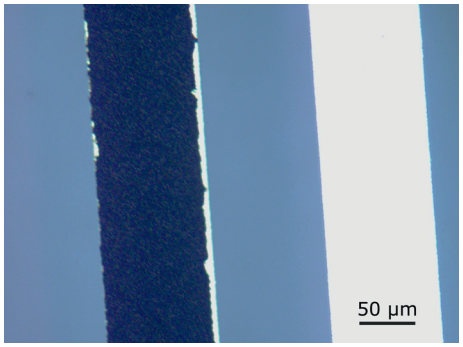

Figure 2.14: Optical microscope image of a Pt/Vulcan catalyst layer deposited on a 100 µm wide Au electrode, next to a clean Au electrode.

Lastly, it is also possible to deposit catalyst particles on the microband electrodes, in the same manner as is done for conventional rotating disk electrodes. A 100 µm wide gold electrode was coated with the ma-N 405 photoresist, and a small section of the electrode was exposed and developed. A catalyst dispersion was made by sonicating a commercial 60 % Pt/Vulcan catalyst in deionized water until the dispersion was stable for at least 30 minutes.

After cleaning the electrode in oxygen plasma, a droplet of the catalyst dispersion was pipetted onto the electrode, spreading evenly over the electrode and the resist. After drying in air, the slide was again cleaned in oxygen plasma. The slide was then carefully put in a beaker with acetone to remove the resist. Using a brush to carefully stir the beaker, the catalyst particles on top of the resist were carefully lifted off as a film, leaving most of the particles on the gold electrode still attached. The slide was then carefully rinsed in isopropanol. The catalyst layer was found to almost completely cover the gold, as seen in the microscope image in figure 2.14. Using a profilometer, the average thickness of the catalyst layer was found to be around 1 µm. The catalyst layer was found to be robust enough to be used at high flow rates in the microfluidic cell. When tested electrochemically by cyclic voltammetry in 0.1 M H_2SO_4, the Pt catalyst showed an electrochemically active area 5 times larger than that of a flat Pt electrode of the same size, with no or little trace of the gold substrate electrode.

This is only a proof of concept for catalyst-covered microband electrodes

for microfluidic cells, and further work is required to obtain a more controlled amount of catalyst, perhaps by self assembly of particles. It may also be possible to make use of different techniques such as screen printing [53, 54] or pyrolysis of carbon-based photoresists [55–57] to make a more electrochemically inert carbon substrate electrode for the catalyst.

2.2.2 Channel materials

In this work PDMS was used to fabricate all the channels. The advantage of PDMS is that it is simple and relatively inexpensive to prototype and fabricate different channel designs. PDMS is optically transparent, compatible with many chemicals, and the irreversible bond to glass after plasma treatment means that the cell is leak-proof at most applicable flow rates. The cured polymer is flexible, so connection to microbore tubing is normally airtight without further modification.

The main downside with using PDMS for electrochemical experiments is the permeability of the polymer. While it is chemically inert to many chemicals, some molecules, especially gases and small organic molecules, are absorbed and may move within the PDMS, and may be released back into the electrolyte at a later time. High concentrations of solvents may also cause swelling. It is possible to modify the permeability of PDMS with surface treatment [58]. While the permeability is one of the attractive properties of some applications of microfluidic cells [19], it is definitely a drawback when it comes to using the cells for electroanalytical purposes.

The most apparent effect of PDMS permeability in the microfluidic electrochemical cells was the electrolyte oxygen content. On noble metal electrodes the reduction of dissolved oxygen is easily seen at lower potentials, and this is the reason electrolytes are purged with an inert gas, and why the PDMS cell would have to be purged as well, before use. An improperly purged PDMS cell would release oxygen into the electrolyte. For a thoroughly purged cell the converse may actually happen, with the PDMS removing trace amounts of oxygen from the electrolyte.

When using electrolytes with small organic molecules, the PDMS became contaminated over time. Continuous experiments with different concentrations were thus started with the lowest concentration and then increased, to avoid the release of species from the channel dominating the actual concentration.

Stripping experiments with rapid (< 1 min) electrolyte changes were found to work well only with lower concentrations, i.e. 1 mM and below. For higher concentrations the clean electrolyte would be contaminated by the species in the previous electrolyte.

Alternative materials for the fabrication of microfluidic cells are available [59, 60], though perhaps none are as easy to fabricate and assemble as PDMS. When selecting an alternative material for the channel part of elec-

trochemical microfluidic cells, there are several properties to be considered. Fabrication of the device should not be prohibitively expensive or difficult. Optical transparency is a large benefit, as it is very useful to be able to see what is going on in the microchannel, especially in regards to trapped gas bubbles in the microchannel. Transparency may also enable combination of the microfluidic electrochemical cell with other in situ techniques such as infrared spectroscopy.

Glass is pretty much the optimal material from an electrochemical standpoint, due to the excellent chemical compatibility and optical transparency. Glass may also be cleaned in aggressive solutions such as fuming sulfuric acid, as is common practice with conventional electrochemical cells. A complete glass cell is more difficult to machine and assemble than PDMS based cells, considering that the custom electrode slide must be bonded with the channel in a manner that does not contaminate the electrodes. There are several commercial suppliers of glass based microfluidic cells.

Fluoropolymers are a popular group of materials for electrochemical applications, which may be used for microfluidic devices as well. A method of fabricating microfluidic devices from perfluoroalkoxy alkane (PFA) or fluorinated ethylene propylene (FEP) using a PDMS master was reported by Ren et al. [61]. PFA and FEP have similar chemical properties to PTFE, but are more optically transparent and may be melt-processed to form the microfluidic devices. PFA/FEP seems to be a suitable replacement for PDMS in microfluidic electrochemical cells.

Another technology to keep an eye on is the development of 3D-printed microfluidic devices [62, 63], which may make fabrication of microfluidic devices more accessible and versatile.

2.3 Electrochemistry

2.3.1 Setup

A Biologic VMP3 multi-channel potentiostat was used for all the electrochemical measurements in this work. The potentiostat is especially suited for multi-electrode experiments, as different techniques can be applied to the different working electrodes completely independently with the same counter and reference electrodes, in the *CE to ground* mode.

Electrolytes were prepared by diluting high quality stock chemicals with Milli-Q (18 MΩ cm) water. Lower concentrations of e.g. formic acid were prepared by preparing lower concentration stock solutions, and diluting controlled amounts using micropipettes. All electrolytes were purged in either nitrogen or argon for at least 30 minutes to remove dissolved oxygen.

Dilute sulfuric acid is a common general purpose acidic electrolyte for electrochemical cells, and is used here in studies of clean surface processes

and experiments with reversible redox species. For experiments involving adsorption of organic molecules there is a rationale behind using perchloric acid, attributed to lower interaction between the anion and noble metal surfaces [64, 65].

Table 2.7: Chemicals used for electrolyte preparation.

Chemical name	**Formula**	**Grade**	**Manufacturer**
Sulfuric acid (98 %)	H_2SO_4	Suprapur	Sigma-Aldrich
Perchloric acid (70 %)	$HClO_4$	Puriss	Sigma-Aldrich
Phosphoric acid (85 %)	H_3PO_4	ACS reag.	Sigma-Aldrich
Monosodium phosphate	NaH_2PO_4	ACS reag.	Merck
Disodium phosphate	Na_2HPO_4	ACS reag.	Merck
Sodium sulfate	Na_2SO_4	ACS reag.	Merck
Tris(2,2'-bipyridyl) ruthenium(II) chloride hexahydrate	$C_{30}H_{24}Cl_2N_6Ru \cdot 6\,H_2O$	99.95%	Sigma-Aldrich
Palladium(II) nitrate dihydrate	$Pd(NO_3)_2 \cdot 2\,H_2O$	$\sim$ 40% Pd	Sigma-Aldrich
Methanol ($\geq$ 99.9)	CH_3OH	Chromasolv	Sigma-Aldrich
Formic acid ($\geq$ 98 %)	HCOOH	Puriss	Sigma-Aldrich
Formaldehyde solution (37 wt.%) cont. methanol	CH_2O	ACS reag.	Sigma-Aldrich

PDMS is oxygen permeable, so it was necessary to keep the microfluidic cell under an inert atmosphere during experiments. A conventional airtight polypropylene/silicone box ($\sim 10 \times 15$ cm, thickness ~ 1 mm) was modified to keep the microfluidic electrochemical cell in an oxygen-free environment, while still providing electrolyte input and connection to the potentiostat (see figure 2.15). The cells were mounted and left in the box under inert gas for at least 4 hours, and sometimes overnight, to remove oxygen from the PDMS. Either argon or nitrogen was used, though in this case nitrogen gas may be more effective at purging the oxygen from the cell, as N_2 is more permeable in PDMS than both O_2 and Ar [66, 67]. The microfluidic flow cells may also be stored in a glove box for a time before use.

A programmable syringe pump (Pump 11 Pico Plus Elite, Harvard Apparatus) was used to control the electrolyte flow in all experiments unless otherwise specified. Glass syringes with PTFE plungers (Gastight 1000 series LT, Hamilton) were the preferred syringes mostly due to low intrusion of oxygen to the electrolyte over time. Disposable PP/PE syringes (Norm-ject, Air-Tite) were found to slowly allow oxygen into the electrolyte, so it is only advisable to use these for short (< 1 h) experiments, or when oxygen in the electrolyte is not critical. The influence of the syringes and pumps on the electrochemical

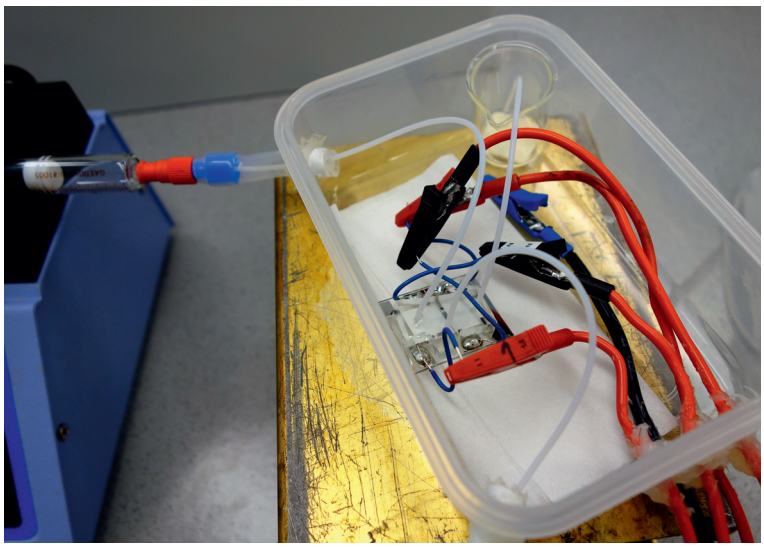

Figure 2.15: Electrochemical setup for microfluidic cells. The main inlet is connected to a syringe in a syringe pump (left), while the reference channel inlet is connected to a free syringe. The inlet tubing is kept inside the purged atmosphere using flexible tubes.

measurements is discussed in section 4.4.1.

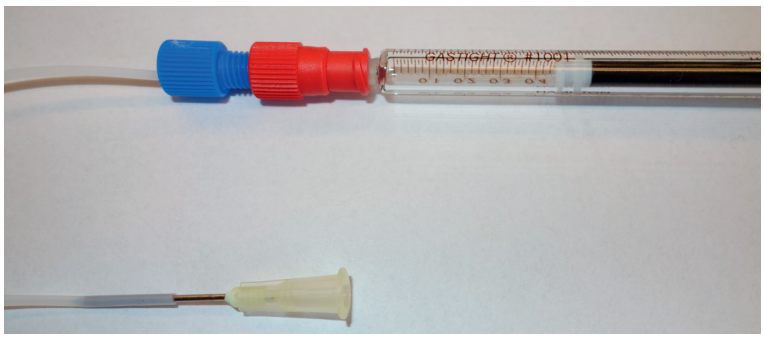

Figure 2.16: Connecting the microfluidic cell to a syringe. Top: microfluidic connectors. Bottom: disposable needle.

The cell inlets were connected to the microfluidic cells using a setup with a PEEK luer adapter to a PTFE ferrule and end connector (Elveflow), as seen in figure 2.16. Alternatively a disposable stainless steel needle (Air-Tite) with a slightly higher gauge than the tubing ID may be used, though this has a larger dead volume than the microfluidic connectors, as well as an increased risk of needle-stick injuries.

Unless otherwise specified, the internal palladium hydride thin-film reference electrode was used for the electrochemical measurements in all following chapters. The properties and usage of this novel reference electrode is dis-

cussed extensively in chapter 5.

At the end of the experiment, as well as after assembly, the microfluidic cell was cleaned by purging with several milliliters of deionized water, typically at a low flow rate overnight. Purging the cell is especially important when working with acids, as they become more concentrated through evaporation of water, and may damage the PDMS. The cell was then purged with air and baked at 65 to 80 °C for at least a few hours or until dry. For a more thorough cleaning isopropanol, or acetone and then isopropanol, was used. The cell would then be baked and purged with water to remove any trace of the organic solvent. Isopropanol is slightly electroactive, and would show up on Pt voltammograms in clean electrolytes.

2.3.2 Electrochemical techniques

In *chronoamperometry* the potential is kept constant while the resulting current is measured, and in *chronopotentiometry* the current is kept constant. These are typically set up as a series of steps from one potential/current to another. This is used to study initial transients and steady state behaviour of electrochemical systems.

Cyclic voltammetry was by far the most used electrochemical technique used in this work. It is a versatile method that can provide much information of the electrochemical system, from characterizing surface processes on electrodes to measuring the reversibility of electroactive species.

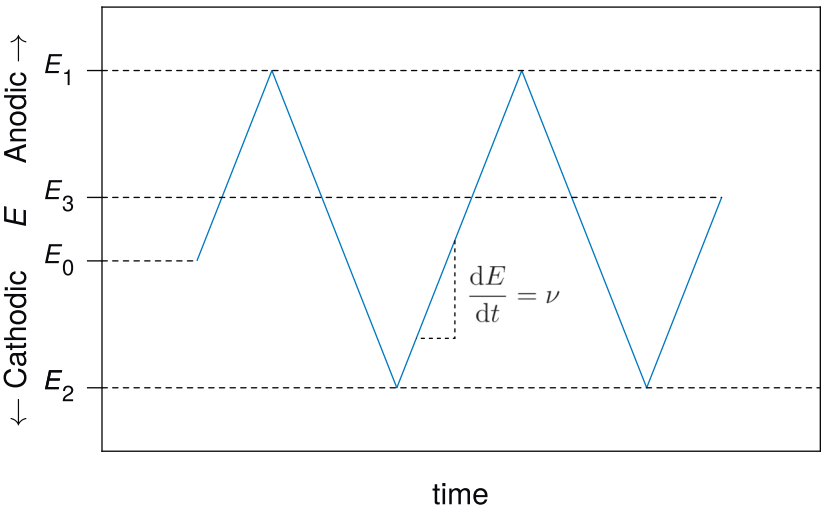

Figure 2.17: Cyclic voltammetry.

An example of the potential-time curve in cyclic voltammetry is shown in figure 2.17. The potential is scanned at a constant scan rate (ν) from a

starting potential (E_0) to an upper vertex potential (E_1) and then down to a lower potential (E_2). This is repeated for a set number of cycles before ending at a final potential (E_3). The definition of the start and end of one cycle is often different for different potentiostats, but here the cycle number (n) increases each time E_0 is passed in the initial scan direction. The scan towards more positive potentials is here referred to as the *forward scan*, and the scan towards more negative potentials is referred to as the *reverse scan*. The initial scan direction may also be in the negative-going direction (i.e. $E_1 < E_2$) but it is still referred to as the reverse scan. The data from cyclic voltammetry is typically plotted as a voltammogram, with the current as a function of the potential.

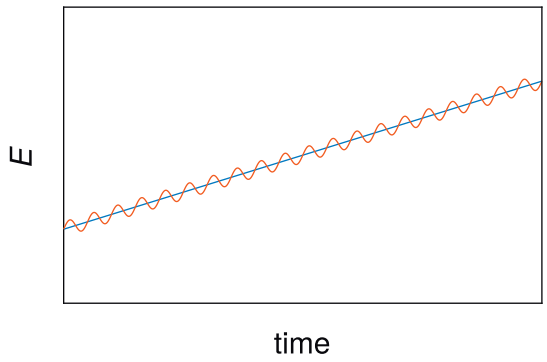

Figure 2.18: AC voltammetry example.

One variation on the linear sweep and cyclic voltammetry techniques is *AC voltammetry*. In this technique, an alternating signal is added to the slow DC potential sweep. The amplitude of the AC signal is usually low compared to the sweep parameters, and the frequency is high compared to the scan rate.

Many digital potentiostats do not have the hardware to provide a true analog potential sweep without further modification, instead the sweep is approximated by a potential "staircase". In the VMP3, the typical potential step is 100 µV. The sampling method thus becomes influential to the measurement. If the potential is measured at the end of each step, the current contribution from capacitive charging may be excluded, and the measured current will be from faradaic processes only. This may however also exclude fast faradaic processes from being measured. The underpotential adsorption/desorption of hydrogen on platinum is a common example of this, and the measured adsorption charge may change depending on the time scale of the potential step and the sampling mode used [68, 69]. In this thesis the current was sampled and averaged over 100 % of the potential step.

2.3.3 Reversible redox couples

For investigations of the mass transport processes in electrochemistry, it is extremely useful to have species that behave *reversibly*, i.e. the rate constant is high. Consider a simple reversible oxidation reaction:

$$\text{Red} \rightleftharpoons \text{Ox} + ne^- \tag{2.1}$$

The concentration of the species at the surface is directly related to the electrode potential by the Nernst equation. At sufficiently high overpotentials, the surface concentration of the reactant is practically zero, and the rate of the reaction is determined only by the mass transport of the reactant to the electrode surface. Reversible couples are often characterized by cyclic voltammetry, as well as by measuring the mass transport limited current at various flow rates.

Finding the right reversible couple was more difficult in practice than in theory. An extensively studied and relatively inexpensive couple is ferri-and ferrocyanide ($Fe(CN)_6^{3-/4-}$). In acidic conditions ferricyanide breaks down, forming toxic hydrogen cyanide as well as Fe^{3+}. Ferrocyanide also reacts with Fe^{3+}, forming the pigment Prussian blue, which was observed in earlier work with microfluidic cells [70]. At pH 7, 5 mM $Fe(CN)_6^{4-}$ was found to behave reversibly on a platinum working electrode, however it was irreversible on the palladium electrode in the same cell, as seen in figure 2.19. This species can not be used with the palladium electrodes that are often featured in this work. In addition the nature of the interaction with palladium is uncertain, and contamination of the internal PdH reference electrode can not be ruled out.

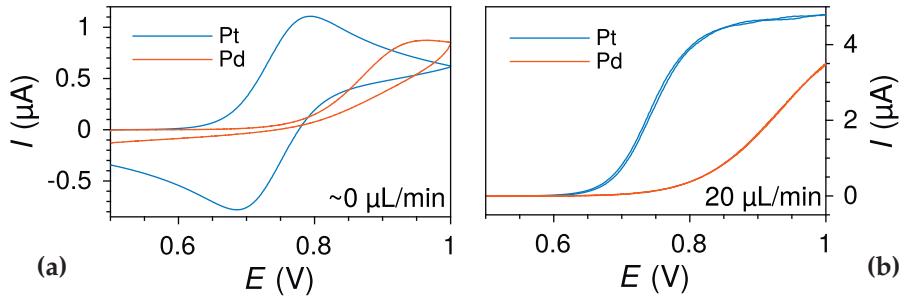

Figure 2.19: Pt and Pd voltammograms in $Fe(CN)_6^{4-}$. Scan rate 100 mV/s. 5 mM $Fe(CN)_6^{4-}$ in a 50 mM phosphate buffer electrolyte at pH 7 with 0.1 M Na_2SO_4.

Another widely used reversible couple is the hexaammineruthenium couple ($Ru(NH_3)_6^{2+/3+}$). This was used with microfluidic cells in the works by Thomas Holm [71, 72]. One major downside with this is that the ruthenium complex degrades in contact with oxygen, which imposes extra difficulties

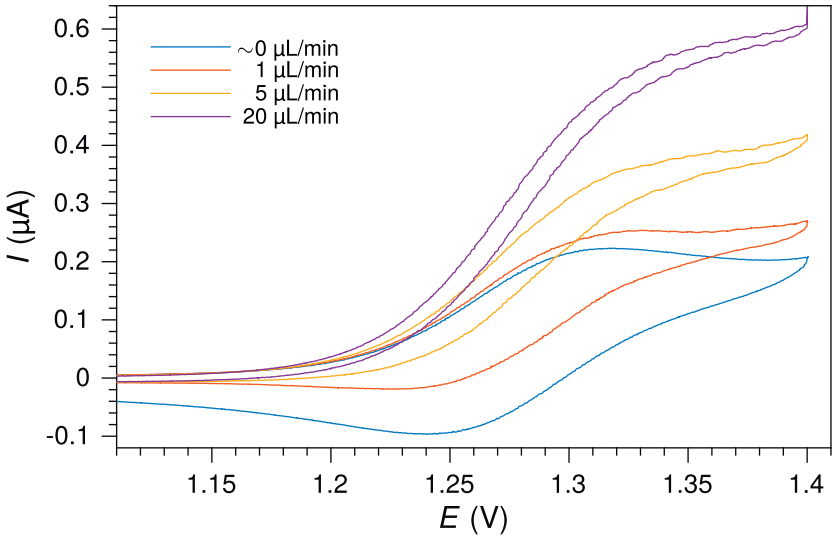

Figure 2.20: Cyclic voltammograms at 100 mV/s on a Pd electrode in 1 mM $Ru(bpy)_3^{2+}$ in 0.1 M H_2SO_4.

with storage and usage of the species. It was difficult to obtain commercially in good quality, with the complex being found degraded at delivery.

$Ru(bpy)_3^{2+}$ is not the most commonly used reversible species in electrochemistry, but it was found to be stable both in dry form and in solution. It was found to behave reversibly on platinum, palladium and gold electrodes, and at pH values from 0.7 to 7 in H_2SO_4 and phosphate buffer electrolytes. It should be noted that it may not be used in $HClO_4$-based electrolytes, as it was found to form an insoluble perchlorate salt.

$Ru(bpy)_3^{2+}$ is oxidized in a single electron transfer reaction at a potential which is in the oxide region of both Pt and Pd[73]:

$$Ru(bpy)_3^{2+} \longrightarrow Ru(bpy)_3^{3+} + e^- \qquad E^0 = 1.24\,V \qquad (2.2)$$

One disadvantage with this species is the relatively high reversible potential. The two previously mentioned species have reversible potentials in the so-called double layer region of the noble metals, where no surface reactions take place. In experiments using $Ru(bpy)_3^{2+}$, the currents from the surface oxide processes can not be eliminated. Fortunately the current in the oxide regions of Pt and Pd are relatively flat. Also, for higher concentrations and slower scan rates the currents from surface processes may become negligible, especially if the electrode is not cycled below the oxide reduction onset potential.

In addition, it should be noted that only one species of the couple, $Ru(bpy)_3^{2+}$, is available commercially, and only as chloride or hexafluorophosphate salts.

Chloride has been found to increase the dissolution of platinum and other noble metals [74], so this species may not be suitable for use with nanoparticle catalysts.

Part I

The microfluidic flow cell as a tool for electrochemical experiments

Chapter 3
Electrode characterization

Abstract

The electrochemical properties of the microfabricated electrodes are examined, especially the surface processes taking place at different potentials in a clean electrolyte. Knowledge of these processes are essential to the investigation of the catalytic properties later in this thesis. In situ measurements of the electrochemically active area of the electrodes are possible, though the accuracy of these methods are not high. The Pt and Pd electrodes were found to behave as expected, though the implementation in a PDMS microfluidic cell seems to limit some of the applications due to absorption of small molecules from the electrolyte.

3.1 Introduction

A common method of characterizing aqueous electrochemical systems with noble metals is to study the surface processes of the metals. This is typically done by cyclic voltammetry in the potential region between oxygen evolution at the anodic side, and hydrogen evolution on the cathodic side. The surface processes are formation and reduction of surface oxide, hydrogen monolayer adsorption and desorption as well as some adsorption and desorption of anions.

When studying electrochemical reactions on these electrodes it is critical to have knowledge on the surface processes on the electrodes, and how these may influence the catalytic activity.

3.2 Experimental

The measurements were performed in microfluidic cells with various electrode materials, fabricated as described in chapter 2. The electrode widths were 100 µm unless otherwise specified, and the thin-film thicknesses were approximately 190 nm. The channel width was 1 mm, making the typical geometric electrode area 1×10^{-3} cm^2.

The electrolytes used were 0.1 M H_2SO_4 or $HClO_4$ and the applied flow rate was 0 µL/min unless otherwise specified. Electrochemical measurements were made using a Biologic VMP3 potentiostat, and potentials are reported with respect to the internal PdH thin-film reference electrode. The details and usage of the PdH reference electrode are discussed in chapter 5.

3.3 Cyclic voltammetry

The channel electrodes were cleaned from organic contamination from solvent residues or PDMS through potential cycling at a relatively high scan rate at the start of the experiments, until stable voltammograms were obtained. The potential cycling also resulted in restructuring the electrode surface, as Pt and Pd atoms move on the surface during formation and reduction of the surface oxides [75, 76].

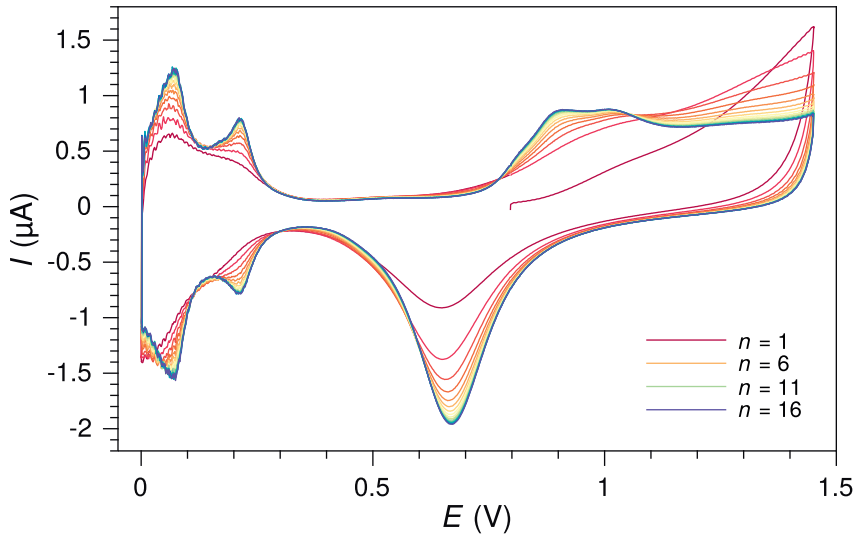

Figure 3.1: Initial cycling at 500 mV/s of a new 100 µm Pt electrode in 0.1 M H_2SO_4. The legend shows the line color for a selection of the cycles.

An example of the initial cycling of a platinum electrode in a previously unused cell is shown in figure 3.1, and the same for palladium is shown

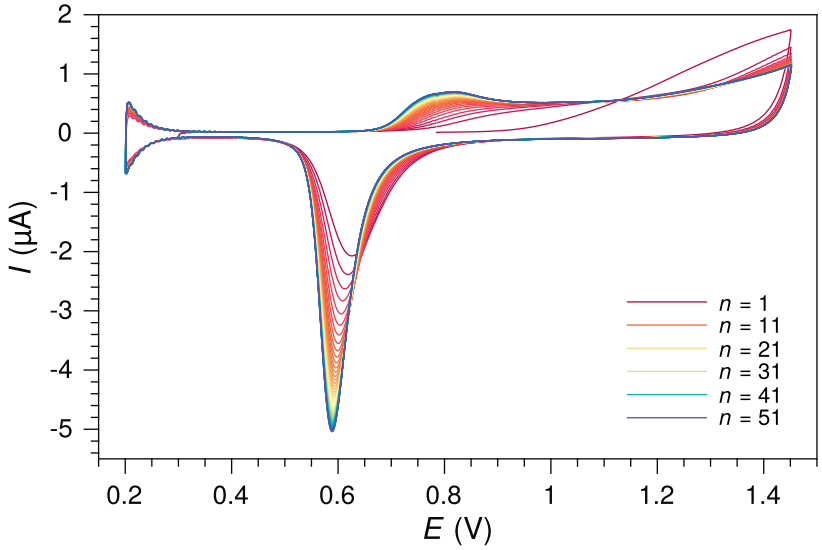

Figure 3.2: Initial cycling at 500 mV/s of a new 100 µm Pd electrode in 0.1 M H_2SO_4. The legend shows the line color for a selection of the cycles.

in figure 3.2. For the new Pt electrode, 10 cycles were typically enough for the following cycles to produce stable voltammograms. The Pd electrode required much more cycling before the voltammogram was stable, with the new electrode being cycled for typically 50 cycles. For electrodes in previously used cells, especially with high concentrations of methanol, the currents from the first cycles were lower and more cycling was required to stabilize the electrode. This is also dependent on the upper vertex of the cyclic voltammetry, and sweeping to a higher potential for a few cycles would speed up the process.

Figure 3.3 shows the cyclic voltammograms at various scan rates for a platinum microband electrode in 0.1 M sulfuric acid. The electrode was cycled between 0 and 1.45 V. The main characteristic feature of the Pt voltammogram is the underpotential hydrogen adsorption/desorption peaks at low potentials [77]. The peaks are close to symmetric, with the strong adsorption/desorption peaks at 210 mV and the weak peaks at 70 mV. The formation of platinum oxide on the surface commences at 0.75 V in the forward scan, while the reduction of surface oxide begins at 1.0 V, with the cathodic peak at around 0.7 V.

The palladium electrode in figure 3.4 was cycled between 0.2 and 1.45 V in 0.1 M sulfuric acid. Palladium does have underpotential hydrogen adsorption, but the major difference to platinum is that the adsorbed hydrogen then becomes absorbed and may diffuse into the Pd lattice, forming palladium hydride. The electrode should not be cycled to too low potentials, as repeated PdH formation and reduction may damage the electrode. For high scan rates

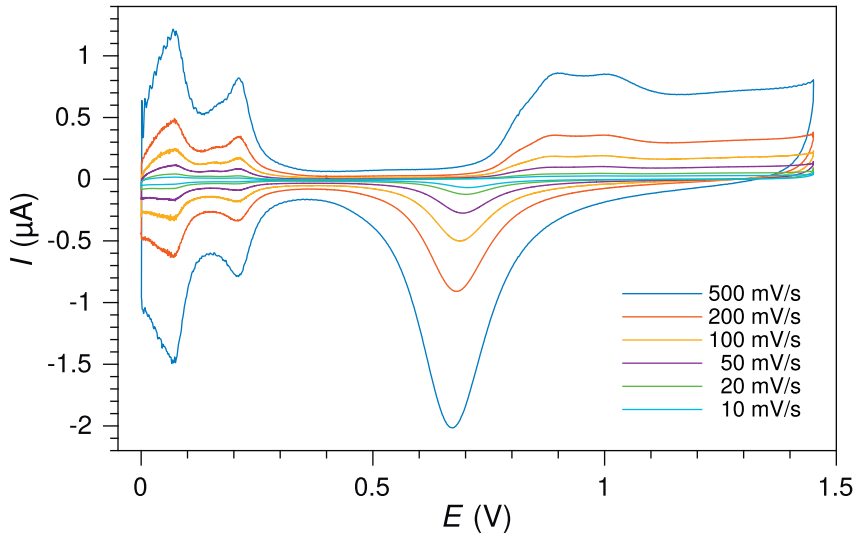

Figure 3.3: Voltammograms at various scan rates for a 100 µm Pt electrode cycled between 0 and 1.45 V in 0.1 M H_2SO_4.

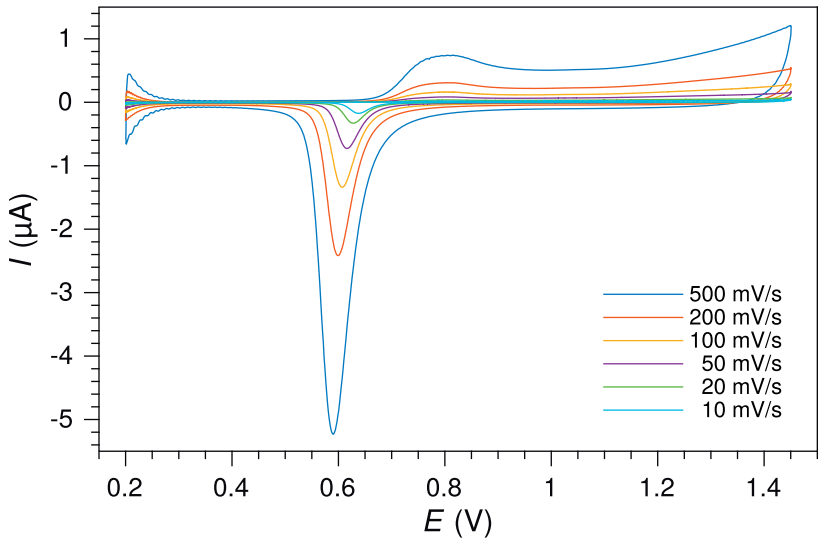

Figure 3.4: Voltammograms at various scan rates for a 100 µm Pd electrode cycled between 0.2 and 1.45 V in 0.1 M H_2SO_4.

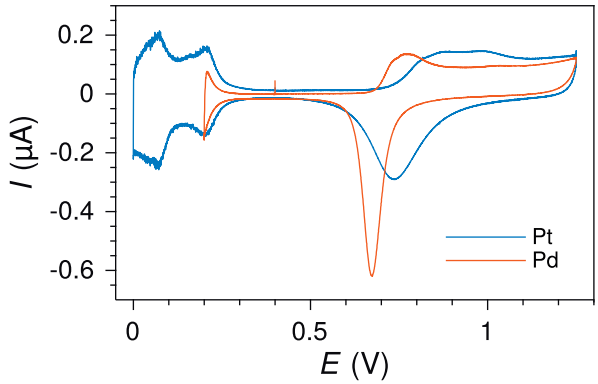

Figure 3.5: Comparison between Pt and Pd cyclic voltammograms at 100 mV/s in 0.1 M H_2SO_4.

the lower vertex is symmetrical, as the hydrogen does not have time to diffuse into the thin-film electrode. In the forward scan, the formation of palladium oxide starts at 0.67 V. As for platinum, the oxidation charge passed in the oxide formation is slightly higher for lower scan rates (see figure 3.6a). In the reverse scan the reduction of the surface oxide begins, in this case, at 0.7 V, with a sharp peak at approximately 0.60 V, and the cathodic peak shifts slightly to higher potentials at lower scan rates.

Figure 3.5 compares the voltammograms of the platinum and palladium electrodes directly. The two metals are distinguishable from the characheristic electrochemical behaviour of the oxides.

When the current is normalized by the scan rate, as can be seen in figure 3.6b, the charge passed during the voltammograms can be compared. The hydrogen peaks for the different scan rates overlap closely for most scan rates. Hydrogen adsorption on platinum is a fast process, and the charge passed is determined by the number of available Pt sites for adsorption. At 10 mV/s the reduction of trace amounts of dissolved oxygen in the electrolyte is more prominent. The oxide formation starts at the same potentials, but more oxide is formed at the slower cycles. The reduction of the oxide also starts similarly, but slower scan rates have a larger cathodic peak shifting slightly to higher potentials.

3.3.1 Electrochemical area measurement

A commonly used, but somewhat inaccurate method of finding the electrochemically active surface area of a Pt electrode is to calculate the surface charge of underpotential hydrogen adsorption and desorption in sulfuric acid [78], as shown in figure 3.7. With the assumption of complete hydrogen coverage at the available Pt surface sites, and the literature value of the surface density

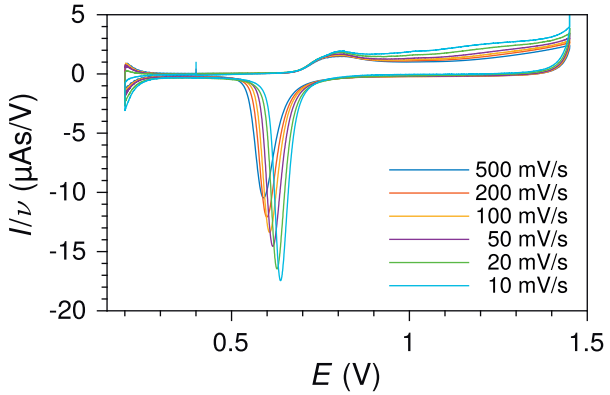

(a) Palladium

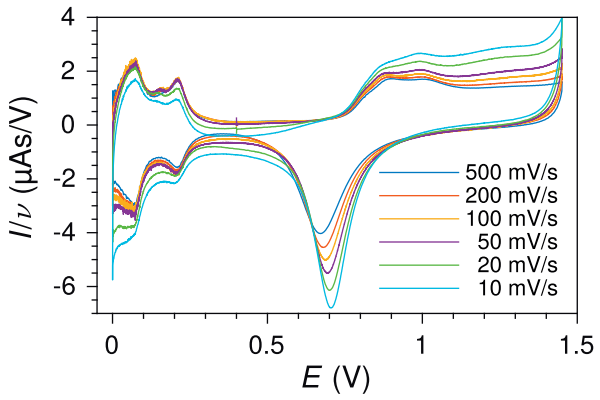

(b) Platinum

Figure 3.6: Voltammograms from figures 3.3 and 3.4 normalized by the scan rate. The unit of the area becomes μC.

of Pt, 1.31×10^{15} sites/cm^2 [79, 80], the electrochemically active area is found by dividing the measured charge by 210 μC/cm^2. The inaccuracies in this method stem from several factors. First, the current from hydrogen adsorption/desorption must be separated from other processes, i.e. the capacitive current component and hydrogen evolution. Second the potential of complete hydrogen adsorption is not clear for all systems. It may be necessary to perform the measurement for different lower vertices and scan rates, and extrapolate to infinite scan rate in order to obtain a more true value of the hydrogen adsorption charge [81]. Lastly the effect of ion interaction or other contaminants with the surface is not clear, and different electrolytes may give different results.

The measured electrochemically active surface area can be compared to the known geometric area to obtain a roughness factor for the electrode. The

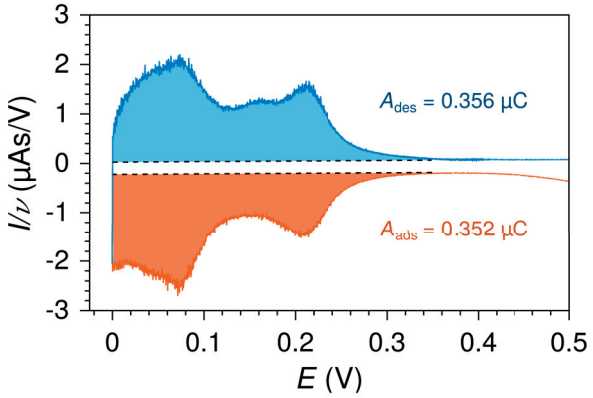

Figure 3.7: Hydrogen adsorption/desorption charge from CV at 100 mV/s between 0.00 and 0.35 V on a 100 µm × 1 mm Pt electrode.

typical roughness factor for Pt electrodes produced in this work was 1.70. This method is not applicable to Pd electrodes due to absorption of hydrogen into the palladium.

Other methods of electrochemically estimating the active surface area are to measure the double layer capacitance of the electrode and relate it to the area specific double layer capacitance of a known flat electrode of the same material, or measure the oxide charge during potential cycling and correlate it to the charge density, 424 µC/cm, associated with reduction of one monolayer of oxide (PdO) [82, 83]. These methods are also not very accurate, as the double layer capacitance measurement depends somewhat on the applied electrode potential and the measurement of oxide charge depends on an assumption that at a certain potential there is exactly one monolayer of the oxide covering the electrode. Although formation of one monolayer PdO was shown to occur when sweeping to 1.45 V [84], figure 3.6 shows that this is not really the case for platinum or palladium as the oxidation charge is also time dependent, i.e. depending on sweep rate. The oxide charge, or more simply the peak oxide reduction current for a certain set of parameters may be used as a control to verify that the electrode is behaving as expected during initial cycling, but is unsuitable for accurate normalization.

A more reliable electrochemical method of measuring the active surface area is to use stripping of adsorbed molecules on the surface [85]. CO-stripping is the most common example of this [86]. Carbon monoxide is a well known poison with strong adsorption on both Pt and Pd, and measuring the charge from anodic CO-stripping from cyclic voltammetry can provide a value for the number of surface sites. The stripping voltammetry requires that the electrolyte does not contain any more CO, to avoid readsorption so that only the adsorbed monolayer is measured. In conventional cells this is done by first covering the electrode with CO in a saturated solution, and then purging the

electrolyte with inert gas for 15 minutes while keeping the electrode in the solution. Unfortunately this was found to be incompatible with the PDMS-based microfluidic electrochemical cells due to absorption of CO into the channel slab. CO is almost as permeable in PDMS as nitrogen gas [67].

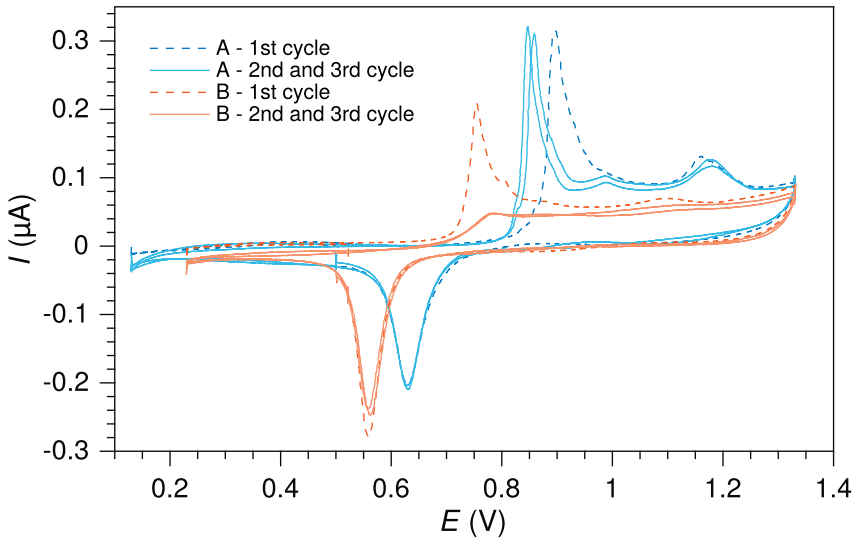

Figure 3.8: CO-stripping at 20 mV/s on a Pd electrode. A: after 2 minutes or B: after 100 minutes of flowing CO-free 0.1 M $HClO_4$ electrolyte through the cell.

CO-stripping was attempted on a 100 µm Pd electrode in a cell with two main electrolyte inlets. A saturated solution was prepared by bubbling CO gas through a base electrolyte of 0.1 M $HClO_4$ before drawing it into a syringe. The Pd electrode was cycled and then kept at 0.5 V while the electrolyte was switched to clean electrolyte. The electrode was then cycled at 20 mV/s in the supposedly clean electrolyte after purging the cell for approximately 2 minutes. The results of the stripping voltammetry in figure 3.8 show that there was still a large amount of CO in the solution, as a result of the CO that was absorbed from the saturated solution being released into the CO-free electrolyte. The voltammograms are actually close to those in the completely saturated solution. Even after 100 minutes of purging the cell with CO-free electrolyte there was still a trace of CO, though it was possible to perform a reasonable stripping voltammetry experiment. The electrode area can be calculated by assuming the charge associated with complete CO coverage to be 420 µC/cm, corresponding to two electrons per surface Pd atom, and measuring the charge difference between the first anodic scan and the stable subsequent voltammograms. Another noticeable effect of the CO covered Pd electrode is that it blocks the adsorption of hydrogen on the Pd electrode at lower potentials, which can be seen from the sweeps down to 0.13 V.

The effect of CO absorption could be limited by severely limiting the time the saturated solution is present in the channel, but in general PDMS-based devices seem unsuited for CO-stripping voltammetry, due to the long time required to remove CO from the cell.

Due to the inconsistency in measurement of electrochemically active surface areas, especially for palladium electrodes, the current measurements in this work is presented without normalization. Note that as most measurements presented in this thesis were done on 10^{-3} cm^2, normalization by geometric area is simple.

3.3.2 Oxide electrochemistry

Figures 3.9 and 3.10 shows the effects of changing the upper vertex potentials in cyclic voltammetry on Pt and Pd electrodes, respectively. Here we see a large difference between the two noble metal oxides. For the platinum electrode, the cathodic peak shifts towards lower potentials for higher upper vertex potentials, while the *onset* for reduction of the oxide starts at approximately 1 V for all cases. The cathodic peak shifts from 0.65 to 0.75 V as the upper vertex potential is changed from 1.6 to 1.0 V.

For the palladium electrode the effect is much more pronounced, with the cathodic peak shifting from 0.54 to 0.72 V. Moreover, the onset of the reduction is delayed significantly with higher upper vertex potentials, showing that the oxide formed is more difficult to remove. Almost all the oxide formed in the 1.0 V cycle is reduced at the potential where the oxide formed in the 1.6 V cycle begins to be reduced. Holding the potential at the upper vertex for some time was also found to have the same effect of suppressing the reduction of surface oxide to lower potentials.

3.3.3 Electrode size limit

An upper limit for the electrode widths that are practical for potentiodynamic experiments in microfluidic electrochemical cells was found from the cyclic voltammograms for various electrode and channel geometries. Note that the electrode widths used here are generally larger than the height of the microchannel. For electrodes that were too wide compared to the channel height, the potential distribution over the electrode became a problem due to the high resistance in the channel. This was observed as the cyclic voltammetry started producing errors in the potentiostat control amplifier in certain parts of the voltammogram, recording oscillating noise with amplitude the same as the current range of the measurement. The effect was first visible in the weak hydrogen adsorption region, as seen in figure 3.11. Alternatively, the noise would also cover the rest of the hydrogen adsorption region, parts of the oxide region, or the whole voltammogram as well. The effect was the same at multiple scan rates. The voltammograms were otherwise stable, indicating

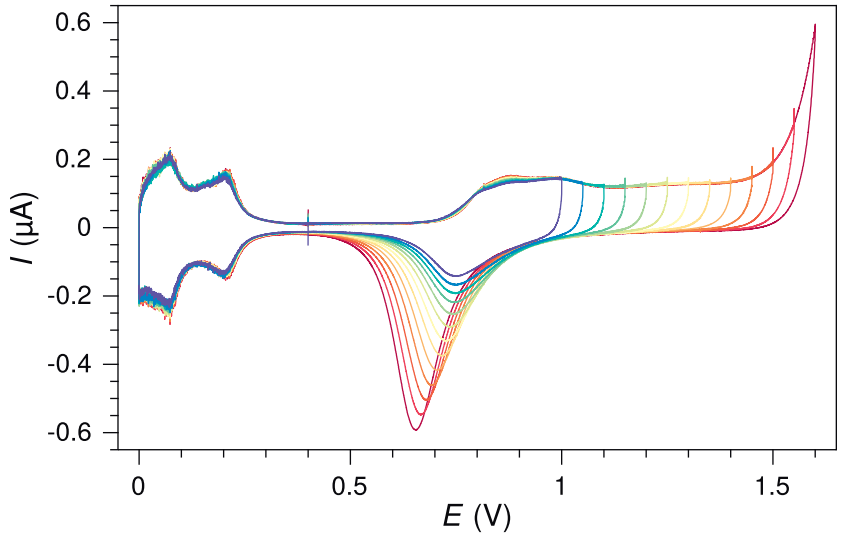

Figure 3.9: Platinum oxide electrochemistry. Effect of changing the upper vertex potential in Pt voltammetry. The electrode was cycled continuously at 100 mV/s in 0.1 M H_2SO_4, changing the upper vertex potential from 1.6 to 1 V.

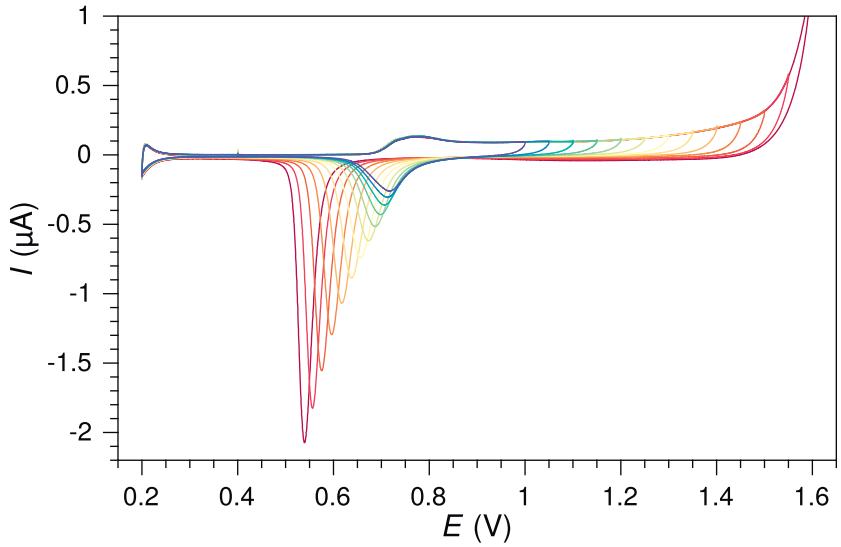

Figure 3.10: Palladium oxide electrochemistry. Effect of changing the upper vertex potential in Pd voltammetry. The electrode was cycled continuously at 100 mV/s in 0.1 M H_2SO_4, changing the upper vertex potential from 1.6 to 1.0 V.

that the effect is not real in terms of electrode surface processes, but rather a problem with the potentiostat control loop and electrolyte resistance.

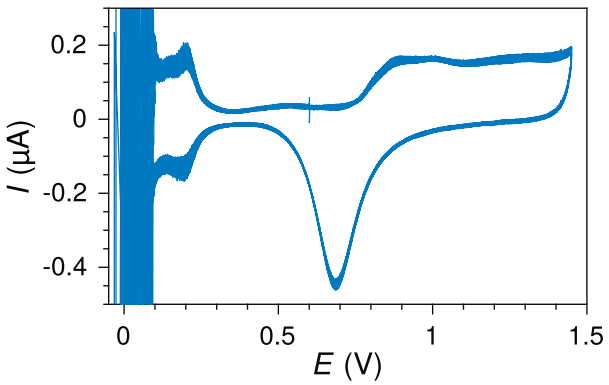

Figure 3.11: Potential control loop effects. Cyclic voltammogram at 100 mV/s of a 100 µm wide Pt electrode in a 22 µm high microchannel. 0.1 M H_2SO_4 electrolyte. Below 0.1 V the measurement is pure noise, while the rest of the voltammogram is reasonably normal.

The effect was seen both in cells with 100 µm wide electrodes in a 22 µm high channel, and on 500 µm wide electrodes in a $\sim$ 100 µm high channel, with both the BioLogic VPM3 and the Gamry Reference 600 potentiostat, and with both the internal PdH and an external RHE reference electrode. For the latter, this was only observed if the working electrode was between the counter electrode and the outlet reservoir containing the reference electrode. Increasing the conductivity of the electrolyte, e.g. by using 0.5 M H_2SO_4 instead of 0.1 M, did decrease or eliminate the effect, proving that the effect originates from the potential distribution and solution resistance.

As a rule of thumb, the electrode width should not exceed 4 times the height of the channel for 0.1 M sulfuric acid or similar electrolytes, in order to avoid these effects.

3.4 Conclusion

The platinum and palladium electrodes fabricated by photolithography and electron beam evaporation were found to be of high quality, and the response from cyclic voltammetry was as expected for these noble metals. In situ measurement of surface areas by electrochemical methods were demonstrated, and the typical surface roughness factor for platinum electrodes was 1.70. Due to the challenges in accurate and reproducible area measurements, the currents reported in this thesis have not been normalized by the surface area.

Chapter 4
Mass transport and fluid flow

Abstract

This chapter gives an introduction to the theory of mass transport mechanisms in microfluidic cells, and follows with experimental results describing the properties of the microfluidic electrochemical cell with regards to mass transport and electrolyte flow control.

4.1 Introduction

The mode of mass transport is what distinguishes microfluidic flow cells from conventional electrochemical cells the most. While channel electrodes are not uniformly accessible like the rotating disk electrode, the mass transport mechanisms can be investigated by numerical and experimental methods. The laminar flow regime in the microchannel means that the mass transport processes are predictable. However the analytical solutions to the processes depend on some assumptions which are not always applicable to the actual conditions in the microfluidic cell, and prediction of the mass transport processes at these conditions may require the use of numerical or semi-analytical methods [87].

The mass transport phenomena in microfluidic flow electrochemical cells may be tuned to very fast detection or high collection efficiency by changing the electrode layout and channel height of the microfluidic cell.

As the electrochemical measurements performed at microband electrodes are very sensitive to the electrolyte flow in the microchannel, it is important to know the influence of the equipment used to provide the flow. The standard syringe pumps do not operate completely smoothly due to the stepping motor, which can lead to extra periodic noise in the measurements.

In this chapter, the fundamental theory and equations for mass transport in the microfluidic electrochemical cells is presented, and compared with

experimental results using a reversible redox couple. The influence of the equipment on electrochemical measurements is then demonstrated.

4.2 Experimental

The general electrochemical setup and fabrication of microfluidic cells was as described in chapter 2.

Electrochemical measurements of mass transport phenomena was performed on cells with platinum or palladium microband electrodes in various configurations, in cells with channel heights 90 and 55 µm. The cell geometry used in the equations below is defined in figure 4.1.

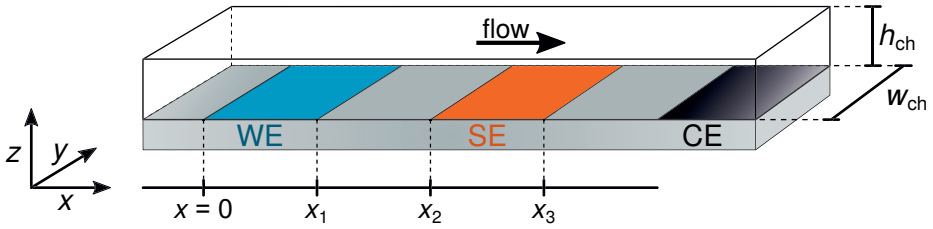

Figure 4.1: Geometry of the microfluidic electrochemical cell. The length of the electrodes is determined by the width of the microchannel (y-coordinate). This figure is compressed along the y-axis, while the x and z axes are to scale for a typical cell geometry.

Tris(2,2'-bipyridyl)ruthenium(II) ($Ru(bpy)_3^{2+}$) was used as a kinetically fast electrochemical species in the experimental results in this chapter. Solutions of 1 to 5 mM $Ru(bpy)_3^{2+}$were prepared in small quantities in either 0.1 M H_2SO_4 or a phosphate buffer electrolyte with 0.1 M Na_2SO_4.

$$Ru(bpy)_3^{2+} \longrightarrow Ru(bpy)_3^{3+} + e^- \qquad E^0 = 1.24\,V \qquad (4.1)$$

Experimental measurements of the mass transport limited current, collection efficiency and transit time were performed by potential step chronoamperometry on the working electrode while keeping the sense electrode at a constant potential of 1.0 V, low enough not to oxidize $Ru(bpy)_3^{2+}$but reduce $Ru(bpy)_3^{3+}$. Measurements of the mass transport limited currents and collection efficiencies were taken from the same set of experiments, using WE potential steps at least 15 s, and then averaging the current during the last half of the step duration. The currents were detrended by subtracting the stable background currents (due to e.g. oxide formation) measured before and after the potential steps. This background current was negligible at lower flow rates, but more substantial at higher flow rates.

4.3 Mass transport

4.3.1 Laminar flow

The defining feature of the microchannel is that at least one of the dimensions of the channel, in this case the channel height, is on the micro scale. The characteristic dimension is elemental in calculating the Reynolds number, which is one of the most used dimensionless numbers in fluid mechanics. The Reynolds number compares the inertial forces on the fluid to the viscous forces, and is used to predict the transition from laminar to turbulent flow.

The Reynolds number for a microchannel can be derived as [e.g. 88]:

$$Re = \frac{\text{Inertial forces}}{\text{Viscous forces}} = \frac{v_{\text{av}} L_0}{\nu} = \frac{QL}{A\nu} \tag{4.2}$$

where v_{av} is the average fluid velocity, Q is the volumetric flow rate, A is the channel cross-section, L_0 is the characteristic dimension and ν is the kinematic viscosity of the fluid. The characteristic length is given by the hydraulic diameter D_{H}, which for a rectangular duct is given by:

$$D_{\text{H}} = \frac{2ab}{a+b} \tag{4.3}$$

where a and b are the height and width of the duct. For a microchannel with $h_{\text{ch}} \ll w_{\text{ch}}$ we can write

$$D_{\text{H}} = 2h_{\text{ch}} \tag{4.4}$$

and:

$$Re = \frac{2Q}{w_{\text{ch}}\nu} \tag{4.5}$$

For the typical microchannel cross-section used in this thesis, $w_{\text{ch}} = 1\,\text{mm}$ and $h_{\text{ch}} = 55\,\mu\text{m}$, and using the kinematic viscosity of water at 25 °C: $\nu = 0.89\,\text{mm}^2/\text{s}$, we get:

$$Re = 0.0375 \left(\frac{Q}{1\,\mu\text{L/min}} \right) \tag{4.6}$$

reasonable flow rates, i.e. up to 1 mL/min ($v_{\text{av}} = 300\,\text{mm/s}$), fall well within the prediction for laminar flow ($Re \leq 2000$).

The microbore tubing used for the electrolyte inlets will also have laminar flow for the same flow rates that give laminar conditions in the channel:

$$Re = \frac{2Q}{\pi r \nu} = 0.0149 \left(\frac{Q}{1\,\mu\text{L/min}} \right) \tag{4.7}$$

The entrance length required for full development of laminar flow in a microchannel is given by [89]:

$$L_{\mathrm{E}} = 0.065 Re D_{\mathrm{H}} \tag{4.8}$$

which, for the same geometry as above becomes:

$$L_{\mathrm{E}} = \frac{0.26 Q h_{\mathrm{ch}}}{w_{\mathrm{ch}} \nu} = 4.1\,\mu\mathrm{m} \left(\frac{Q}{1\,\mu\mathrm{L/min}} \right). \tag{4.9}$$

The laminar flow regime will definitely be fully developed within 1 mm of the microchannel inlet for flow rates below 240 µL/min.

The advantage of laminar flow in an electrochemical cell is the predictable behaviour and precise control of the mass transport phenomena in the cell, and with the microchannel the range of possible time scales is very large.

Pressure-driven, steady-state flow of an incompressible fluid in a straight microchannel is known as Poiseuille flow [90]. As the cross-section of the channel does not change, the flow velocity is assumed to only have a component in the lengthwise direction. An analytical solution for the velocity field in a microchannel with a rectangular cross-section has been found [91]:

$$v_x(y,z) = \frac{4 h_{\mathrm{ch}}^2 \Delta p}{\pi^3 \eta L} \sum_{n,odd}^{\infty} \frac{1}{n^3} \left(1 - \frac{\cosh\left(n\pi \frac{y}{h_{\mathrm{ch}}} \right)}{\cosh\left(n\pi \frac{w_{\mathrm{ch}}}{2 h_{\mathrm{ch}}} \right)} \right) \sin\left(n\pi \frac{z}{h_{\mathrm{ch}}} \right) \tag{4.10}$$

Here, the y and z-coordinates are along the width and height of the microchannel, such that $\frac{-w_{\mathrm{ch}}}{2} < y < \frac{w_{\mathrm{ch}}}{2}$ and $0 < z < h_{\mathrm{ch}}$. Δp is the pressure drop over length L in the channel, and η is the dynamic viscosity of the fluid.

The solution of equation 4.10 for a typical channel cross section used in this work is shown in figure 4.2 for an arbitrary velocity $v_x' = v_x / v_{\max}$. The velocity at the channel walls is zero due to the no-slip condition. As the channel height is much smaller than the width, the velocity field is not affected by the side walls for most of the channel width (y-coordinate), and the velocity profile for the cross-section at $z = \frac{1}{2} h_{\mathrm{ch}}$ is mostly flat. In fact, the velocity field for most of the channel width can be accurately described by the much simpler equation for the flow between two parallel plates:

$$v_x(y,z) = \frac{\Delta p}{2\eta L} \left(h_{\mathrm{ch}} - z \right) z \tag{4.11}$$

which describes the parabolic velocity profile in the z-coordinate.

The relationship between the flow rate and the pressure drop in a channel is found by integration of the velocity field. In the case of rectangular microchannels there is no analytical solution, and the flow rate is approximated by:

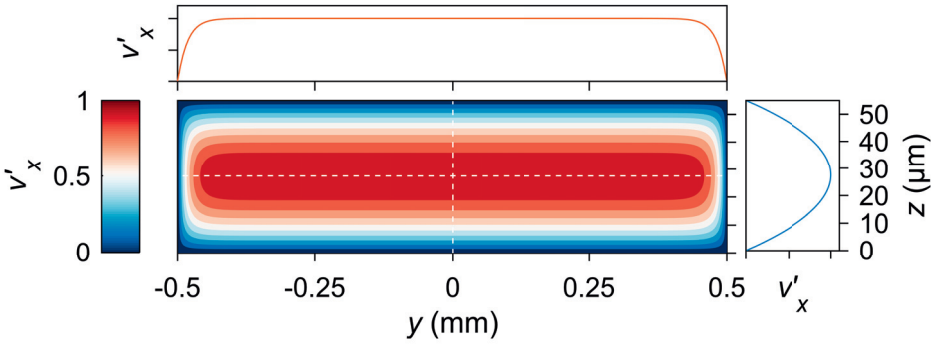

Figure 4.2: Flow velocity field in a rectangular microchannel with $h_{ch} = 55\,\mu m$ and $w_{ch} = 1.0\,mm$. Calculated from equation 4.10 for an arbitrary pressure drop and channel length. The field is normalized by the maximum velocity ($v'_x = \frac{v_x}{v_{max}}$). The top plot shows the velocity profile for $z = \frac{1}{2}h_{ch}$, and the right plot shows the profile for $y = 0$.

$$Q \approx \left(1 - 0.630\frac{h_{ch}}{w_{ch}}\right)\frac{h_{ch}^3 w_{ch}}{12\eta L}\Delta p \tag{4.12}$$

The factor in parentheses in equation 4.12 corrects for the influence of the side walls, and the second part of the equation is the analytical solution for flow between two parallel plates. For the geometry in figure 4.2 the correction factor is 0.965, i.e. treating the channel by the solution for parallel plates leads to a 3.5 % error in the predicted flow rate at a given pressure drop. For most practical applications the influence of the side walls may be neglected.

In practice, the flow rate is determined by the pump, and the pressure drop is established from this. The average flow velocity is simply determined by the flow rate and the channel cross-section ($Q = w_{ch}h_{ch}v_{av}$). It can also be useful to know the maximum flow velocity, which will be the velocity in the center of the channel. For the case of parallel plates this is easily derived from equation 4.11:

$$v_{max} = \frac{3}{2}v_{av} \tag{4.13}$$

Due to the influence of the side walls this will slightly underestimate v_{max} in a microchannel, and from numerical investigation of the velocity field in figure 4.2 we get:

$$v_{max} = 1.555 v_{av} \tag{4.14}$$

The laminar flow in microchannels may be treated as an analogue to electrical circuits in order to predict the flow in multiple elements connected in

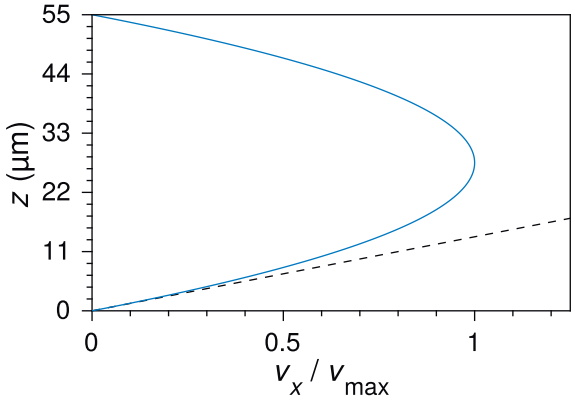

Figure 4.3: Lévêque approximation (dashed) compared to the analytical solution in figure 4.2.

series or in parallel. From equation 4.12 it is intuitive to define the *hydraulic resistance* for a rectangular microchannel:

$$R_{\text{hyd}} = \frac{\Delta p}{Q} = \frac{12\eta L}{\left(1 - 0.630\frac{h_{\text{ch}}}{w_{\text{ch}}}\right) h_{\text{ch}}^3 w_{\text{ch}}} \tag{4.15}$$

Continuing the analogue to electrical circuits the *hydraulic capacitance* [90] can be defined as the change in volume at changing pressures due to the compliance of the elements in the fluid circuit as well as gas bubbles. PDMS is a flexible material, and will react, if only slightly, to pressure differences.

4.3.2 Mass transport limited current

For electrochemical measurements the mass transport of species into the electrode is of interest. Close to the electrode surface, the parabolic flow profile in Poiseuille flow may be approximated by a linear function. This is known as the Lévêque approximation [92].

$$v_x = 4v_{\text{max}}\frac{z}{h_{\text{ch}}} \tag{4.16}$$

For a sufficiently fast electrochemical reaction, the current is dependent on the rate of mass transport to the electrode. This mass transport problem was solved using the Lévêque approximation and the assumption of $w_{\text{ch}} \gg h_{\text{ch}}$, leading to the Levich equation for channel electrodes [93], adapted for the geometry in figure 4.1:

$$I_{\text{lim}} = 0.925 n F c D^{2/3} Q^{1/3} \left(\frac{2 w_{\text{ch}} x_1}{h_{\text{ch}}} \right)^{2/3} \tag{4.17}$$

where n is the number of electrons transferred in the reaction, c^{∞} is the bulk concentration of the reactant, D is the diffusion coefficient, and x_1 is the width of the working electrode in the x-direction (see figure 4.1).

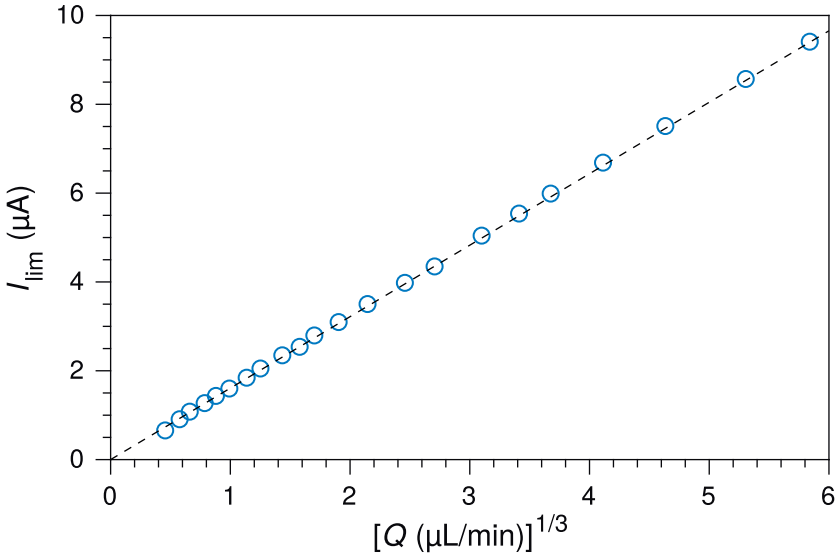

Figure 4.4: Mass transport limited current. Oxidation current of 5 mM $Ru(bpy)_3^{2+}$ in 0.1 M H_2SO_4 measured at 1.35 V on a Pt electrode. Geometry $h_{\text{ch}} = 55\,\mu\text{m}, w_{\text{ch}} = 1\,\text{mm}, w_{el} = 100\,\mu\text{m}$.

From equation 4.17, a plot of the mass transport limited current vs. the cube root of the flow rate should be linear. This was confirmed experimentally for a 100 µm wide Pt electrode in a 1 mm × 55 µm microchannel, as seen in figure 4.4. The relationship holds true for all reasonable flow rates, and only breaks down due to depletion at flow rates below 1 µL/min.

4.3.3 Collection efficiency

The collection efficiency for two channel electrodes under laminar flow has been described analytically under the Lévêque approximation and negligible axial diffusion by equation 4.18 [94].

$$\begin{aligned} N = 1 - F\left(\frac{\alpha}{\beta}\right) + \beta^{2/3}\left(1 - F(\alpha)\right) \\ - (1 + \alpha + \beta)^{2/3} \times \left[1 - F\left(\frac{\alpha}{\beta}(1 + \alpha + \beta)\right)\right] \end{aligned} \tag{4.18}$$

where:

$$F(\theta) = \frac{3^{1/2}}{4\pi} \ln\left[\frac{(1+\theta^{1/3})^3}{1+\theta}\right] + \frac{3}{2\pi} \arctan\left(\frac{2\theta^{1/3}-1}{3^{1/2}}\right) + \frac{1}{4} \tag{4.19}$$

and:

$$\alpha = \frac{x_2}{x_1} - 1 \tag{4.20}$$

$$\beta = \frac{x_3}{x_2} - \frac{x_2}{x_1} \tag{4.21}$$

The expressions in equations 4.20 and 4.21 are defined by the electrode geometry in figure 4.1. α and β are dimensionless quantities, so the units do not matter, only the relative magnitudes.

As for the conventional rotating ring-disk electrode, there is no dependence on the electrolyte flow in this equation. It assumes no upper barrier for diffusion normal to the electrodes. The thin microchannel, with h_{ch} comparable to typical values for the electrode geometry, means that the species produced on the upstream electrode can not diffuse as far away from the electrode plane as they would in a higher channel, so the concentration in the channel, and thus the collection efficiency, is higher. This effect is more prominent for longer time scales, i.e. slower flow rates. We will refer to the collection efficiency by equation 4.18 as a limiting high flow rate collection efficiency, N_∞, which depends only on the electrode geometry. For microfluidic electrochemical cells N_∞ essentially gives the lower limit which the actual collection efficiency will approach at high flow rates.

For the electrode geometry most commonly used in this work, 100 µm wide electrodes separated by a 100 µm gap (i.e. $x_1 = 1$, $x_2 = 2$, $x_3 = 3$), N_∞ is 0.250. This will be the same for any set of electrodes with the gap the same width as the electrodes.

Figure 4.5 shows the experimentally measured collection efficiency in a set of cells with 100 µm platinum microband electrodes with various gaps between the WE and SE. The dashed lines show the calculated collection efficiencies for the electrode geometries by equation 4.18. The calculated value is accurate for high flow rates (> 20 µL/min) while for lower flow rates the experimental value deviates towards higher collection efficiencies, as expected. The deviation is greater for larger gaps as the transit time is higher.

For thinner channels and lower flow rates, the deviation from N_∞ is greater, and collection efficiencies reach 0.5-0.7 for the standard 100 µm design in a 55 µm high channel at 0.2 µL/min. This is however not an optimal way of increasing the collection efficiency, as the lower flow rates are less stable and harder to work with in practice.

A better way of increasing the collection efficiency is to optimize the electrode geometry. Reducing the upstream electrode width and the electrode gap to 20 µm, with a 100 µm sense electrode, gives a N_∞ of 0.475.

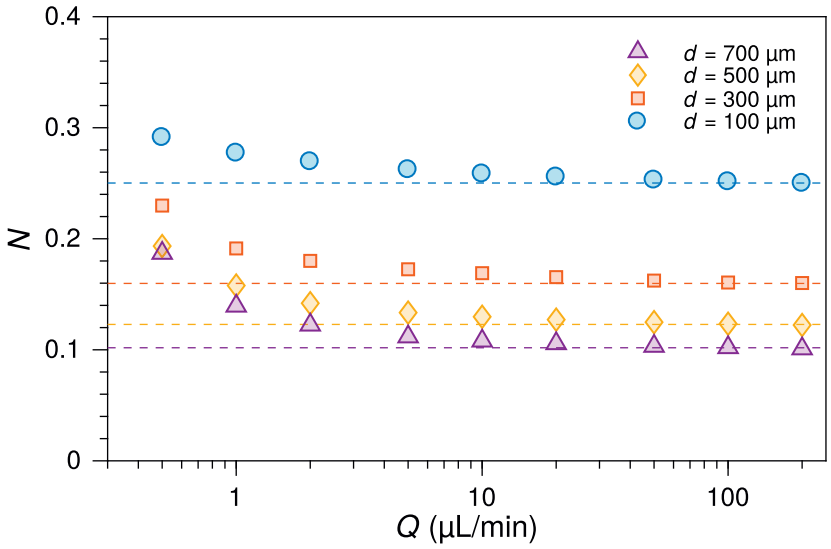

Figure 4.5: Collection efficiency as a function of the electrode gap. Experimentally measured collection efficiencies between 100 µm Pt electrodes with different electrode gaps ($d = x_2 - x_1$). Dashed lines show N_∞ . The channel height was 90 µm. The measurements were performed with 1 mM $Ru(bpy)_3^{2+}$in a pH 3 phosphate buffer / 0.1 M Na_2SO_4 by stepping the WE to 1.5 V, while keeping the SE at 1.0 V.

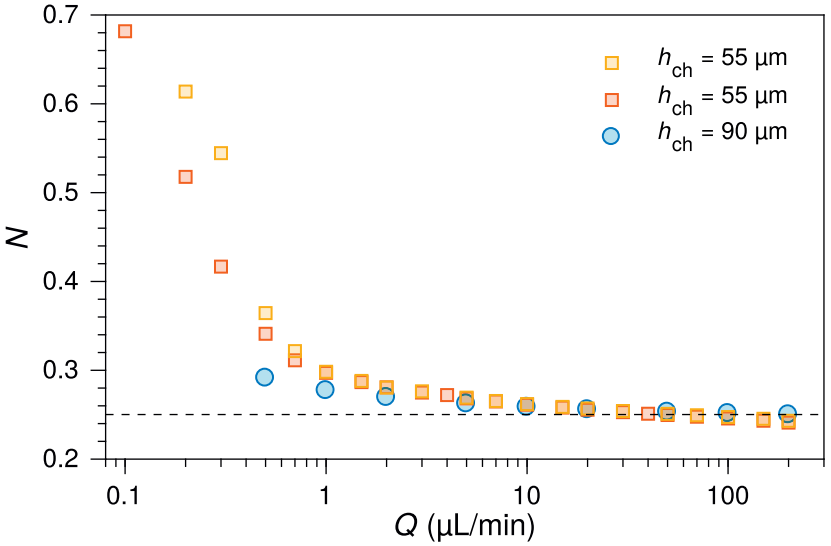

Figure 4.6: Collection efficiency and channel height. Experimental collection efficiencies for cells with 100 µm wide electrodes with a 100 µm gap, and 90 (same as in figure 4.6, blue circles) or 55 µm (squares) high channels.

It should be noted however, that while the collection efficiency is improved with wider sense electrodes, the actual signal-to-noise ratio might suffer. Especially for potentiodynamic techniques, the currents from surface processes such as oxide formation and reduction will scale linearly with the electrode area, while mass transport dependent currents will not. In addition there is a limit to the size of electrodes that can be used in practice for electrochemical measurements in microfludic cells, as discussed previously in section 3.3.3.

4.3.4 Transit time

In the multi-electrode microfluidic electrochemical cell, the *transit time* is the approximate time it takes for a certain species produced at the upstream working electrode to be detected at the downstream sense electrode. Figure 4.7 shows an example of the detection of $Ru(bpy)_3^{3+}$ on the SE after a potential step at the upstream WE in 5 mM $Ru(bpy)_3^{2+}$. The sense electrode detects a brief current spike as the WE potential is stepped at $t = 0$. As the electrode gap is on the same scale as the width of the electrodes, there is a significant delay after the initial detection before the steady state collection current. The initial detection time can intuitively be seen as the transport time from x_1 to x_2. The transport involves both downstream convection and diffusion normal to the electrode plane. The transit time did not scale linearly with the flow rate. At 1 µL/min, the transit time coincides with the electrode gap divided by the average velocity.

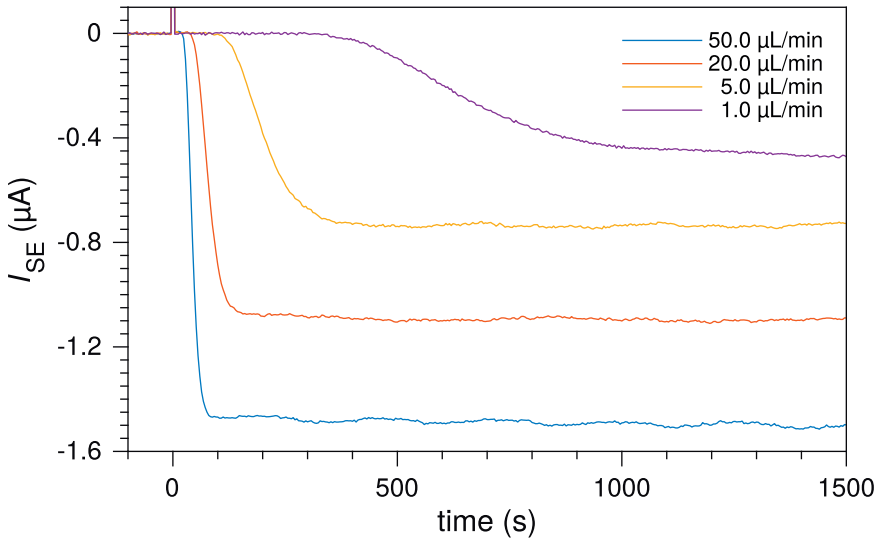

Figure 4.7: Transit time for 100 µm electrodes and electrode gap. Initial detection of $Ru(bpy)_3^{3+}$ produced at the upstream WE. Electrode geometry: $x_1 = 100$ µm, $x_2 = 200$ µm, $x_3 = 300$ µm Channel height 55 µm.

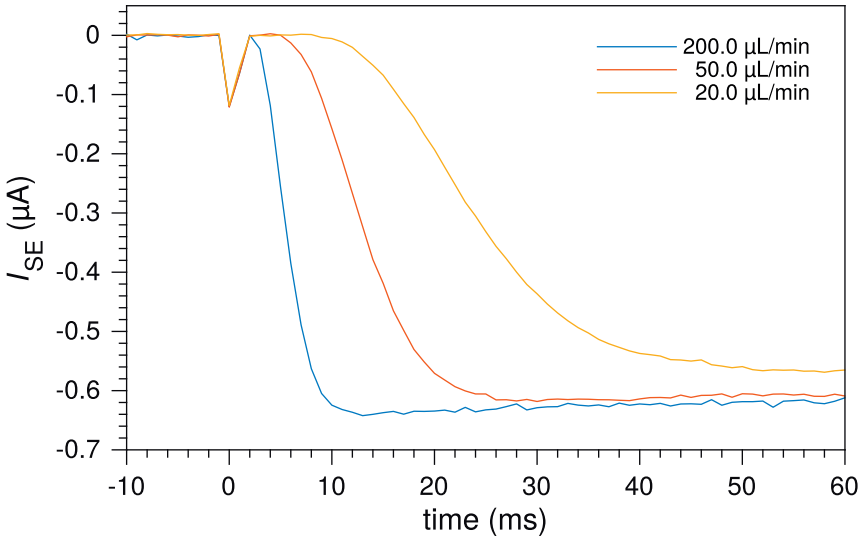

Figure 4.8: Transit time for 20 µm electrodes and electrode gap. Fast initial detection of $Ru(bpy)_3^{3+}$ produced at the upstream WE, with a cell geometry optimized towards lower transit times: $x_1 = 20\,\mu m$, $x_2 = 40\,\mu m$, $x_3 = 60\,\mu m$, $h_{ch} = 55\,\mu m$. Recorded at a sampling rate of 1000 Hz.

The transit time may be optimized by increasing the flow rate and decreasing the gap between, and the size of, the electrodes. Figure 4.8 shows the initial detection in a cell geometry optimized towards lowering the transit time. For 200 µL/min, the initial detection is at 3 ms, and steady state is reached after 12 ms. For reference, the average fluid velocity in the channel at 200 µL/min is 61 µm/ms.

4.4 Fluid flow

The simplest method of providing fluid flow in the microchannel is to use hydrostatic pressure, raising the inlet reservoir sufficiently above the outlet. This has the obvious downside of having no direct control over the flow rate provided.

The most common method of providing a controllable flow in microfluidic devices is to use a syringe pump. This pump uses a syringe as the inlet reservoir, and a pusher block moves the plunger of the syringe. The flow rate is determined by the diameter of the syringe and the speed of the pusher block.

A more recent development is the introduction of pressure pumps for microfluidics, using gas pressure over the inlet reservoir to create the pressure required for the flow. This also usually includes a flow meter in a feedback loop, as the fluid flow is not directly known from the applied pressure without

complete knowledge of the hydraulic resistance in the circuit as well as outside factors such as the pressure of the purge gas over the outlet reservoir.

4.4.1 The syringe pump

One of the major drawbacks with the syringe pump for electrochemical measurements, and mass transport dependent processes in particular, is the nature of the stepping motor. The syringe plunger is not pushed in a continuous motion, but rather as a series of discrete steps. The rate of the stepping is proportional to the flow rate and inversely proportional to the cross-section of the syringe used. Microstepping is a method of smoothing the motion of the motor [95]. While there is continuous work to improve the stepping angle and the microstepping of these motors, the oscillations they produce in the fluid flow were measurable by the mass transport limited current in the microfluidic electrochemical cells.

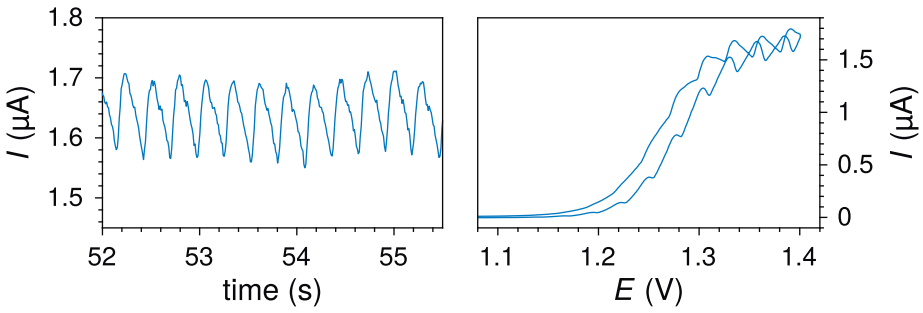

(a) Chronoamperometry at 1.4 V **(b)** Cyclic voltammetry at 100 mV/s

Figure 4.9: Examples of the oscillations in the measured oxidation current in 5 mM $Ru(bpy)_3^{2+}$ on a 100 µm wide platinum electrode, using the older syringe pump. The oscillations correspond to the full-step frequency of the syringe pump at this flow rate (3.7 Hz @ 5 µL/min)

In the beginning of this thesis work, a Model 33 Twin Syringe Pump (Harvard apparatus) was used. This syringe pump pushes the plunger of the syringe 0.33 µm for each microstep of the motor with ¼ microstepping. For a typical flow rate (5 µL/min) with a common 1 mL syringe with diameter 4.69 mm, this gives a step frequency of 14.6 Hz for the microsteps and 3.7 Hz for the full steps. These frequencies could be seen in the oscillations in the mass transport limited current, though the microsteps were usually not apparent. The "noisy" flow produces results like those in figure 4.9.

The noise in figure 4.9 is almost 10 % of the mean current, which would be detrimental to electrochemical experiments. It should be noted that it is possible to dampen the oscillations by increasing the compliance of the fluidic circuit, e.g. by introducing a length of Tygon tubing, though this would also decrease the responsivity of the flow.

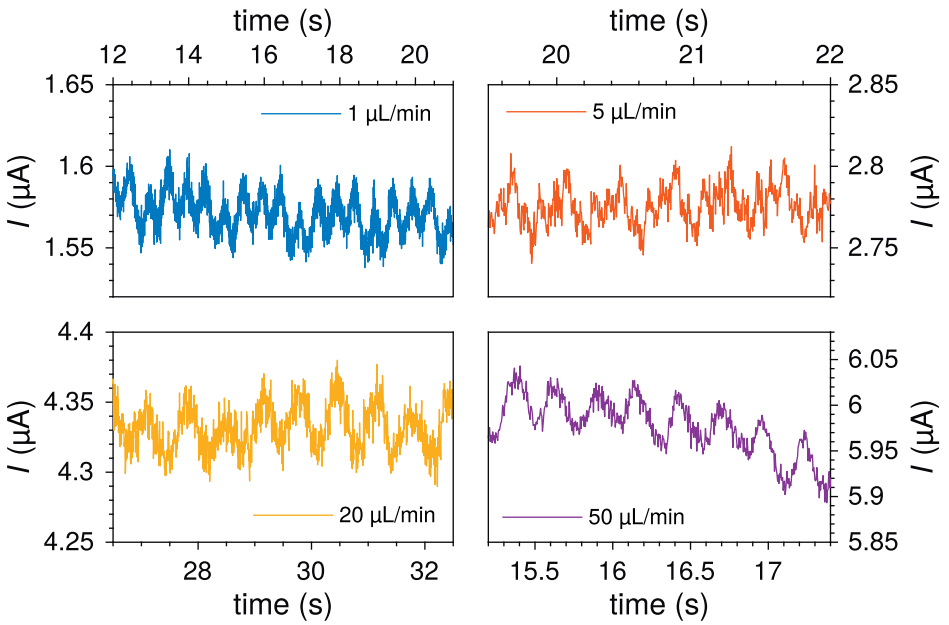

Figure 4.10: Flow oscillation at various flow rates with the P11 syringe pump and PTFE / glass syringes. Measured in 5 mM $Ru(bpy)_3^{2+}$ / 0.1 M H_2SO_4

A new syringe pump (Pump 11 Pico Plus Elite (P11), Harvard apparatus) was purchased. This pump has a finer full-step as well as 1/16 microstepping to smooth the oscillations. The pusher block moves 0.031 µm per microstep of the motor. While it is marketed as a virtually stepless syringe pump, some periodic noise is usually still seen in electrochemical experiments. The magnitude of noise is not only dependent on the pump itself, but also on the other components, most notably the syringes. The PTFE/glass syringes used mostly in this work have a very high resistance to pushing down the plunger which will dampen the oscillations. On the other hand, glass/glass syringes (e.g. Perfektum tuberculin) have very little resistance, and will transfer all oscillations in the pump block movement to the flow.

The source of the flow oscillations is easily tracked back to the pump motor as they are periodic with a frequency exactly equal to the step frequency of the motor at the given flow rate ($f_m \propto Q$). At higher flow rates periodic features with frequencies equal to the step frequency divided by an integer were found. Figure 4.10 shows the periodic fluctuations for a selection of flow rates. At 1 µL/min ($f_m = 2.0$ Hz), the periodic features have the same frequency as the pump full steps, though every 4th step looks different. At 5 µL/min ($f_m = 10.1$ Hz) the features with frequency $f_m/4$ are more prominent. At higher flow rates periodic features with frequency $f_m/28$ are most prominent. The noise levels are typically at 2% or less. While the noise may not be detrimental to

electrochemical experiments, it is useful to know what the source is.

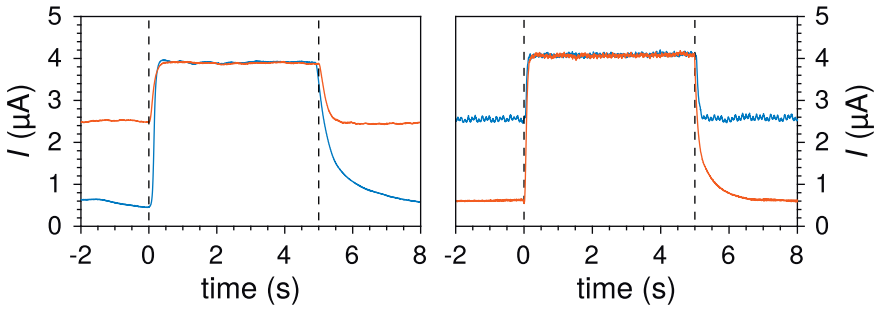

(a) PTFE / glass syringe. **(b)** Glass / glass syringe.

Figure 4.11: Flow responsivity and stability with different syringes in the same syringe pump. Measured by stepping the pump rate from 0 or 5 µL/min to 20 µL/min and back in 5 mM $Ru(bpy)_3^{2+}$.

Another important parameter of the fluid control is the responsivity. In one way this is inversely proportional to the stability of the flow, especially for syringe pumps. The responsivity determines how fast the target flow rate is reached, both when increasing and decreasing the flow, and depends on the properties of the whole fluidic circuit. Figure 4.11 shows the flow responsivity using syringes of similar diameter with (a) PTFE or (b) glass plungers. The rise time from 5 to 20 µL/min is (a) 0.4 s and (b) 0.14 s, and the relaxation time back to 5 µL/min is (a) 0.7 s and (b) 0.22 s. The responsivity with the glass plunger comes at a cost of a 200 % increase in the pump noise.

Another advantage of using high resistance syringe plungers is that they passively eliminate backflow. The pressure in the main channel can only push a small amount of fluid into the stagnant channels before the pressure is equalized, and the static friction of the syringe prevents further backflow. For example, the side channel with the reference electrode was usually kept stagnant while the main channel was under flow by using the PTFE/glass syringe, while lower resistance plungers (PP/PE or glass/glass) would in some cases be pushed out by the pressure in the channel.

It should be noted that in practice, *completely* stagnant fluid was difficult to achieve in the setup used. Especially when using a pressurized atmosphere to keep oxygen away, small changes in gas pressure as well as ambient pressure may cause the electrolyte to move within the channel, though controllable flow rates should range down to 0.1 µL/min.

4.4.2 The pressure pump

A pressure based pumping system (OB1 MK3, Elveflow) was tested as an alternative to the syringe pump. The advantage of this system is that the

gas pressure controlled flow is stepless, and may potentially be tuned to be more stable *and* more responsive than the syringe pump flow. The flow rate is measured by a flow meter between the reservoir and the cell, which is connected in a feedback loop to the pressure controller. The feedback loop must be tuned in a balance between responsivity and stability. The hydraulic resistance of the fluid circuit must also be tuned to match the pressure range of the controller, which normally involves adding small diameter tubing to the circuit.

For the use in the electrochemical setup, the additional components compared to the syringe pump setup proved a challenge. More components exposed to air made it impossible to use this pump in a regular bench setup without introducing too much oxygen to the electrolyte. A functional electrochemical setup with this pump will probably require having the entire fluidic circuit inside a glove box or glove bag to keep oxygen away.

Another practical challenge with the pressure pump system is that it is vulnerable to backflow. When working with multiple inlet cells, keeping one inlet stagnant requires actively measuring the flow rate and keeping it at zero by adjusting the pressure over the inlet reservoir.

If these experimental challenges are solved, the pressure pump system is more flexible than the syringe pump in terms of the flow programs that can be applied, and the increased responsivity may enable more hydrodynamic investigations than are possible with a syringe pump.

4.4.3 Electrolyte switching

One advantage of microfluidic electrochemical cells is that they allow for fast switching of the electrolyte. One major consideration here is the dead volume of the fluid circuit. With a single inlet the PTFE tubing represents almost all of the dead volume, which is in the order of 0.1 mL for a typical cell used in this work. In addition to this, the flow in the tubing is always laminar, and several times the dead volume is required to completely flush the previous electrolyte. This can of course be reduced by using thinner tubing, but the best way to decrease the dead volume and increase the electrolyte switching capabilities is to use a multiple input cell with a junction in the microchannel. The dead volume is then less than 1 µL.

In figure 4.12, the electrolyte switching and dual flow in a triple inlet microfluidic electrochemical cell is visualized using dyed water. The electrolyte over the working electrode can be switched in less then 1 second. The fluid in the stagnant inlets is pushed slightly back by the fluid under flow. When both main inlets are under flow, a clean dual flow is formed with very low mixing. This mode is used for example in membraneless fuel cells to separate the anode and cathode.

Note that the reference side channel (branching down from the main channel towards the lone reference electrode), which is kept stagnant with clear

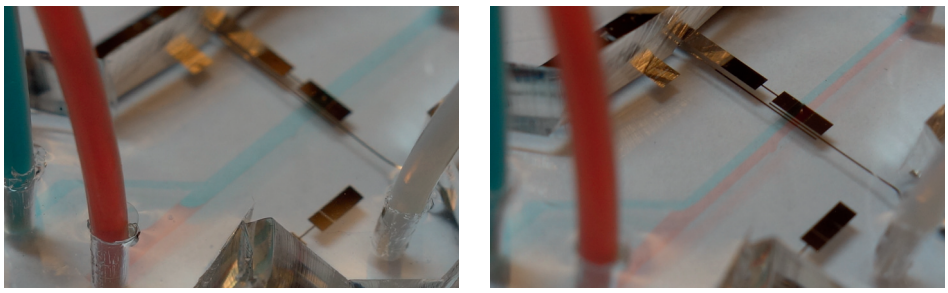

(a) Primary flow rate 0 µL/min, secondary flow rate 20 µL/min

(b) Both inlets at 20 µL/min

Figure 4.12: Visualization of electrolyte switching with dyed water. Flow to primary (straight) and secondary (branched) inlets was provided by the pressure pump, and the reference channel inlet kept stagnant connected to a PTFE / glass syringe. For scale, the reference electrode in the bottom right of the figure is 1 mm wide.

water using a PTFE / glass syringe, is not much affected by the flow in the main channel.

Another possibility with microfluidic electrochemical cells is to change the concentration by in situ mixing of different electrolytes. The device must then be tailored to allow for complete mixing of the electrolytes [96], which is the opposite case of figure 4.12b. With the pressure pump system, there is also commercial equipment which may be used to handle multiple electrolytes.

4.4.4 Gas bubbles

A common source of flow disturbances not originating from the syringe pump, was gas bubbles in the microchannel. A gas bubble would often be trapped in the intersection between the inlet tubing and the PDMS, and periodically block the electrolyte flow, creating characteristic and very regular spikes in the flow rate, and thus the measured current. The effect was seen easily with the reversible $Ru(bpy)_3^{2+}$species, but also with e.g. formic acid experiments. Trapped gas bubbles are relatively easy to remove with high flow rates if they are discovered.

Another problem with gas bubbles is that they may get trapped between the working electrode and the reference electrode, sometimes blocking off the electrical contact between the electrodes. When this happens the potentiostat may increase the current to the electrode in order to achieve the target potential. This actually caused some of the less robust palladium electrodes to be completely dissolved in a matter of seconds. Gas bubbles were especially problematic when working with external reference electrodes, as the bubbles would easily become trapped at the outlet of the cell.

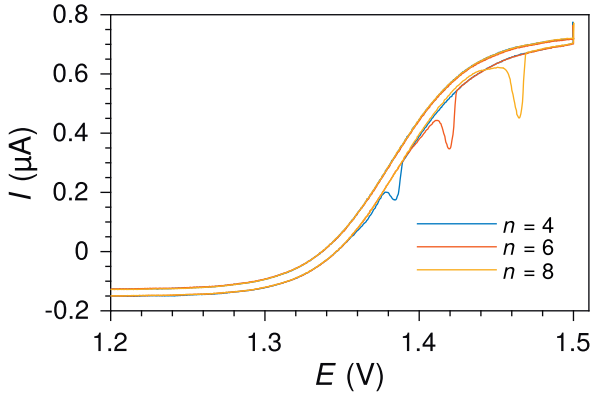

Figure 4.13: Current dips due to a gas bubble growing and blocking the flow momentarily during cyclic voltammetry on Pt at 100 mV/s in 1 mM $Ru(bpy)_3^{2+}$ at 50 µL/min. The dips are spaced evenly in 20 s intervals.

4.5 Conclusion

The theory behind the mass transport processes in microfluidic flow cells relevant for electrochemical measurements are presented. Microfluidic flow electrochemical cells present an ability to tailor the geometry of the cell towards different applications, such as high collection efficiency or fast mass transit. Mass transit times between two electrodes as low as 3 ms were demonstrated.

Some practical aspects with the operation of microfluidic electrochemical cells, such as the influence of the equipment used for electrolyte flow, are demonstrated. The syringe pump generated a periodic disturbance in the electrolyte flow, which should be minimized by using a smoother pump and high resistance syringes.

Chapter 5
The palladium hydride thin-film reference electrode

Abstract

An on-chip thin-film palladium hydride reference electrode is described for use with microfluidic electrochemical cells. A Pd electrode fabricated by photolithographic methods is electrochemically charged with hydrogen in-situ with a simple current step technique that may be monitored in situ without the requirement for external reference electrodes. The placement of the reference electrode in a side channel means that it is unaffected by species in the main channel. The stability of the thin-film reference electrode was found to be higher than previously reported, as long as care is taken to remove oxygen from the electrochemical system. A practical operation period of at least 5 hours is more than sufficient for most electrochemical experiments in the microfluidic cell.

The results in this chapter are published in Electrochimica Acta [1], along with the results in chapter 6. The text and figures have been modified for this thesis, in order to make the chapters stand-alone.

5.1 Introduction

Electrochemical experiments require a reference electrode to reliably measure electrode potentials. Using a reference electrode in a three-electrode setup allows for the study of processes at the working electrode without the influence of the reaction at the counter electrode [e.g. 97]. Traditional reference electrodes, such as the saturated calomel electrode, the Ag/AgCl electrode [47, 98, 99] or the hydrogen reference electrode, are very large compared to the cell, and need to be placed in an external chamber, typically downstream of the electrodes in the channel. It is important that the counter electrode is

situated downstream of the working electrode to avoid the processes taking place there influencing the concentration of species at the working electrode. This configuration is the source of an inaccuracy in the measurement of working electrode potentials due to uncompensated solution resistance. Moreover, external reference electrodes negate some of the attractive features of a fully integrated lab-on-chip device.

Integrated pseudo reference electrodes [100] based on gold [101, 102] or Ag/AgCl [103–107] have been used in lab-on-chip devices, but reporting potential measurements against these electrodes is problematic, as they are not based on thermodynamic equilibrium [108], or they are not separated from the sample electrolyte. Some successful implementations of stable integrated Ag/AgCl reference electrodes have been made, using laminar flow [109] or a nanochannel [110] in order to separate the sample electrolyte from the reference electrolyte while maintaining electrical contact. When working with platinum or gold electrodes however, it is advisable to avoid the presence of chloride ions due to adsorption and anodic corrosion of the electrode [111–113]. A certain constant amount of Cl^- ions is necessary to maintain a thermodynamically stable reference potential, and concentrations down to 10 ppm [74] can be harmful, especially to nanoparticle catalysts. Thomas et al. [114] demonstrated several thin-film metal/metal ion reference electrodes with non-electroactive anions. Integrated reference electrodes can also be based on a reversible redox couple in solution [38, 71] such as $Ru(NH_3)_6^{2+/3+}$ or $Fe(CN)_6^{3-/4-}$, but these will both be affected by, and affect the measurement of other species in the solution. A more extensive review of the most common microfabricated reference electrodes can be found in Shinwari et al. [115].

The internal palladium hydride reference electrode is a possible alternative to using traditional reference electrodes. Palladium can incorporate large amounts of hydrogen as a palladium hydride alloy, with an α-phase at mole fractions up to 0.017, and a mix of α and β (or α') phase up to a fraction of 0.58 at room temperature [116].

Palladium hydride electrodes generated from palladium wire have been found to hold a stable potential at 50 mV against a hydrogen reference electrode at the same pH [117]. This potential is generally attributed to the α-β phase transition of the PdH alloy [118]. As this reference electrode only requires a palladium metal electrode which can be charged in situ, it is relatively simple to fabricate by the same photolithographic method as the rest of the microfluidic cell, and it can easily be integrated in the cell upstream of the working electrode. One of the main concerns with the PdH reference electrode is the period of stable potential, as the alloy loses hydrogen to the electrolyte.

Imokawa et al. [119] reported fabrication and application of nanostructured PdH microelectrodes with lifetimes of 1-3 hours in deaerated solutions. Webster and Goluch [37] reported a microfabricated PdH reference electrode in a nanochannel, that was stable for up to 1 hour. In both these cases, an external

reference electrode was used to load the Pd structure with hydrogen.

In this chapter, the implementation and usage of the palladium hydride thin-film into the microfluidic cell is discussed. The process of charging the palladium electrode is monitored and controlled using a platinum electrode downstream of the former as a pseudo reference electrode. This senses the release of hydrogen as the palladium hydride reference electrode is charging.

5.2 Experimental

The fabrication of the microfluidic cells and the electrochemical setup is described in chapter 2. Figure 5.1 shows a schematic of the cells used in this chapter. The palladium reference electrode (REF) is 190 nm thick and 1 mm wide. The channel width is 1 mm both in the reference and the main channel. The distance from the internal reference is approximately 6 mm, while the distance to the outlet and the external reference electrode is approximately 1 cm

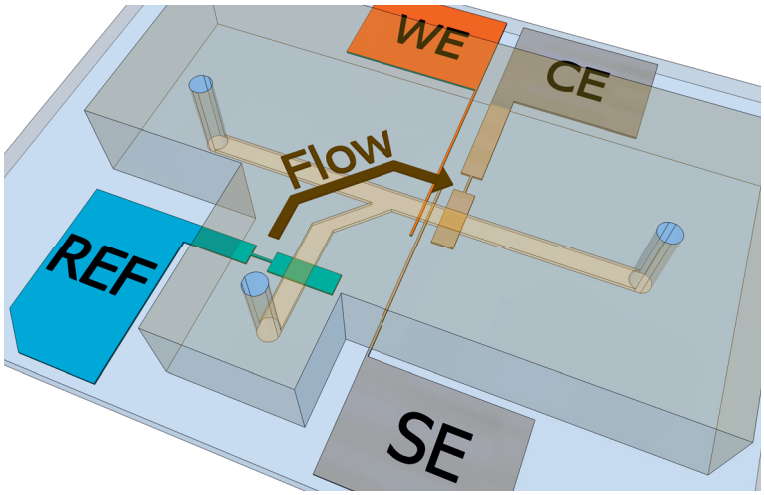

Figure 5.1: Schematic of the microfluidic cell. All dimensions except for the heights of the channel and electrodes are drawn to scale. The channel width is 1 mm. The 1 mm palladium reference electrode is located in a branched channel upstream of the main electrodes.

Electrochemical experiments were performed in either 0.1 M H_2SO_4 or a 50 mM phosphate buffer electrolyte (H_3PO_4 and Na_2HPO_4), with 0.1 M Na_2SO_4 supporting electrolyte. The buffer solution was calculated and measured to be pH 3.0.

The palladium hydride reference electrode was charged in situ by reduction of H^+ from the electrolyte at a constant current of –0.5 µA, under a flow rate of 5 to 20 µL/min trough the reference channel branch as indicated in figure 5.1.

The reduced hydrogen is adsorbed and then rapidly absorbed into the metal electrode, forming palladium hydride.

The potential of the palladium hydride reference electrode during was monitored during charging and at open circuit using a reversible hydrogen electrode (RHE), which was placed in a chamber at the outlet of the cell in the same electrolyte as the rest of the system. For normal operation of the microfluidic cell, without the external reference electrode, the charging process was monitored using the platinum working electrode as a temporary pseudo reference electrode.

5.3 Charging the PdH reference electrode

Figure 5.2 shows the potential transient during charging of the PdH reference electrode, measured against the RHE. The potential during charging goes through two plateaux, most clearly seen in the logarithmic plot. The first lasts 10 s, and corresponds to the formation of the α phase (low H solubility), and the second corresponds to the formation of the β phase (high H solubility).

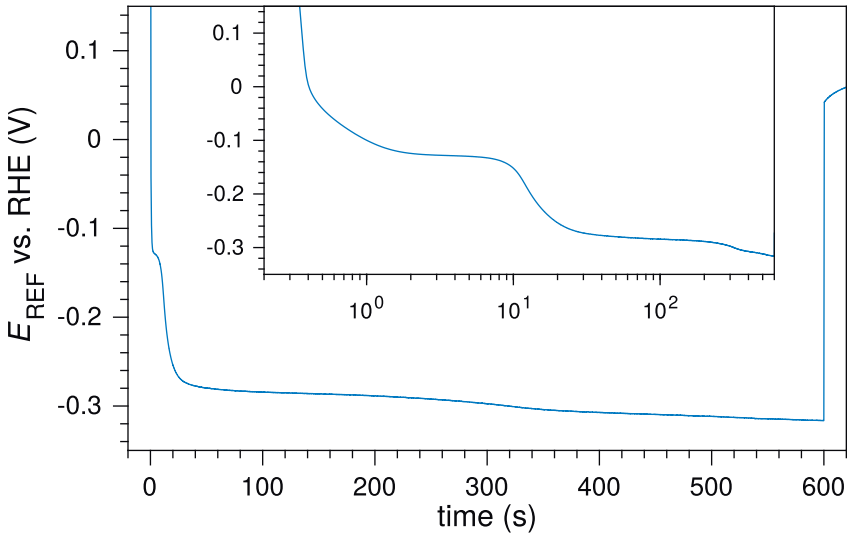

Figure 5.2: PdH charging transient. Charging a 1 mm wide thin-film Pd electrode (REF). Constant current at –5 µA from $t = 0$ to $t = 600$ s. Flow rate 20 µL/min through the reference side channel. Potential measured against a RHE in an outlet chamber. Inset shows the time on a log scale.

Figure 5.3 shows the measurement of the open circuit potential at the WE vs. RHE performed simultaneously with the charging of the PdH reference electrode in figure 5.2. The platinum electrode acts as a hydrogen sensor downstream of the charging reference electrode, with the potential moving

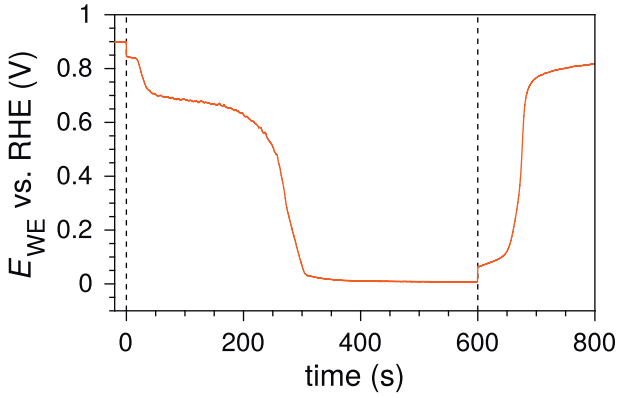

Figure 5.3: Downstream detection of hydrogen during PdH reference electrode charging. Measurement of the open circuit potential at WE vs. an external RHE during charging of the PdH reference electrode at a flow rate of 20 µL/min (figure 5.2). The potential flattens sharply at 300 s.

towards 0 V vs. the RHE as the amount of hydrogen gas in the electrolyte increases. At a flow rate of 20 µL/min, transport time from the RHE to the WE is around 1.6 s. Note that the steps in the potential at 0 and 600 s are due to IR drop between REF and CE when current flows between the electrodes. The potential decreases after 20 s, showing that not all of the hydrogen produced at the reference electrode is absorbed into the palladium. The open circuit potential decreases more rapidly after 200 s and flattens sharply at 300 s. This indicates that the release of hydrogen into the electrolyte at the reference electrode is near constant between 300 and 600 s.

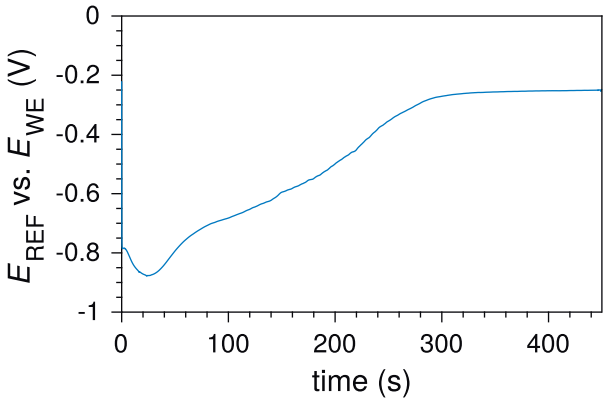

Figure 5.4: In situ monitoring of the PdH charging process. Measurement of the potential of the charging reference electrode vs. the downstream Pt WE. Electrolyte 0.1 M H_2SO_4 at 20 µL/min.

In the normal operation of the microfluidic electrochemical cell, i.e. without the external reference electrode, the release of hydrogen from the reference electrode was used to monitor the charging process. By using the platinum working electrode, located in the main channel downstream of the reference electrode as a temporary pseudo reference electrode, the measured potential can be seen as a combination of figures 5.2 and 5.3, with the requirement of an external reference removed. During the first 20 seconds, the potential drops, before hydrogen is starting to be released from the electrode, changing the potential of the pseudo reference electrode. The potential then rises and eventually flattens out, as the amount of H_2 released becomes constant.

The charge passed during 300 s at –5 µA is 1.5 mC, surpassing the calculated theoretical charge of 1.2 mC required to reach the pure β-phase in the exposed part of the Pd electrode. Based on this, we assume that the exposed part of the thin-film electrode is mostly converted to β phase PdH alloy during the charging. Whether more hydrogen is absorbed into the alloy beyond this point can not be discerned from this experiment. No adverse effects of charging the reference for longer than 300 s were observed in practice, and the time required for potential stabilization was similar whether the charging was aborted at 300 s or continued to 600 s. Charging for shorter times led to shorter or absent stable potential periods.

Visually, the palladium-hydrogen alloy had a darker tint than the parts of the electrode not exposed to electrolyte. The electrode returned to its normal color after being depleted of hydrogen during the experiments, and no visible changes or damage to the electrode were observed even after multiple charging cycles. As long as the faradaic processes at the palladium electrode were controlled, the reusability of the reference electrode was excellent. One palladium electrode was charged and discharged 15 times without measurable damage.

5.4 Stability and reproducibility

The potential of the PdH electrode was found to drift during the first 30 minutes after charging, before reaching a more stable potential. When measured against the RHE, the stable potential of the thin-film PdH reference electrode was (75 ± 5) mV. Figure 5.5 shows the continuous measurement of the electrode potential, with a stable period of 5 hours in a thoroughly deaerated cell.

In cells with no external reference, the PdH reference electrode was stable for up to 8 hours after charging, as inferred from hydrogen adsorption and desorption potentials at platinum. This PdH stability is difficult to demonstrate directly in cells with an external reference owing to practical complications in connection with the latter, mainly due to trapped gas bubbles blocking the channel outlet.

The potential of the reference electrode drifted by 1-2 mV/h over the op-

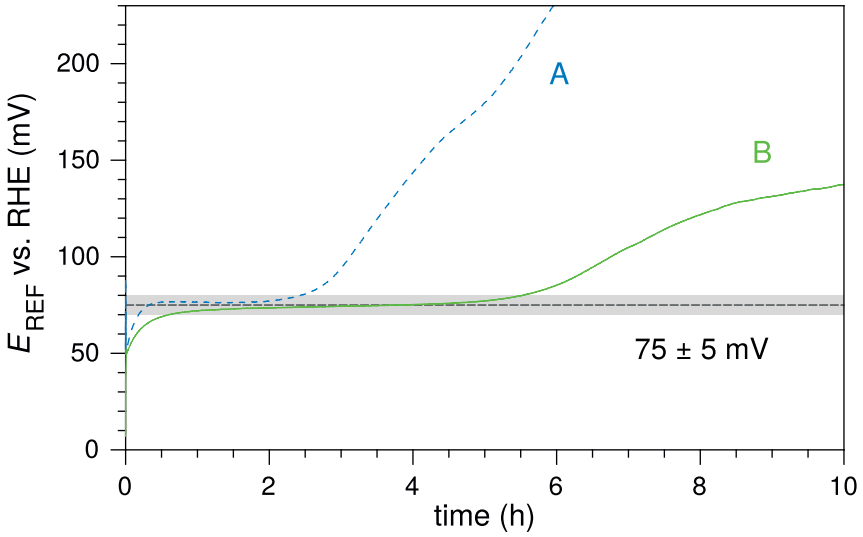

Figure 5.5: Stability of the PdH reference electrode. Open circuit potentials of the PdH reference electrode directly after charging, in a moderately (A) and thoroughly (B) deaerated cell.

eration period. The stability of the reference electrode was found to be very sensitive to the concentration of dissolved oxygen in the reference electrolyte. With the cell outside of the nitrogen-purged box, the PdH reference discharged within 15 minutes. For a moderately deaerated cell, i.e. a cell kept in an N_2-atmosphere for ∼4 hours, the potential typically remained stable for 2 hours.

One drawback with the thin-film PdH reference electrode was an increased pickup of electromagnetic noise compared to an external reference electrode. This was solved by operating the cell in a grounded Faraday cage.

The PdH reference electrode is reliable as long as certain precautions are taken. Firstly, the potential of the electrode will drift by about 1 mV/h as the PdH β phase is depleted of hydrogen, and up to 5 mV/h towards the end of the lifetime. This must be taken into account when reporting potentials against this reference. If possible, a known potential should be used to verify the reference potential and check the drift, for instance before and after the measurement. This could be towards an external reference electrode, a known electrochemical couple, or the hydrogen adsorption peaks of a clean Pt electrode.

Secondly, the pH of the reference electrolyte should be constant. During longer experiments it is possible that the species in the main electrolyte channel diffuse into the reference channel, even if it is kept stagnant. It is advisable to use the same electrolyte, or at least have the same pH in the main and reference electrolyte.

Third and finally, the absence of oxygen is very important to the stability of the reference. Electrolytes must be purged with inert gas before measurements,

and it is advisable to use glass syringes to keep the electrolyte deaerated during the experiments. PDMS is oxygen permeable, so the cell should be kept under inert atmosphere before and during the experiment. A short exposure to air when transferring the cell from storage to the experimental setup did not seem to have a measurable effect, but having the cell exposed to air for longer periods eventually introduced oxygen into the electrolyte.

Compared to other integrated reference electrodes for microfluidic cells, the main advantage of this reference electrode is the simplicity of the cell design and operation. The lifetime of a single charge is long enough for many continuous electrochemical experiments, and the ability to recharge the reference electrode in situ sets it apart from other electrodes. The stability of integrated Ag/AgCl reference electrodes varies with the complexity of the design and fabrication. Simple electrodes of similar dimensions fabricated by thin-film methods show similar or lower stability than this one [115]. This is due to the limited amount of Ag and AgCl making the electrode vulnerable to dissolution. Higher stability has been achieved by employing additional fabrication steps such as electroplating [103] to increase the amount of available silver, or coating the electrode with a polymer [105] or KCl-gel [107] to inhibit dissolution. In any case, an ion-conductive barrier would be required to avoid contamination of the working electrolyte, as the Ag/AgCl electrode is typically operated in Cl^- concentrations above 0.1 M. The non-contaminating reference electrolyte for the PdH electrode allows for a simpler cell design.

5.5 Conclusion

A microfluidic cell is described with an integrated PdH reference electrode placed in a side channel upstream of the working, sense and counter electrodes situated in the main channel. The side channel allows the reference electrode to be unaffected by the species in the main channel.

The PdH reference electrode was generated in situ by producing hydrogen at a 190 nm thick Pd thin-film electrode, creating a palladium-hydrogen alloy which was able to sustain a reference potential of (75 ± 5) mV, measured against a reversible hydrogen electrode, for at least 5 hours, with a potential drift of around 1 mV/h. The electrode can be charged in a highly reproducible manner, without the need for an external reference electrode. The re-usability of the microfluidic cells was found to be excellent, with at least 15 charge-discharge cycles possible without significant damaging effects to the thin-film electrode.

Chapter 6
Potential distribution and reference electrode placement

Abstract

The restricted volume in the microchannel means that the solution resistance is high. This may impact the accuracy of potential measurements on electrodes in the microchannel when the current is high. The effects of reference electrode placement and the interaction between multiple electrodes in the microchannel are examined. By placing the internal reference electrode upstream of the working electrodes, the effects of solution resistance is minimized.

The results in this chapter are published in Electrochimica Acta [1], along with the results in chapter 5. The text and figures have been modified for this thesis, in order to make the chapters stand-alone.

6.1 Introduction

One of the experimental challenges with performing electrochemical measurements in microfluidic cells, and the focus of this chapter, is the effect of solution resistance caused by the restricted volume of the microchannel. This can create large potential gradients in the microchannel when a current flows, which imposes severe limitations to the currents that can be applied to electrodes in the microchannel without losing accuracy in the measured electrode potentials. The main focus of electrochemical microfluidics has been low-current or single electrode sensing applications [34, 120–122], where the potential distribution, or even the electrode potential itself, is subordinate. Currents up to tens of nanoamperes typically cause potential shifts of less than a millivolt [47] in a microchannel. For a typical experimental setup, using a 1 mm by 50 µm channel and 0.1 M sulfuric acid as the electrolyte, the channel resistance per unit length becomes 43 kΩ/cm at 20 °C (data from [123]). This is manageable

for currents up to tens of nanoamperes, but for currents on the scale of microamperes, which is relevant for many electrochemical reactions, the potential distribution and reference electrode placement must be considered in order to report accurate electrode potentials. Knowledge and control of the potential distribution also gives a higher degree of flexibility in cell design and choice of supporting electrolytes.

In standard electrochemical cells the reference electrode is placed as close in the potential field to the working electrode as possible, for instance using a Luggin capillary, in order to minimize the uncompensated solution resistance R_s [77]. In a microfluidic cell with an external reference electrode, R_s becomes the full resistance between the working and counter electrodes, instead of just a fraction of it. Significant shifts in the potential sensed by the reference electrode can occur when current flows between the working and counter electrodes.

Problems with uncompensated solution resistance are compounded when working with multiple electrodes in the same microchannel, for instance using a downstream sense electrode to detect the products of the working electrode. The current through one of the electrodes will influence the solution potential above the other electrodes. This influence has been described for microchannels with external reference electrodes [98, 124, 125] at various electrode distances, and must be accounted for to be able to report accurate potential measurements.

In this chapter, the placement of the internal reference electrode upstream of the working electrodes is compared to the usage of an external reference electrode at the cell outlet. The interaction between multiple electrodes due to the potential distribution when a current is applied is examined for currents up to 75 µA.

6.2 Experimental

The fabrication of the microfluidic cells and the electrochemical setup is described in chapter 2. Figure 6.1 shows a schematic of the cells used in this chapter. The working and sense electrodes were 100 µm platinum electrodes with varying gaps between them, as defined by the edge-to-edge gap d in figure 6.2.

Electrochemical experiments were performed in a 50 mM phosphate buffer electrolyte (H_3PO_4 and Na_2HPO_4), with 0.1 M Na_2SO_4 supporting electrolyte (all Sigma Aldrich). The buffer solution was calculated and measured to be pH 3.0. Half-wave potentials were recorded in 1 mM tris(2,2-bipyridyl) dichlororuthenium(II) hexahydrate (Sigma Aldrich) in the buffer electrolyte, the electroactive species being $Ru(bpy)_3^{2+}$.

The potential distribution in the microchannel was probed by measuring the half-wave potential $E_{1/2}$ of the oxidation of $Ru(bpy)_3^{2+}$at constant flow rate, at the SE, while a current step technique was performed at the WE. Both

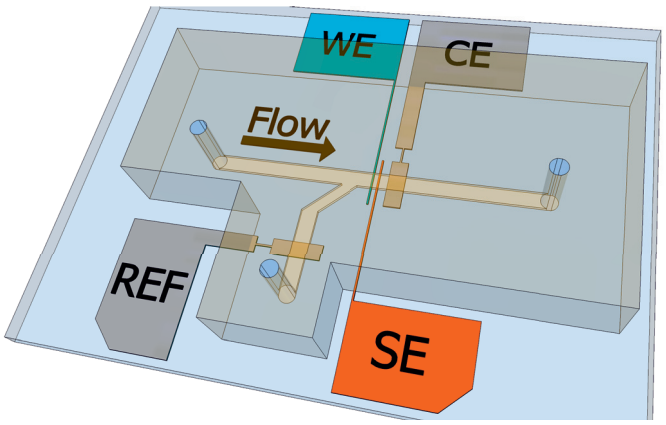

Figure 6.1: Schematic of the microfluidic cell.

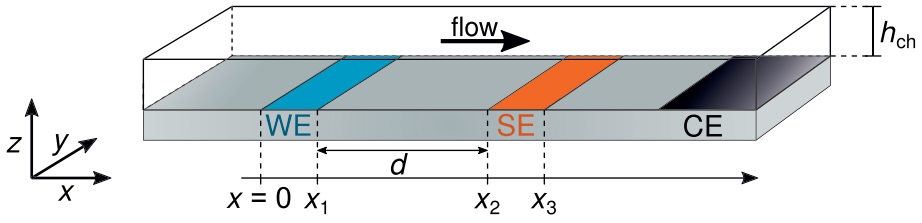

Figure 6.2: Geometry of the microfluidic cells used in this chapter. The working and sense electrodes are 100 µm Pt electrodes, with electrode gaps $d = 100$, 300, 500 or 700 µm. The channel dimensions are 1 mm × 90 µm.

the WE and SE were cycled at 100 mV/s between 1.0 and 1.5 V to stabilize platinum oxide on the surface. The mass transport limited current for the oxidation of $Ru(bpy)_3^{2+}$, I_{lim}, for the appropriate flow rate, was estimated from the maximum current when the potential cycling at the WE gave stable voltammograms. When the anodic electrode current is stepped beyond I_{lim}, the electrode potential is increased and oxygen evolution takes place in addition to $Ru(bpy)_3^{2+}$oxidation:

$$Ru(bpy)_3^{2+} \longrightarrow Ru(bpy)_3^{3+} + e^- \qquad E^0 = 1.24\,V \qquad (6.1)$$

$$2\,H_2O \longrightarrow O_2 + 4\,H^+ + 4\,e^- \qquad E^0 = 1.23\,V \qquad (6.2)$$

The half-wave potential shift was measured by cycling the SE at 100 mV/s from 1.0 to 1.5 V for 12 cycles, while current steps were applied to the WE. These techniques were linked so that the current steps on the working electrode were synchronized with the lower vertex points of the potential cycles on the SE, see figure 6.3. The SE was cycled several times per current step on the WE: first two initial cycles at open circuit, then four at a conditioning current

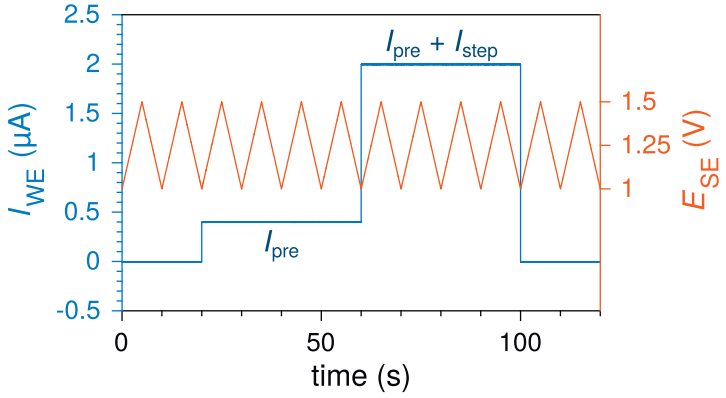

Figure 6.3: Applied waveforms. Blue: Chronopotentiometry steps applied to the WE. Red: Voltammetry cycles applied to the SE. The current on the WE was first stepped from open circuit to I_{pre} at 20 s, then stepped by a magnitude of I_{step} at 60 s. The half-wave potential shift at the SE was measured from the forward scans of the cycles directly before and after the step at 20 s.

I_{pre}, four at high current ($I_{pre} + I_{step}$), then two cycles at open circuit at the end. The magnitude of the step from the conditioning current to high current is defined as I_{step}. This was repeated for increasing values of I_{step}, up to 100 µA. The conditioning current I_{pre} was chosen to be slightly higher than the estimated limiting current, in order to ensure that the concentration ratio $c_{Ru(bpy)_3^{2+}}/c_{Ru(bpy)_3^{3+}}$ was constant over the high-current step. The half wave potentials were measured from the cycles directly before and after the high-current step, and the other cycles were used to validate the experiment, as the measurement was only considered valid if the voltammograms for each step were stable for all the cycles.

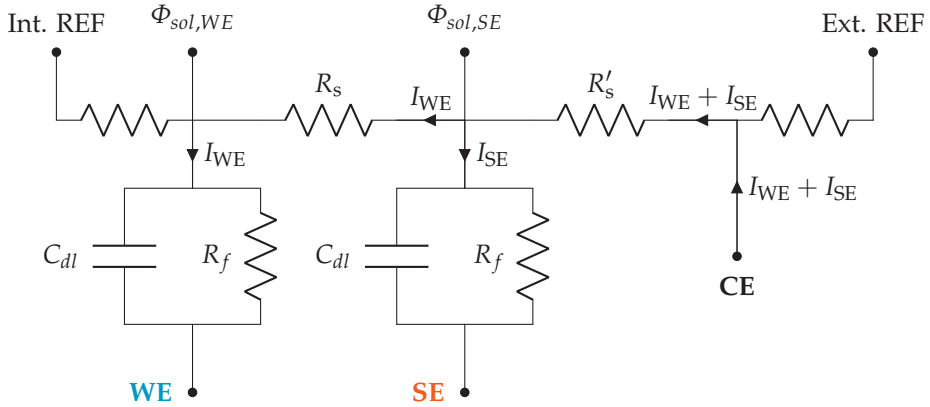

Figure 6.4: Simplified equivalent electrical circuit of a four electrode microfluidic cell.

The potential distribution in the microchannel can be predicted from the simplified equivalent electrical circuit in figure 6.4. As currents are applied between the WE and/or SE and the counter electrode, the electrolyte in the rectangular microchannel acts as an ohmic resistor shifting the solution potential along the channel length.

6.3 Potential shift on single electrodes

With a fully functional integrated reference electrode, the effects of reference electrode placement and potential distribution on the measurement of electrode potentials in the microchannel can be investigated. This section describes the effects on a single electrode, comparing the integrated (upstream) reference electrode with an external (downstream) one.

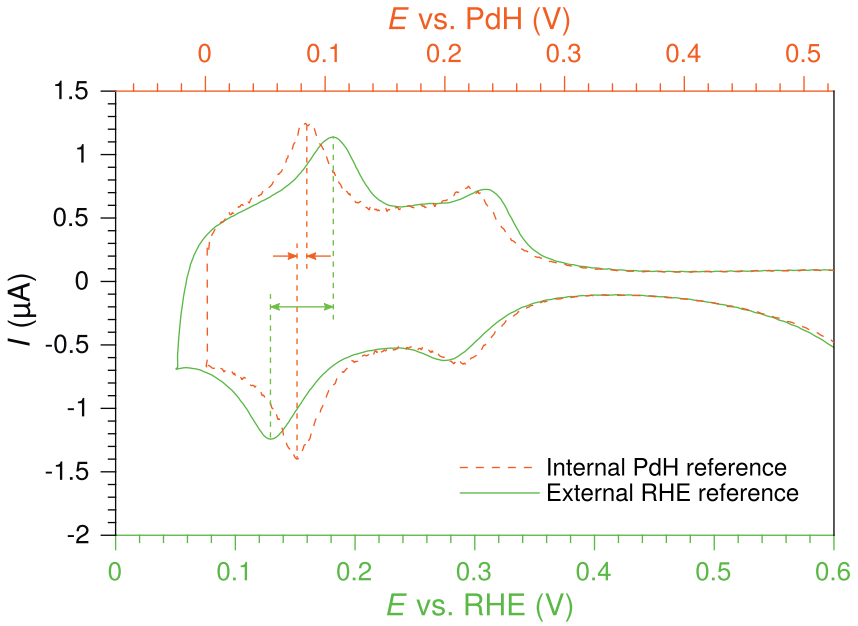

Figure 6.5: Strong (H_S) and weak (H_W) hydrogen adsorption and desorption peaks of a 100 µm platinum electrode (WE), recorded by cyclic voltammetry at 500 mV/s against an external RHE reference electrode (green, solid, bottom axis) and against the internal PdH reference electrode (red, dotted, top axis). The separation of the weak adsorption/desorption peaks (H_W) with the external reference electrode is 53 mV, and 7 mV with the internal PdH reference electrode.

The peak separation of strong hydrogen adsorption and desorption peaks was analyzed by cyclic voltammetry at 500 mV/s (figure 6.5), first using an external reversible hydrogen electrode placed in an outlet chamber, and then with the internal PdH reference electrode. The peak separation was 53 mV when using the external reference electrode, and 7 mV when using the internal

one.

These hydrogen adsorption and desorption peaks are characteristic features of platinum voltammograms. Ideally, there should be no peak separation [77]. The peak separation observed here is due to uncompensated solution resistance. This shows that even when performing electrochemical measurements on a single electrode, the effects of solution resistance and reference electrode placement in a microchannel can be significant.

These adsorption and desorption currents are small compared to the currents for the electrocatalytic reactions typically studied using these electrodes, and higher currents lead to larger potential shifts. This clearly shows that the configuration with the internal reference electrode is better suited for higher current experiments.

6.4 Interaction between multiple electrodes

When working with multiple electrodes in a microchannel, the situation becomes more complicated, as the currents at one electrode may influence the solution potentials at other electrodes in the channel. By moving the reference electrode upstream of the WE this is simplified, as the current on the SE should not influence the potential at the WE in this configuration. The current applied to the WE, however, will influence the potential at the SE or any additional electrodes downstream, and the magnitude of this influence will be quantified in this section. Figure 6.6 illustrates the expected potential distribution in the channel with currents flowing through the electrodes. This is derived from the simple equivalent electrical circuit for the microfluidic cell in figure 6.4, where electrode width is not considered. An anodic current through the WE, with CE as the counter electrode, is expected to shift the solution potential Φ_{sol} above the SE to lower potentials with a magnitude of $I_{WE} \times R_s$.

The shift in the solution potential above the SE was measured using the half-wave potential $E_{1/2}$ of the oxidation reaction of $Ru(bpy)_3^{2+}$, while oxygen was produced at the WE upstream. This redox system was chosen due to its stability, fast charge transfer, and that the redox potential can be fixed between the potentials for oxygen evolution and reduction on Pt by choosing the right pH. The voltammograms for this system at the flow rates used in this section are shown in figure 6.7.

At any potential where H_2O is oxidized, the WE will also oxidize $Ru(bpy)_3^{2+}$, so it was necessary to take both oxidation reactions into consideration when performing the current step. To account for this, the half wave potential was measured at the SE, first with the WE at a conditioning current (I_{pre}) slightly above the mass transport limited current of $Ru(bpy)_3^{2+}$, then again at a higher current with significant oxygen evolution. This ensures that the ratio of $c_{Ru(bpy)_3^{2+}}$ to $c_{Ru(bpy)_3^{3+}}$ in the Nernst equation (equation 6.3) will be constant over the current step, consequently the only difference between the voltammogram

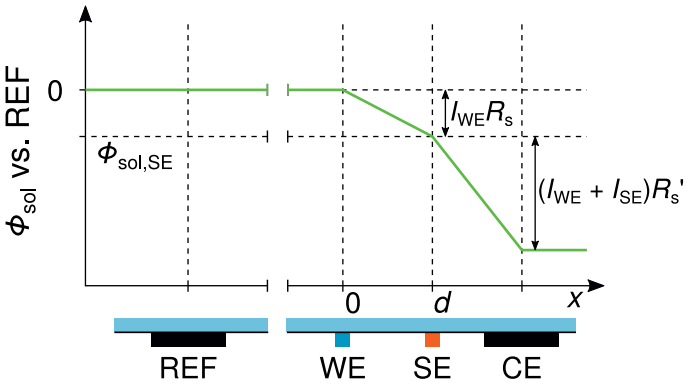

Figure 6.6: Expected potential distribution in the microchannel when an anodic current flows through both the WE and the SE, with CE as the common counter electrode. Derived from simple equivalent circuit of the cell. The current flowing between the WE and REF is negligible, so there is no potential gradient between these electrodes in the simplified case.

before and after the current step is the shift in solution potential Φ_{sol}.

$$E = E^\circ - \frac{RT}{F} \ln \frac{c_{red}}{c_{ox}} \tag{6.3}$$

Figure 6.8 shows the response in the voltammogram at the SE to the different chronoamperometry steps at the WE, and confirms that the method used is suitable for probing the solution potential. For $n = 2$ and $n = 12$, corresponding to $I_{WE} = 0$ before and after the experiment, there is complete overlap. The step from open circuit to diffusion limited current shifts the current of the voltammogram cathodically. The step from I_{pre} to higher current shifts the voltammogram to lower potentials, as is expected for anodic currents through the WE. The total current during the high-current step is $I_{pre} + I_{step}$. The experiment was repeated for a range of current steps, at flow rates of 0.5, 5 and 50 µL/min. Only the results recorded at 50 µL/min were used in the calculations, as the applicable oxygen evolution current was limited at lower flow rates due to accumulation of oxygen gas in the channel.

Figure 6.9a shows voltammograms for a cell with an electrode gap of 300 µm, with oxygen evolution currents of up to 74.1 µA at the WE. The potential is shifted up to 200 mV. Figure 6.9b shows the same voltammograms corrected by the measured half-wave potential shift. The forward scans overlap closely, verifying that the potential shift is the only difference between the voltammograms.

Figure 6.9b also shows a cathodic current at potentials below 1.2 V, corresponding to the reduction of oxygen gas produced at the WE. This current increases along with I_{step}, and was especially prominent at lower flow rates.

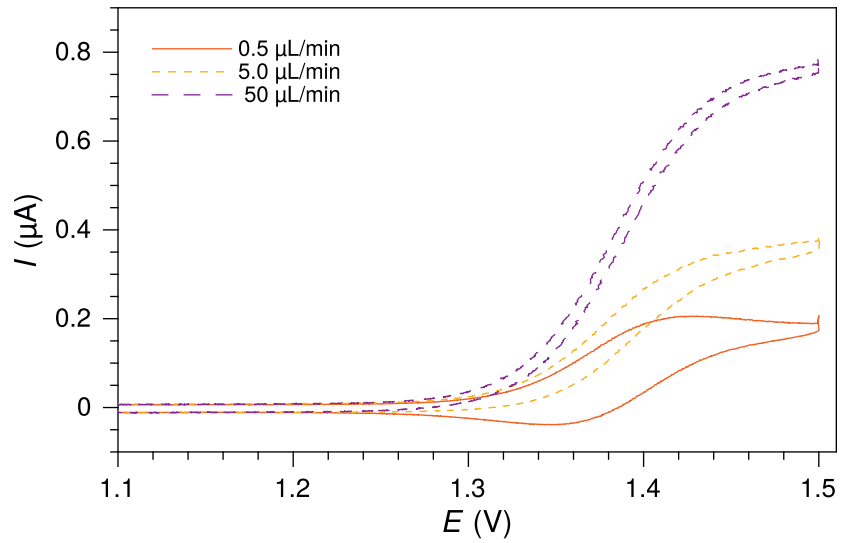

Figure 6.7: Voltammetry of the $Ru(bpy)_3^{2+}$redox system. Typical voltammograms recorded at 100 mV/s at the different flow rates used in this chapter.

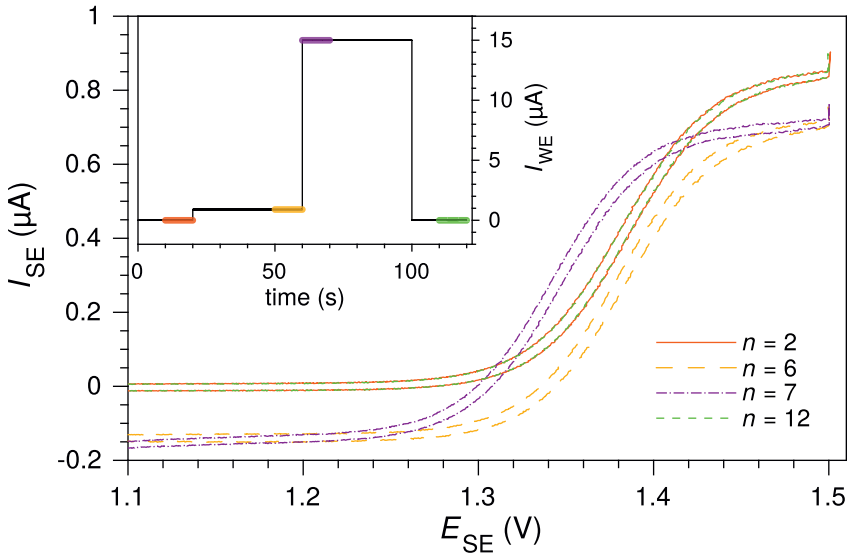

Figure 6.8: Cyclic voltammetry at the SE at different parts of the current steps on the WE (n is the cycle number). n=2 and n=12 are with WE at open circuit (and overlap completely), n=6 and n=7 are with the WE at the conditioning and high current steps. The half-wave potential shift is measured from the 6th and 7th cycles. The inset illustrates the current at the WE at the different cycles at the SE. The flow rate is 50 µL/min and the electrode gap d is 300 µm.

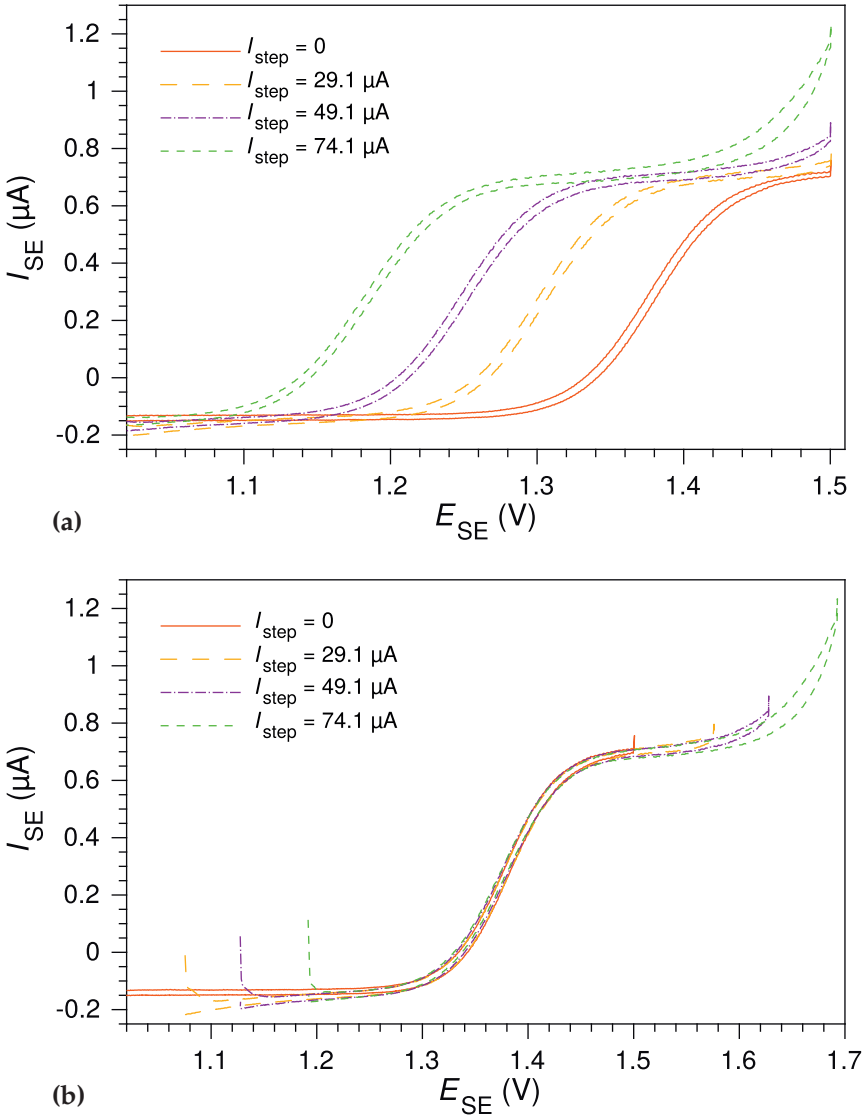

Figure 6.9: Potential shift voltammograms. (a) Voltammograms recorded at the SE, cycle 6 and 7, before ($I_{step} = 0$) and after galvanic step on WE. Electrode gap 300 µm, flow rate 50 µL/min. (b) The same voltammograms corrected for the measured potential shift.

When performing the same experiment in 0.1 M sulfuric acid, the potential ranges for reduction of O_2 and oxidation of $Ru(bpy)_3^{2+}$overlap making measurement of the half-wave potential shift impossible. In the pH 3 buffer solution, the processes that depend on the proton concentration, including the oxygen evolution as well as the PdH reference, are shifted to lower potentials so they don't overlap with $Ru(bpy)_3^{2+}$oxidation.

Figure 6.10a shows the half-wave potential shifts measured for increasing I_{step} for all flow rates. Figure 6.10b shows the data for all 4 cells, at 50 µL/min. The dashed lines are linear fits calculated by a robust (bisquare) linear least squares method. The bisquare method weights the data points closest to the fit heavier than the outliers. The slope of this line is R_s in $\Delta\Phi_{sol} = \Delta E_{1/2} = I_{WE} \times R_s$.

Most of the data points follow the linear fit closely, though a few measurements deviate to a larger shift than expected. This is due to oxygen bubbles of significant sizes beginning to form and block parts of the channel, effectively increasing the solution resistance. At high anodic currents the oxygen evolution is significant enough to form visible gas bubbles in the channel and in the outlet tubing. This is exaggerated at higher electrode spacing and lower flow rates, and sets an upper limit to the I_{step} in these experiments. This gradual resistance increase could be seen by comparing the subsequent CV cycles after the current step, as the voltammogram continued to shift further to lower potentials even while I_{step} remained constant. Consequently, the potential shift was only taken into consideration if it was stable over the 4 cycles. The channel was periodically flushed with short bursts at high flow rate to remove residual oxygen bubbles from the channel.

In figure 6.10c R_s, as found from the slopes in figure 6.10b, is plotted against the electrode spacing d. Only 50 µL/min data was used in the calculation, though the lower flow rates fit the same calculations at low I_{step}-values. The dashed line is an unbound linear fit calculated by a weighted LLS method, using the inverse of the 95% confidence interval from the calculation of the R_s values, as the weights. This fit intersects the d-axis at $d = -93$ µm. A more appropriate definition of the electrode spacing would seem to be the center-to-center distance, rather than the edge-to-edge distance of the electrodes.

The experimental electrolyte conductivity can be calculated from the slope of the linear fit in figure 6.10c and the dimensions of the microchannel:

$$6.6\,\Omega/\mu m \times 1\,mm \times 90\,\mu m = 0.60\,\Omega\,m \rightarrow 17\,mS/cm \tag{6.4}$$

The literature conductivity of 0.1 M Na_2SO_4 is 15.0 mS/cm [123]. There is also a small contribution to the conductivity from the buffer species.

While the electrode separation is very accurate in the lithography process, the channel height has been found to be not completely uniform. Variations of 5 µm in channel height are common for the SU8 channel master. This may contribute to uncertainties in predicting the solution resistance from the

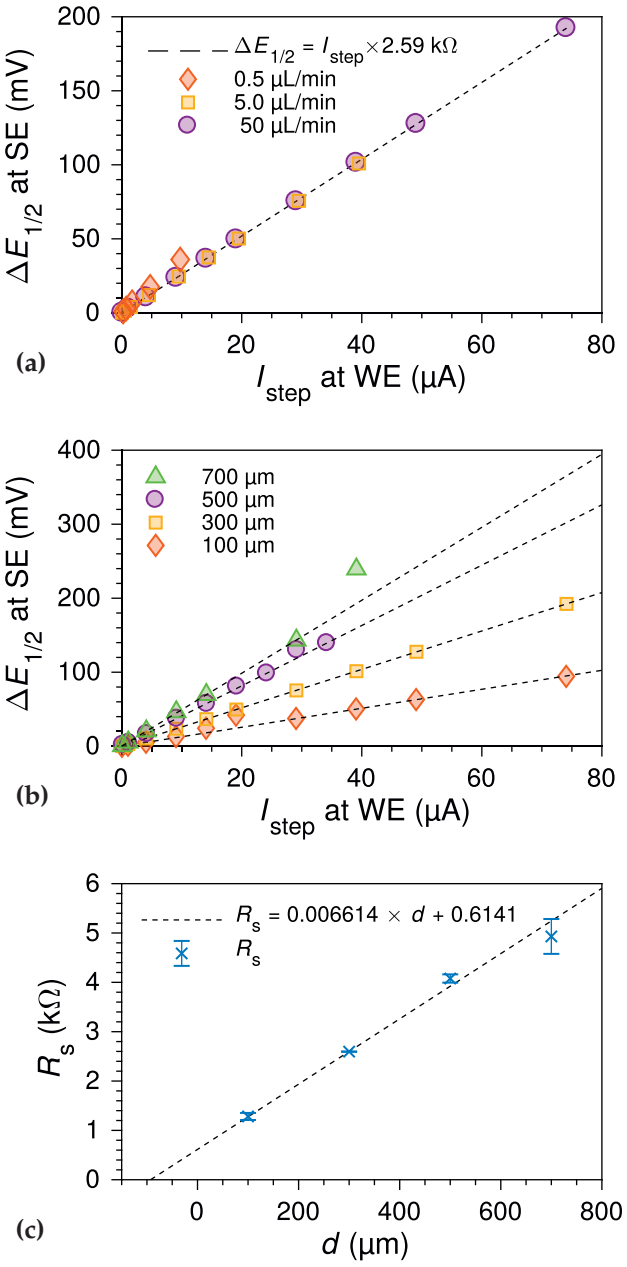

Figure 6.10: Measured shifts in the half-wave potential at different I_{step} currents. For the cell with electrode gap $d = 300\,\mu\text{m}$: (a) All flow rates. (b) Potential shifts for all electrode gaps at $50\,\mu\text{L/min}$. (c) the slopes of the linear fits plotted against the electrode spacing, including the 95% confidence intervals. The dotted line is a weighted LLS using 1/95% confidence interval weighting. The linear fit intersects the d-axis at $d = 93\,\mu\text{m}$.

electrode distance and electrolyte resistivity alone, as this is dependent on the channel cross-section. The method used in this work is a more reliable method to measure the solution resistance directly.

To confirm that the potential at the WE is completely independent on the processes on the downstream electrodes, the roles of the electrodes were switched, using a cell with $d = 100\,\mu m$. The half-wave potential of the oxidation of $Ru(bpy)_3^{2+}$was measured by cyclic voltammetry, while current steps up to $-50\,\mu A$ was applied to the SE. As expected, this had no effect on the potential of the reaction at the WE.

6.5 Potential shift tolerance

From the results above, it is possible to set some limits to how large the currents at the upstream electrode can be before the shifts in the solution potential at downstream electrodes have to be considered. A potential shift tolerance ΔE_{max} is defined as a limit below which the potential shift is considered to be negligible for the experiment. The corresponding maximum current I_{max} at the WE then becomes:

$$I_{max} = \frac{\Delta E_{max}}{R_s} = \frac{\Delta E_{max} \times w_{ch} \times h_{ch}}{\rho \times d_c} \tag{6.5}$$

or in terms of current density:

$$j_{max} = \frac{I_{max}}{w_{ch} \times w_{el}} = \frac{\Delta E_{max} \times h_{ch}}{\rho \times d_c \times w_{el}} \tag{6.6}$$

where:

$$\begin{aligned} w_{ch} &= \text{channel width} \\ h_{ch} &= \text{channel height} \\ \rho &= \text{electrolyte resistivity} \\ d_c &= \text{electrode center-to center distance} \\ w_{el} &= \text{working electrode width} \end{aligned} \tag{6.7}$$

The cell used in this work with the highest value of I_{max} is the one with electrode separation $d = 100\,\mu m$ (i.e. $d_c = 200\,\mu m$). Equations 6.5 and 6.6 give a maximum current of $3.78\,\mu A$, or a current density of $3.78\,mA/cm$. For currents higher than this, potential shifts at the SE will be higher than the tolerance of $5\,mV$.

There are several possible methods for increasing the current density limit in electrochemical experiments. The simplest is to decrease the electrolyte

resistivity by increasing the supporting electrolyte concentration. A second option is to modify the cell design, using smaller electrodes and further decreasing the electrode gaps. It should be possible to produce features down to 10 µm reliably by the lithography process used here.

6.6 Conclusion

The major advantage with the placement of the reference electrode upstream of the working electrodes is that it allows for higher currents to pass through electrodes in the microchannel, while maintaining the accuracy of the measured electrode potentials. In this configuration, the solution potential at one electrode is not affected by currents applied to any downstream electrodes. The solution potential is affected by currents at any upstream electrodes, but this relationship is quantifiable, and it is possible to find current limits, below which this effect is negligible. This configuration is a significant improvement for electrochemical microfluidic cells, as it allows for measurements of higher currents with less inaccuracy due to potential distribution, enabling the study of electrocatalytic reactions in microfluidic cells.

For example, current densities up to 4 mA/cm were possible without the potential at the downstream electrode changing by more than 5 mV. It is possible to increase this by an order of magnitude using a more concentrated supporting electrolyte, or a smaller electrode.

Chapter 7
AC techniques

Abstract

The short mass transit times between electrodes in microfluidic electrochemical cells enables measurement of fast (AC) signals as well as slow (DC) signals via mass transport between electrodes. The measurement and isolation of a periodic current signal applied to the working electrode and measured at the sense electrode, is demonstrated in this chapter.

7.1 Introduction

One experimental possibility enabled by the small scale design and rapid mass transport between the electrodes in a microfluidic electrochemical cell, is the ability to generate an periodic concentration profile in the channel. By applying an periodic perturbation in the potential at the upstream working electrode, the concentration of the product species may have an periodic profile downstream of the working electrode.

The periodic concentration effect was studied in microfluidic cells in terms of mass transport impedance by Thomas Holm [72], and is described here in terms of AC voltammetry.

AC voltammetry, which is cyclic voltammetry with an additional periodic perturbation, could potentially be used in noisy environments where the DC current measured by the sense electrode is affected by other processes than the direct transport of reaction products from the working electrode.

This technique was originally investigated as a method of boosting the sensitivity of the sense electrode in the in-situ detection of methanol oxidation products in chapter 9, though this was impeded by the fast deactivation of the palladium electrode.

In this chapter the isolation of an AC current signal applied to the working electrode and measured on the sense electrode is demonstrated using

$Ru(bpy)_3^{2+}$as a model species.

7.2 Experimental

The general electrochemical setup and fabrication of microfluidic cells is described previously.

The electrochemical measurements was performed on a 100 µm working Pt electrode with 100 µm Pd sense electrode in a 55 µm high channel. An electrolyte with 5 mM $Ru(bpy)_3^{2+}$in 0.1 M H_2SO_4 was used as the model system to study this effect. Potentials were measured against the internal

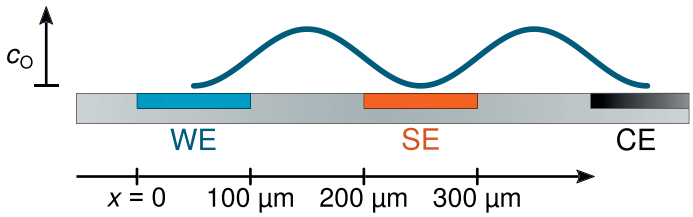

Figure 7.1: Illustration of the alternating concentration profile downstream of a point in the center of the the working electrode.

An AC voltammetry technique was applied to the working electrode. The potential was cycled between 0.8 and 1.4 V at 20 mV/s, with an added sinusoid with a peak amplitude of 10 mV at 7 Hz. The flow rate was 20 µL/min. Other parameters were tested as well. The sense electrode was kept at a constant 1.0 V to reduce the oxidized species back to $Ru(bpy)_3^{2+}$.

The measured currents on the working and sense electrodes were processed with the same principles as the digital lock-in amplifier [126] as described in section 7.3 using MATLAB. The lowpass filter used was a fourth order Butterworth filter with cutoff frequency 0.5 Hz.

7.3 Lock-in amplification

Mathematical description of phase independent digital lock-in amplification of an AC+DC signal:

For an ideal ac+dc current signal:

$$\begin{aligned} Is &= I_{DC} + I_{AC} \\ &= I_{DC} + A\sin(\omega t + \theta_s) \end{aligned} \tag{7.1}$$

where:

$$\omega = 2\pi f_r \tag{7.2}$$

f_r is the frequency of the AC component in the measured current on the sense electrode, which is set by the working electrode. We define sine and cosine wave reference signals with same frequency as the AC component of the current:

$$y_1 = \sin(\omega t + \theta_r) \tag{7.3}$$
$$y_2 = \cos(\omega t + \theta_r) \tag{7.4}$$

The current is multiplied with each reference signal and run the product through a low pass filter. The phase independent result is found by taking the root of the two squared components:

$$\begin{aligned} Is \times y_1 &= I_{DC} \sin(\omega t + \theta_r) + \frac{A}{2}(\cos(\theta_s - \theta_r) + \cos(2\omega t + \theta_s + \theta_r) \\ &\xrightarrow{lowpass} \frac{A}{2}\cos(\theta_s - \theta_r) \end{aligned} \tag{7.5}$$

$$\begin{aligned} Is \times y_2 &= I_{DC} \cos(\omega t + \theta_r) + \frac{A}{2}(\sin(\theta_s - \theta_r) + \sin(2\omega t + \theta_s + \theta_r) \\ &\xrightarrow{lowpass} \frac{A}{2}\sin(\theta_s - \theta_r) \end{aligned} \tag{7.6}$$

$$\begin{aligned} R &= \sqrt{\left(\frac{A}{2}\cos(\theta_s - \theta_r)\right)^2 + \left(\frac{A}{2}\sin(\theta_s - \theta_r)\right)^2} \\ &= \frac{A}{2} \end{aligned} \tag{7.7}$$

The result is a continuous function for the amplitude of the ac-component of the current, and the calculation is independent of any phase difference between the measured signal and the reference signals. A real measured current would also have a other noise components, e.g. the 50 Hz hum from the mains or the flow fluctuations from the pump, though these are also filtered out as long as the frequency is different enough from the applied AC signal.

7.4 AC working-sense voltammetry

Figure 7.1 illustrates the concentration oscillations from a point in the center of the working electrode. As real electrodes have nonzero widths, the oscillations from different parts of the electrode will have different phases, largely dependent on the transit time from the different parts of the electrode to a point downstream of the electrode. This will "smudge" the concentration profile in the channel. Too high frequencies may not generate any periodic concentration profile. The measurement of the current is also averaged over the width of the sense electrode, which decreases the measured amplitude further. Detection of the AC signal requires that the frequency of the signal is not too high compared to the inverse of the transit time discussed in section 4.3.4. The

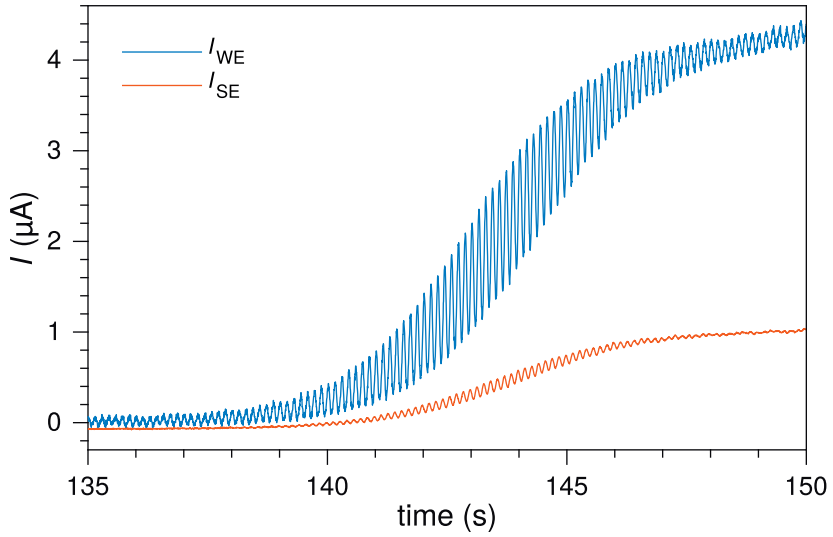

Figure 7.2: Unfiltered AC+DC currents. Raw current of the Pt working (20 mV/s + 10 mV at 7 Hz) and Pd sense electrode (constant 1 V) for one half cycle.

initial transit time for this geometry and flow rate is ∼40 ms while it takes ∼140 ms for steady-state detection. The applied frequency should also avoid the pump noise frequencies, which in this specific case at 20 µL/min is at 40.3 and 10.1 Hz.

Figure 7.2 shows the raw current measured at the working and sense electrodes. Both the AC and the DC components of the mass transport from the working to the sense electrode are measured. For a reversible species, the amplitude of the AC component of the current is related to the slope of the voltammogram. The surface oxide also contributes to the measured current, as the potential is in the oxide region of platinum.

Figure 7.3 shows a comparison of the amplitudes of the working and sense electrode currents. At the lower potentials, there is a constant periodic signal from the surface oxide on the Pt electrode, while the AC response on the sense electrode is zero. The sense electrode amplitude then follows the curve for the working electrode closely. The magnitude of the response is under half of the DC response (i.e. collection efficiency), due to the averaging of the signal at this frequency and flow rate. The signal may be improved by optimizing the cell towards lower transit times.

The ringing effect from numerical lowpass filtering means that the sampling time must be relatively large compared to the period of the AC signal, so this method was unsuccessful in formic acid detection in chapter 9, as measurements at constant potentials lead to too rapid deactivation of the sense electrode.

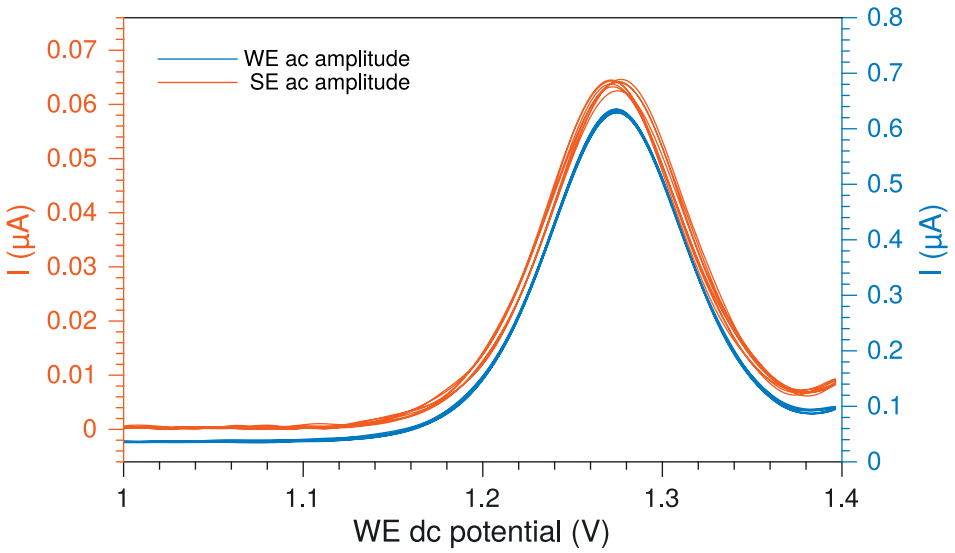

Figure 7.3: AC amplitude of the measured current on the working and sense electrodes

7.5 Conclusion

The short mass transit times between electrodes in microfluidic electrochemical cells enables a novel experimental technique by detection of both periodical (AC) and constant (DC) concentration of a species generated on the working electrode. By using the same operating principle as the digital lock-in amplifier it is possible to isolate a continuous function for the amplitude of the periodical component of the signal of known frequency, filtering out both the DC signal and periodic noise with different frequencies.

Part II

Investigation of methanol oxidation through downstream electrochemical measurement of the soluble products

Chapter 8
Oxidation of formic acid and formaldehyde on palladium

Abstract

One method of increasing the understanding of the methanol oxidation reaction, is to study the release of the soluble intermediates, formic acid and formaldehyde. This can be done using a palladium electrode located downstream of the working electrode. In order to use the palladium electrode as a sensor electrode, the oxidation mechanisms of these species must be understood on their own. In this chapter, the electrooxidation of HCOOH and HCHO on palladium in acidic electrolytes is studied by electrochemical methods, in solutions both with and without additional methanol, with the objective of quantitative analysis. The oxidation of both these species suffer from relatively rapid deactivation of the Pd electrode, and currents at constant potential conditions indicate only a fraction of the available species concentrations.

Oxidation of formic acid is possible at or close to mass transport limited currents by either aggressively cycling or stepping the electrode to facilitate the release of Pd^{2+}, or by addition of Pd^{2+} to the system. The oxidation of formaldehyde is more sluggish. By stepping the palladium electrode directly to lower potentials, it is possible to oxidize formic acid at a high rate, while having a negligible current contribution from formaldehyde oxidation. These methods are utilized for in situ measurements of methanol oxidation products in the next chapter.

8.1 Introduction

Methanol is a candidate fuel for use in low temperature and portable fuel cells (DMFCs), though the slow rate of the methanol oxidaton reaction and catalyst requirements are limiting factors for the commercial application of the DMFC.

One approach to increasing the understanding of the MOR, is to study the oxidation intermediates and products.

Several methods have been applied to study the oxidation mechanism, such as FTIR [11, 13, 127–130] and DEMS [131–134]. A qualitative understanding of the reaction is crucial in designing electrocatalysts kinetically in favour of complete oxidation.

In this thesis, the soluble and electroactive reaction intermediates in the MOR, formic acid and formaldehyde, are studied using electrochemical methods. The palladium electrode is especially interesting for this application as it is active towards both formic acid and formaldehyde, but does not oxidize methanol in acidic electrolytes.

In order to accurately detect and quantify formic acid and formaldehyde as oxidation products of methanol, an understanding of the oxidation mechanisms of these species on palladium, specifically in acidic media, is required. Much work has been put into the study of formic acid on palladium due to its promise as a fuel for electrochemical energy conversion. Work on lower concentrations, and oxidation of these species in solutions also containing methanol, is more scarce.

The oxidation of formic acid on palladium is an electrocatalytic reaction, and is subject to its own reaction kinetics and electrode deactivation. In order to directly quantify the amount of formic acid released from the Pt WE during methanol oxidation, the oxidation of formic acid must be mass transport limited. This requires a very high activity of the Pd electrode, preferably at constant potential.

Alternatively, the detection of formic acid and formaldehyde may be compared to standardized solutions of known concentrations, though this probably requires modelling of the mass transport from the WE to the SE to correlate bulk concentrations with the generated concentrations.

The mass transport limited current for 1 mM HCOOH at 5 µL/min for a 1 mm × 100 µm electrode at 25 °C is 2.4 µA from equation 4.17(note that it is linearly dependent on concentration), using the diffusion coefficient of formic acid in water, $1.516 \times 10^{-5}\,\mathrm{cm^2/s}$, from the literature [135]. In practice the diffusion coefficient is likely slightly lower due to lower room temperature in the lab.

For formic acid, the following reaction mechanism has been suggested for electrooxidation on palladium [136, 137], with the formation of an adsorbed species ($C(OH)_2$) which is slow to oxidize further.:

$$\mathrm{HCOOH} \longrightarrow \mathrm{COOH(ads)} + \mathrm{H^+} + \mathrm{e^-} \tag{8.1}$$

$$\mathrm{HCOOH} + \mathrm{COOH(ads)} \longrightarrow \mathrm{C(OH)_2(ads)} + \mathrm{CO_2} + \mathrm{H^+} + \mathrm{e^-} \tag{8.2}$$

$$\mathrm{C(OH)_2(ads)} \longrightarrow \mathrm{CO_2} + 2\,\mathrm{H^+} + 2\,\mathrm{e^-} \tag{8.3}$$

along with the more direct pathway

$$\mathrm{COOH(ads)} \longrightarrow \mathrm{CO_2} + 2\,\mathrm{H^+} + 2\,\mathrm{e^-} \tag{8.4}$$

following step 8.1.

The adsorbed species $C(OH)_2$ binds to two surface sites, and its slow removal is responsible for the deactivation of the palladium electrode, as well as leading to high variability in measurements of the oxidation current [138–142].

Palladium(II) ions are suggested to have an important role in retaining the activity of the reaction [138]. Pd^{2+} in solution, either electrogenerated [142] or added to the analyte [138] reactivate the palladium electrode surface by reacting with the adsorbed species:

$$\mathrm{C(OH)_2(ads)} + \mathrm{Pd^{2+}} \longrightarrow \mathrm{CO_2} + 2\,\mathrm{H^+} + \mathrm{Pd^0} \tag{8.5}$$

Electrogenerated Pd^{2+} comes from the palladium electrode itself, usually originating from dissolution during the reduction of surface oxides. The release of Pd^{2+} is highly dependent on the state of the oxide layer, which is affected by both the time and potential of the electrode during oxidation [142–144] as well as the state (e.g. roughness) of the electrode.

Formaldehyde oxidation on palladium is proposed to follow the same reaction mechanism as on platinum alloys, which is dehydrogenation forming adsorbed CO. If the potential is high enough, the CO is further oxidized to CO_2. The full oxidaton requires an oxygen donor, such as H_2O or OH.

$$\mathrm{HCHO} \longrightarrow \mathrm{CO(ads)} + 2\,\mathrm{H^+} + 2\,\mathrm{e^-} \tag{8.6}$$

$$\mathrm{CO(ads)} + \mathrm{H_2O} \longrightarrow \mathrm{CO_2} + 2\,\mathrm{H^+} + 2\,\mathrm{e^-} \tag{8.7}$$

Any effect of added Pd^{2+} was not found for formaldehyde oxidation [141] on palladium under similar conditions.

In this chapter, the oxidation of formic acid and formaldehyde on palladium is studied by electrochemical methods, with the goal of using the Pd electrode as a sense electrode for in situ methanol oxidation experiments. Various electrochemical techniques are applied to understand the system, and develop methods to possibly quantify and identify the products of methanol oxidation.

8.2 Experimental

All measurements shown in this chapter were performed in microfluidic cells with 100 µm electrodes, with 100 µm electrode gaps. The electrodes are a palladium electrode (SE) downstream of a platinum (WE) electrode, with a Pt counter electrode situated downstream of both. The fabrication of microfluidic

cells and the general electrochemical setup is described in chapter 2. The palladium hydride reference electrode is located in a side channel upstream of the main electrodes. The reference electrode was charged as previously described in chapter 5, first at the start of the experiment, then recharged after $\sim$ 4 hours or if the potential was found to drift. The potential drift was controlled by comparing peak locations in fast cyclic voltammograms.

The base electrolyte was 0.1 M perchloric acid. Electrolytes of various concentrations were prepared from concentrated solutions of methanol, formic acid, and a dilute solution of formaldehyde (also containing 10-15% methanol). The working electrodes were cycled at 500 mV/s in the base electrolyte at the start of the experiments until the voltammograms were stable. This took typically around 30 cycles for Pt and at least 100 cycles for Pd.

The flow rate was 5 µL/min unless otherwise specified. Cyclic voltammetry was performed in various electrolytes, starting with clean 0.1 M $HClO_4$ electrolyte, then 0.1 M CH_3OH, before repeating in increasing concentrations of formic acid or formaldehyde.

The electrodes were cycled, starting at 500 mV/s for at least 30 cycles until stable, then continuously cycled at decreasing scan rates. The upstream Pt electrode was cycled before the Pd electrode, so some trace levels of methanol oxidation products may have been present even in the electrolyte with methanol only.

The other electrochemical techniques were performed in solutions without methanol. For measurements at constant potentials, the electrode was cycled at 20 mV/s until stable, before the potential was stopped at the given potential, typically on the reverse scan.

8.3 Cyclic voltammetry

8.3.1 Formic acid

Figure 8.1 shows cyclic voltammograms for the Pd electrode, cycled at 20 mV/s between 0.30 and 1.45 V, in various concentrations of formic acid in addition to 0.1 M methanol. A closer view of the voltammograms for the lower concentrations is plotted separately.

Starting at the upper vertex potential (1.45 V) on the reverse (negative going) scan, the Pd electrode is active towards formic acid oxidation immediately after the reduction of palladium oxide begins, and palladium surface sites are formed. Formic acid concentrations down to 0.1 mM, are detectable by cyclic voltammetry at 20 mV/s. For higher concentrations there is a pre-peak at 0.6 V before the main peak. The main peak shifts towards higher potentials as the concentration is decreased, from 0.4 V in 0.1 M formic acid. The electrode remains active down to the lower vertex of 0.30 V. On the forward scan, the oxidation peak is at about 0.4 V for all concentrations, though at

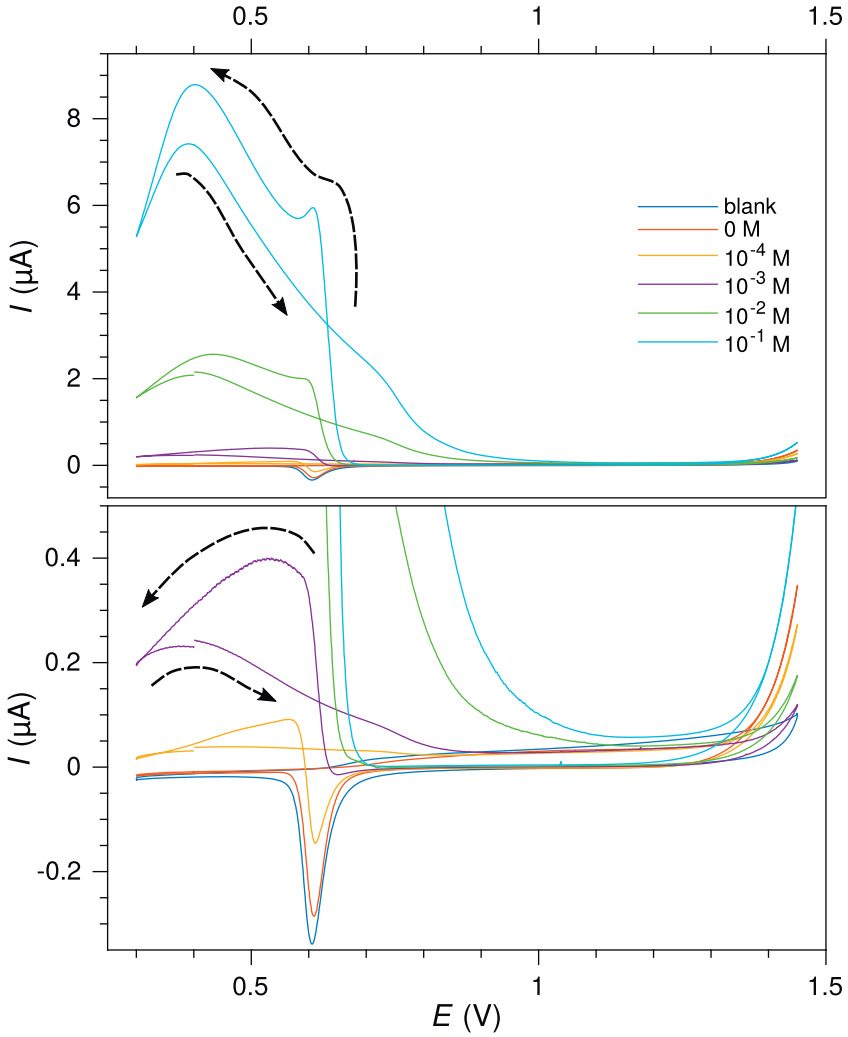

Figure 8.1: Cyclic voltammetry on Pd at 20 mV/s in various concentrations of formic acid added to 0.1 M methanol. Voltammogram in the base electrolyte for comparison. The upper plot shows a closer view of the voltammograms at lower concentrations. Arrows indicate scan direction.

lower concentrations it is not very prominent. The forwards peak was found to always be lower than the reverse peak for slow scan rates (below 50 mV/s). Palladium oxide is passive towards formic acid oxidation, so the current drops as the oxide is formed above 0.8 V. Closer to the upper vertex, above 1.35 V, the palladium oxide covered electrode oxidizes methanol, in addition to being slightly active towards high concentrations of formic acid, as can be seen from the voltammograms for 0 M formic acid (red) and 0.1 M formic acid (light blue) compared to the blank electrolyte.

Figure 8.2 shows the effect of different scan rates in 1 mM formic acid. For

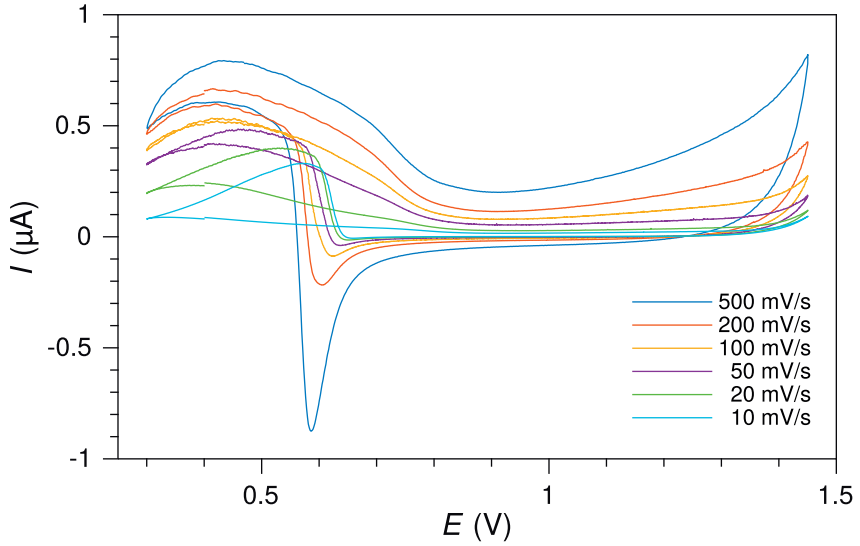

Figure 8.2: Cyclic voltammograms from various scan rates on Pd in 1 mM formic acid and 0.1 M methanol.

higher scan rates, above 100 mV/s, the forward scan peak is higher than the reverse peak. For the slower scan rates, the forward scan peak is less prominent, and it is indistinguishable at 10 mV/s. The reverse peak current decreases with the scan rate, though the peak current at 500 mV/s is only twice as high as 10 mV/s, at 0.6 mA.

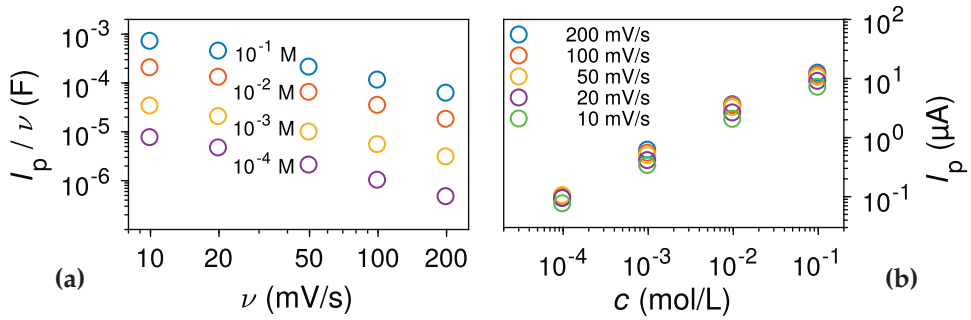

Figure 8.3: Analysis of the reverse scan peak current from cyclic voltammetry of formic acid on palladium, as a function of scan rate and concentration. (a) Logarithmic plot of peak current divided by scan rate vs. the scan rate in various concentrations of formic acid. (b) Logarithmic plot of peak current vs. formic acid concentration at various scan rates.

Figure 8.3a shows the reverse scan peak current (I_p) at the different concentrations, normalized by the scan rate, and plotted as a logarithmic plot. There is a linear relationship of $\log(I_p/\nu)$ vs. $\log(\nu)$ with the slope -0.82. For a completely mass transport limited process, this slope would be equal to -1,

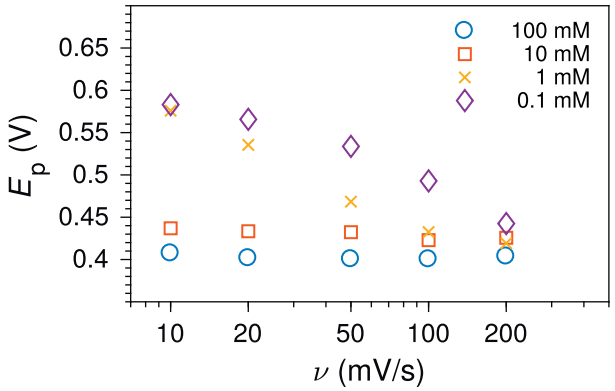

Figure 8.4: Peak potential from cyclic voltammetry in various concentrations of formic acid added to 0.1 M methanol.

as the peak current would be independent of the scan rate assuming the flow rate is high enough for the measurements to be at steady-state. Figure 8.3b is a logarithmic plot of the peak current vs. the concentration. For all the scan rates there is a linear relationship of $\log\left(I_\mathrm{p}\right)$ vs. $\log\left(c\right)$, with a slope of 0.70.

Figure 8.4 shows the reverse scan peak potential (E_p) plotted against the logarithm of the scan rate. For higher concentrations, the peak potential is relatively stable at 0.40 and 0.43 V for the 0.1 and 0.01 M formic acid solutions, but at the lower concentrations the peak potential shifts to higher potentials as the scan rate is lowered. At the lowest scan rates the reverse scan peak occurs directly after the cathodic surface oxide reduction peak.

The linear relationship in figure 8.3b shows that, with careful control of the treatment of the palladium electrode, following the same parameters for each different electrolyte, it is possible to obtain consistent and predictable and consistent data for measuring the formic acid concentration. However, small changes in the experimental parameters can give unpredictable results. The data presented above were measured in a continuous experiment in a single microfluidic cell, breaking only to switch electrolyte and recharge the reference electrode. Figure 8.5 shows four different voltammograms on 100 µm Pd electrodes at the same scanrate in 1 mM formic acid, with and without methanol, from different cells. The difference in the electrode activities may be due to slightly different conditioning of the Pd electrode.

Figure 8.6 shows the effect of changing the upper vertex potential in cyclic voltammetry at 20 mV/s on the palladium electrode in 1 mM formic acid without methanol. The Pd electrode was cycled continuously, starting with an upper vertex potential of 1.45 V, and decreasing the vertex potential every 2 cycles. The reverse scan peak current starts off high, at 0.90 µA, and decreases rapidly as the upper vertex potential is decreased. Cycling the electrode below 1.10 V, the anodic peak is barely visible. The location of the peak is also shifted

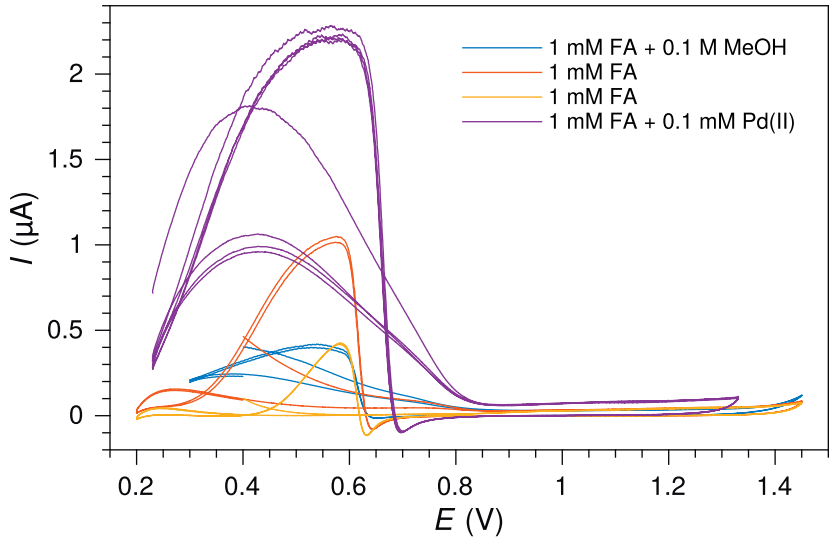

Figure 8.5: Voltammograms on Pd at 20 mV/s in 1 mM HCOOH under different conditions. The addition of Pd^{2+} is discussed further in section 8.7

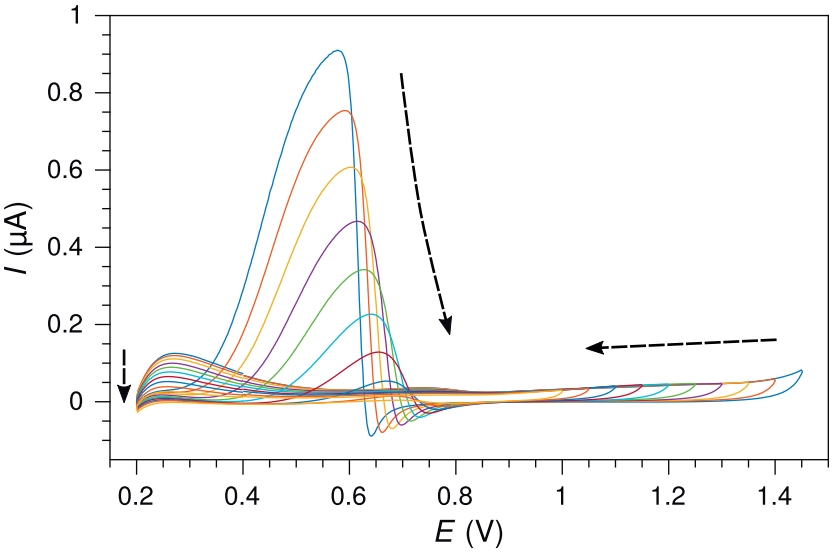

Figure 8.6: Effect of changing the upper vertex potential on cyclic voltammograms of Pd in 1 mM formic acid. Arrows indicate decreasing upper vertex potentials, from 1.45 to 1.00 V, in the order they were recorded.

to higher potentials, as the reduction of palladium oxide occurs at higher potentials when the upper vertex potential is lower. There are no special features (e.g. stripping peaks) in the forward scan. This shows that the reactivation of

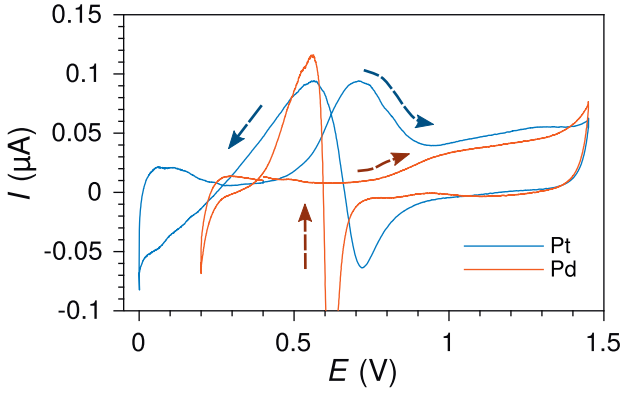

Figure 8.7: Comparison of voltammograms on Pt and Pd electrodes at 20 mV/s in 0.1 mM formic acid.

the Pd electrode towards formic acid requires the electrode to be cycled into the oxide region, and that scanning the electrode to higher potentials makes the Pd electrode more active in formic acid oxidation once the palladium oxide is reduced. This is consistent with the suggested mechanism in equation 8.5, that palladium (II) ions in solution is essential in removing poisoning species from the palladium surface. It is known that higher oxidation potentials on palladium causes more Pd^{2+} ions to be released from the electrode, both before and during the reduction of the surface oxide [142–144].

Figure 8.7 shows a comparison of the cyclic voltammograms for 0.1 mM HCOOH on palladium and platinum electrodes. While the activity of the noble metals in HCOOH oxidation is similar, the difference in the reaction mechanism is very clear from the forward scan. The oxidaion of formic acid in the platinum voltammogram is very similar to methanol oxidation, with the forward scan peak at 0.7 V consistent with at least partial CO coverage on the surface. Palladium does not have this stripping peak, and is only reactivated on the reverse scan after a full cycle into the oxide region.

8.3.2 Formaldehyde

Figure 8.8 shows cyclic voltammograms at 20 mV/s for the Pd electrode in various concentrations of formaldehyde in addition to 0.1 M methanol. The top plot shows a closer view of the lower concentrations. The electrode was cycled between 0.2 and 1.2 V.

During the reverse scan, oxidation of formaldehyde starts as soon as palladium oxide starts being reduced below 0.8 V. In 0.1 M formaldehyde there is a significant oxidation current also in the oxide region. At lower concentrations ($\leq$ 1 mM) the cathodic palladium oxide reduction peak is still visible. The reverse scan peak occurs directly after the reduction of palladium oxide, at

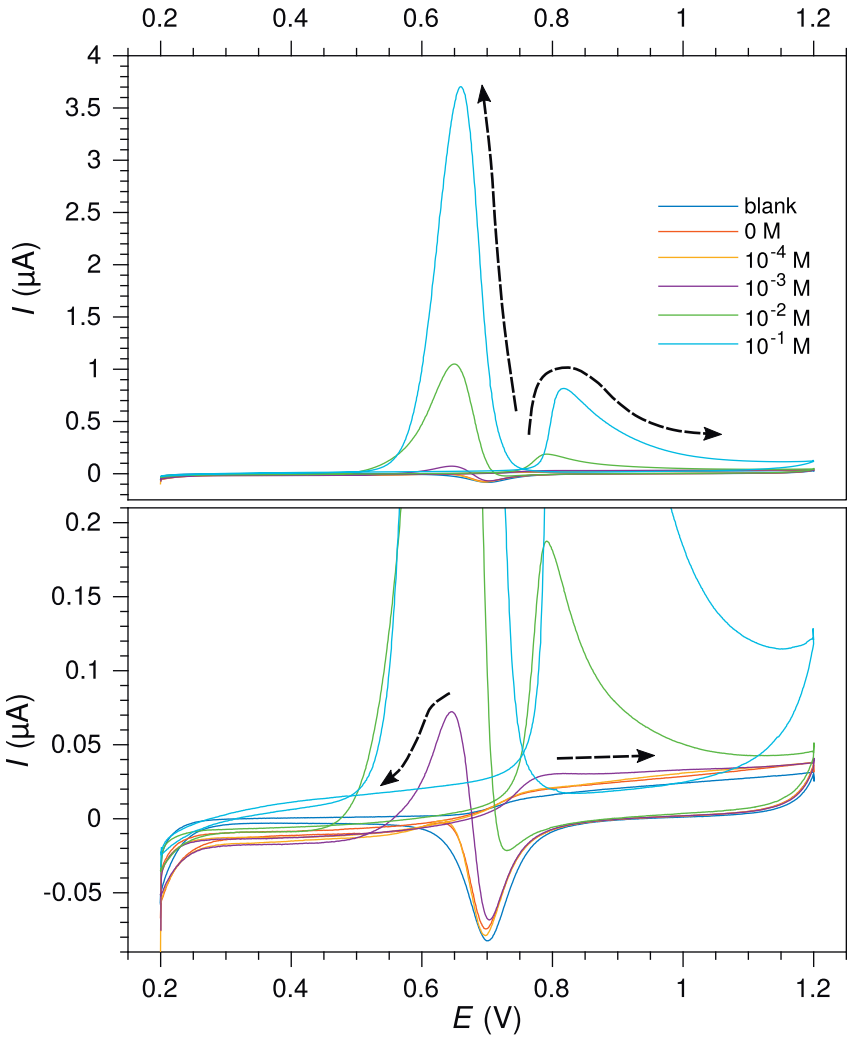

Figure 8.8: Cyclic voltammograms for Pd at 20 mV/s for various concentrations of formaldehyde added to addition to 0.1 M methanol. The arrows indicate scan direction.

0.66 V, and does not seem to change at all with the changing concentration. After the peak, the electrode is rapidly deactivated, and the oxidation current is negligible below 0.5 V. On the forward scan, the electrode is mostly passive until the starting potential of palladium oxidation, ∼0.70 V. In the higher concentrations, there is a large oxidation peak, at 0.82 V for 0.1 M, and 0.79 V for 0.01 mM. For lower concentration there is no real peak, though the current in the oxide region is generally slightly higher than for the blank electrolyte.

In 0.1 M formaldehyde, the reverse scan peak current is 3.7 µA, about half of the peak current in the corresponding formic acid concentration. The forward scan peak is at 0.82 µA. In 1 mM formaldehyde, the reverse scan peak current

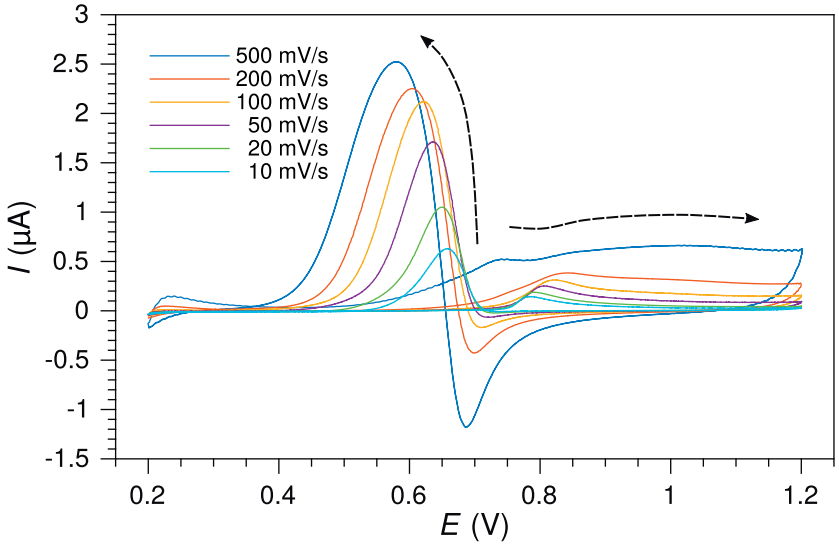

Figure 8.9: Cyclic voltammograms from various scan rates on Pd in 10 mM formaldehyde and 0.1 M methanol. The arrows indicate the scan direction.

is 72 nA, which is less than one fifth of the peak current in 1 mM formic acid. The current response of formaldehyde is less than the response from formic acid, and the difference is magnified for lower concentrations.

Figure 8.9 shows the effect of varying scan rates on the voltammograms in 10 mM formaldehyde. Higher scan rates lead to higher reverse scan peaks, and shift the location of the peaks to lower potentials.

Like the oxidation of formic acid, the cyclic voltammograms from oxidation of formaldehyde are very dependent on the oxidation potentials of the palladium electrode, but here the effect if opposite. Voltammograms at 20 mV/s in 1 mM formaldehyde are plotted in figure 8.10, compared with the voltammograms for the base electrolyte. An upper vertex potential of 1.20 V leads to a reverse scan peak that is twice as high as for 1.45 V. The charge estimated by comparing with the blank cycle is higher as well. The palladium oxide formed at higher potentials requires more negative potentials to be reduced, and by the time free Pd sites are formed and available oxide, the lower potentials electrode is less active towards formaldehyde oxidation at the lower potentials. The formaldehyde oxidation is hidden by the surface oxide reactions. Again, there is no forward scan peak in either of the cycles, though there is general increase in the anodic current in the oxide region, compared to the blank cycles.

8.3.3 Formic acid + formaldehyde

Figure 8.11 shows the cyclic voltammograms for the Pd electrode in a mixture of both formic acid and formaldehyde at 10 mM of each. Comparing

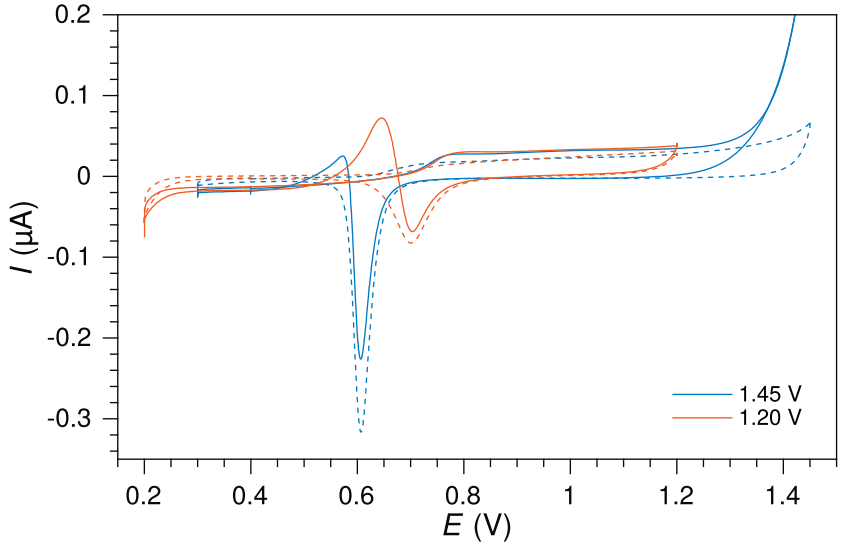

Figure 8.10: Effect of changing upper vertex potential in the HCHO voltammogram. Cyclic voltammetry at 20 mV/s on the Pd electrode in 1 mM formaldehyde. Dashed lines show the voltammogram in the clean 0.1 M perchloric acid electrolyte.

to the voltammograms for the individual species, it is clear that formic acid contributes with the majority of the oxidation current, while the presence of formaldehyde accelerates the deactivation of the electrode, decreasing the sensitivity of the electrode towards both formic acid and formaldehyde. This is especially visible on the forward scan, where the current drops to a fraction of the reverse scan peak for all but the fastest scan rates.

In situ quantification of formaldehyde in solutions also containing formic acid seems difficult, as the oxidation current is masked by the more active species. The most obvious effect of formaldehyde in the cyclic voltammogram is an increase in the deactivation, though this is not a reliable measurement.

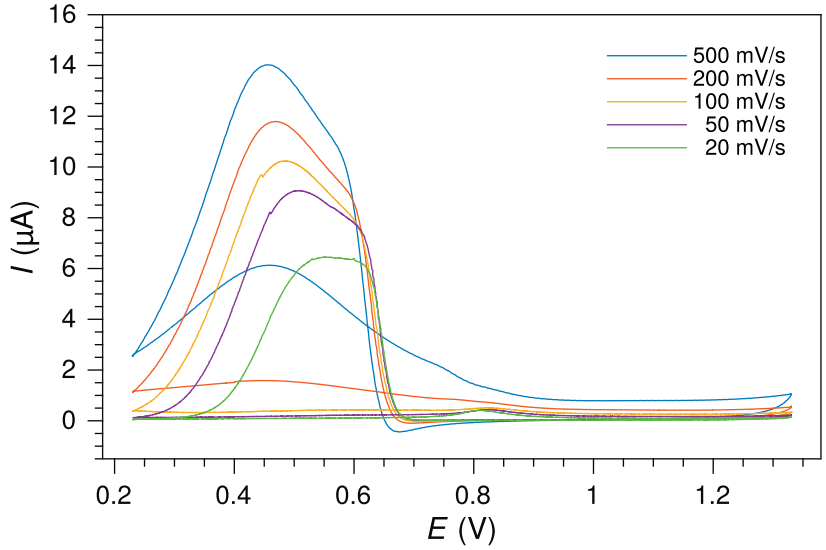

Figure 8.11: Cyclic voltammetry at various scan rates on the Pd electrode in a solution with 10 mM HCOOH and HCHO in 0.1 M $HClO_4$.

8.4 Deactivation of Pd at constant potential

The deactivation of the palladium electrode towards formic acid oxidation at constant potential was studied in 0.1 mM formic acid at various potentials and flow rates. For reference, the calculated mass transport limited current for this concentration of formic acid at 5 µL/min is 0.24 µA using equation 4.17. The potential was cycled at 100 mV/s until stable voltammograms were produced, and then stopped during the reverse scan at a potential where formic acid is oxidized. Figure 8.12 shows that there is only a slight dependence of the deactivation rate on the potential of the electrode. In all cases the current drops to close negligible oxidation currents within 30 to 40 s after the cycling is stopped. Note that the current does not drop *completely* to zero, but the current at the end is only a fraction of the initial current.

Figure 8.13 shows the deactivation at flow rates from 1 to 50 µL/min, for a palladium electrode held at 0.55 V, which was the peak potential on the reverse scan in the cyclic voltammograms. The first thing to note is that the peak current, i.e. the initial current in these plots, is not appreciably higher for increased flow rates. The initial current at 20 µL/min is less than double of the current at 1 µL/min.

The rate of deactivation is clearly much higher for higher flow rates. After 15 seconds at constant potential the oxidation current is actually highest for the lowest flow rate. At the faster flow rates the current drops to below zero due to trace amounts of dissolved oxygen in the electrolyte being reduced at

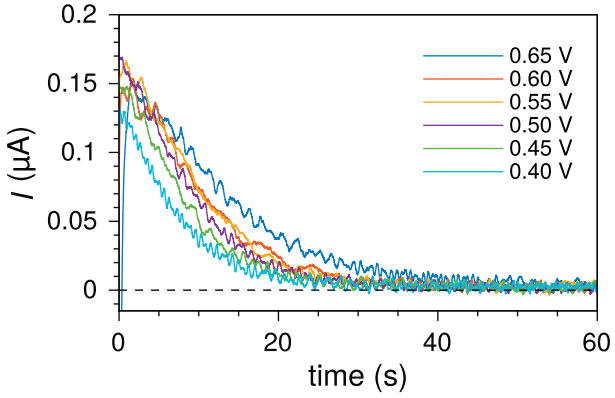

Figure 8.12: Measured current on the Pd electrode at a constant potential after cycling to activate the electrode. Flow rate 5 µL/min and electrolyte 0.1 mM HCOOH.

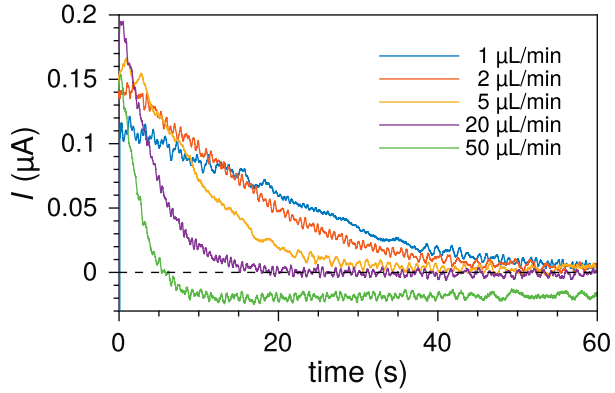

Figure 8.13: Measured current on the Pd electrode held at 0.55 V at various flow rates in 0.1 mM HCOOH.

this potential.

The same effects were also observed in a large volume 3-electrode cell experiment on a palladium disk electrode in 1 mM formic acid at rotation rates from 0 to 500 rpm (not shown).

Due to this rapid deactivation of the formic acid oxidation on palladium, even in the best-case scenario with no other contaminants, quantification of formic acid at constant potentials seems difficult, as the measured oxidation current will only be a fraction of the mass transport controlled current.

8.5 Open circuit

When the palladium electrode is left at open circuit in a solution with formic acid the electrode potential drops rapidly, as formic acid is adsorbed and the first step of the oxidation reaction is dehydrogenation.

$$\mathrm{HCOOH} \longrightarrow \mathrm{COOH(ads)} + \mathrm{H(ads)} \tag{8.8}$$

If the potential is kept above 0.25 V, hydrogen is oxidized and desorbed:

$$\mathrm{H(ads)} \longrightarrow \mathrm{H^+} + \mathrm{e^-} \tag{8.9}$$

but at open circuit the adsorbed hydrogen is absorbed into the palladium electrode, and the electrode potential decreases

$$\mathrm{H(ads)} \longrightarrow \mathrm{H(abs)} \tag{8.10}$$

The presence of absorbed hydrogen was confirmed by an anodic peak at $\sim$0.2 V on the initial cycle of a subsequent cyclic voltammogram (visible at low concentrations of formic acid). Brief ($<$30 s) periods at open circuit was found to have negligible impact on the electrode performance during the subsequent voltammograms, but after longer periods ($>$2 min), the measured oxidation current on the initial scan was lower than the following cycles. The reaction to form the deactivating species ($C(OH)_2$, equation 8.3) occurs together with the additional hydrogen being absorbed into the palladium electrode.

An example of the electrode being still active after a brief period at open circuit in formic acid is shown in the initial forward scan in figure 8.20 below.

In formaldehyde solutions, the same potential decay was observed, and the initial cycle of the following voltammetry indicated CO poisoning of the electrode:

$$\mathrm{HCHO} \longrightarrow \mathrm{CO(ads)} + 2\,\mathrm{H(ads)} \tag{8.11}$$

An example of this is is shown in the initial forward scan in figure 8.22 below.

8.6 Stripping experiments

In a microfluidic cell with multiple electrolyte inlets, it is possible to analyze surface poisoning species by switching out the electrolyte with clean electrolyte while maintaining the electrode potential. The difference between the initial cycle and subsequent cycles in the clean electrolyte shows the presence of any electroactive surface species remaining on the electrode surface after

the electrolyte switch. Of course this requires that the new electrolyte is not contaminated. As was seen previously in section 3.3.1, stripping experiments with CO worked poorly, as the PDMS absorbed CO from the saturated electrolyte and released it back into the clean electrolyte. Low concentrations of formic acid and formaldehyde were used to avoid too much contamination, and the subsequent scans are used to confirm that the electrolyte is relatively clean. These experiments were done with a branched inlet cell to allow for fast switching of electrolyte with a small dead volume (see section 4.4.3).

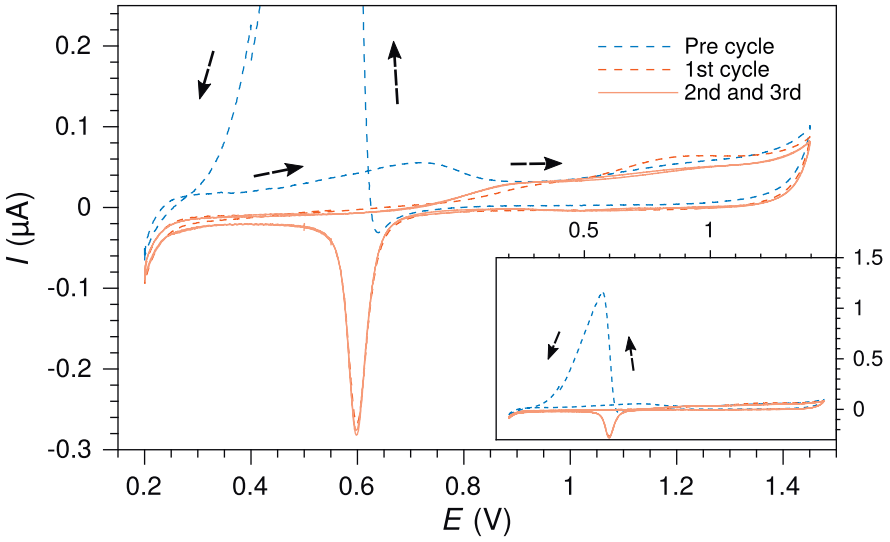

Figure 8.14: Stripping voltammetry at 20 mV/s from 1 mM formic acid on the Pd electrode. The potential was held for 1 min at 0.55 V at the end of the pre-cycle, while the current decreased from the peak current to close to zero.

Figure 8.14 shows a stripping experiment for 1 mM formic acid at 5 µL/min. The Pd electrode was cycled at 20 mV/s in the 1 mM solution, before the potential was held at 0.55 V, close to the peak potential. This potential was held for one minute, during which the current dropped to close to zero. The cell was then flushed with blank electrolyte for 3 minutes while keeping the Pd electrode at constant potential. The potential was then cycled at 20 mV/s, starting on the reverse scan.

There is no clear peak, but there is a slight increase in the anodic current around 1.2 V, which is slightly higher than even the current in the pre-cycle, indicating that this coverage increases as the electrode is deactivated at 0.55 V. However, the charge passed is much too low for this species to have complete coverage of the electrode.

The adsorbed species did not block the adsorption of hydrogen on the Pd electrode at lower potentials in any significant way, as indicated by the unchanged hydrogen adsorption (and subsequent absorption), even with the

prescence of 1 mM formic acid.

Stripping experiments in higher concentrations of formic acid than 1 mM failed due to contamination of the electrolyte by release of formic acid taken up by the PDMS, which was measured on the 2nd and 3rd cycles under flow of the "clean" electrolyte.

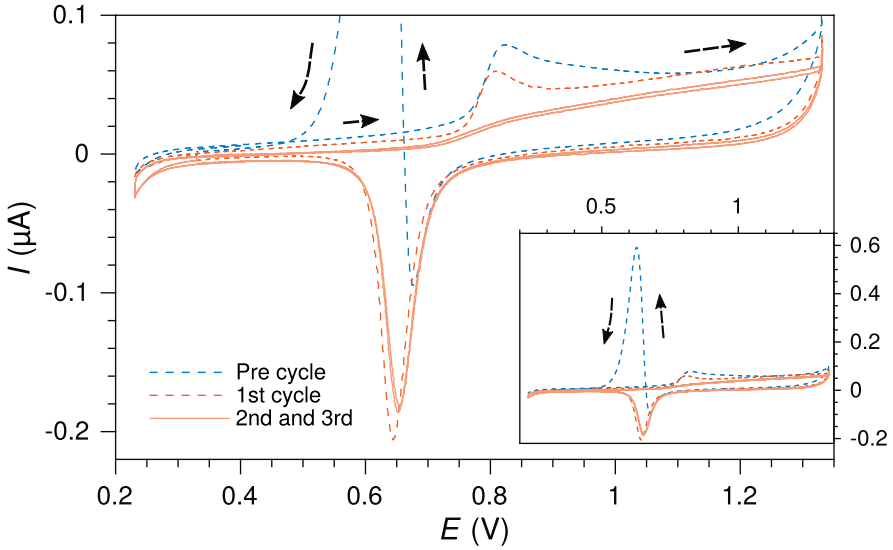

Figure 8.15: Stripping voltammetry at 20 mV/s from 10 mM formaldehyde on the Pd electrode. The potential was held at 0.33 V at the end of the pre-cycle, first for one minute in the formaldehyde solution, then for another minute while the channel was flushed with clean electrolyte, and then cycled again.

Figure 8.15 shows a stripping experiment from 10 mM formaldehyde. The Pd electrode was cycled in the same way as above, and the potential was held constant at 0.33 V while the electrolyte was switched. At this point the activity of formaldehyde has reduced to zero and the stripping cycle should show the species adsorbed at this point in the cycle. The stripping scan does indeed show a peak at 0.8 V, which is consistent with adsorbed CO on the surface, though not of the magnitude that indicates complete coverage of the surface (compare with figure 3.8, page 40). The peak is also consistent with the regular voltammograms of formaldehyde on Pd. The oxidation current is consistently higher in the oxide region during the first cycle. This excess oxidation charge is not accounted for in the oxide reduction charge on the reverse scan, suggesting that this comes from irreversible oxidation of organic residues on the surface.

8.7 Addition of palladium (II) ions

In order to further study the effect of Pd^{2+} ions in solution on the activity of the Pd electrode towards formic acid oxidation, and the deactivation of the electrode, additional Pd(II) ions were added to the formic acid solution. The electrolyte was prepared by adding 0.1 mM $Pd(NO_3)_2$ to a solution of 1 mM formic acid and 0.1 M $HClO_4$. At this concentration, the Pd ions added a weak yellow color to the electrolyte. $Pd \cdot^{2+}$ is known to be reduced in a homogeneous reaction in formic acid:

$$HCOOH + Pd^{2+} \longrightarrow CO_2 + 2\,H^+ + Pd^0 \tag{8.12}$$

In higher concentrations of formic acid, as well as in methanol and formaldehyde, the Pd^{2+} ions were reduced by the organic molecules, sometimes in a matter of minutes. The solution became clear, and precipitated Pd particles sank to the bottom of the sample glass. However, in formic acid concentrations of 1 mM and below, Pd^{2+} was found to be stable in solution for weeks, more than sufficient to perform the experiments. The test solution kept its yellow color and no precipitated particles were observed a week after the solution was used.

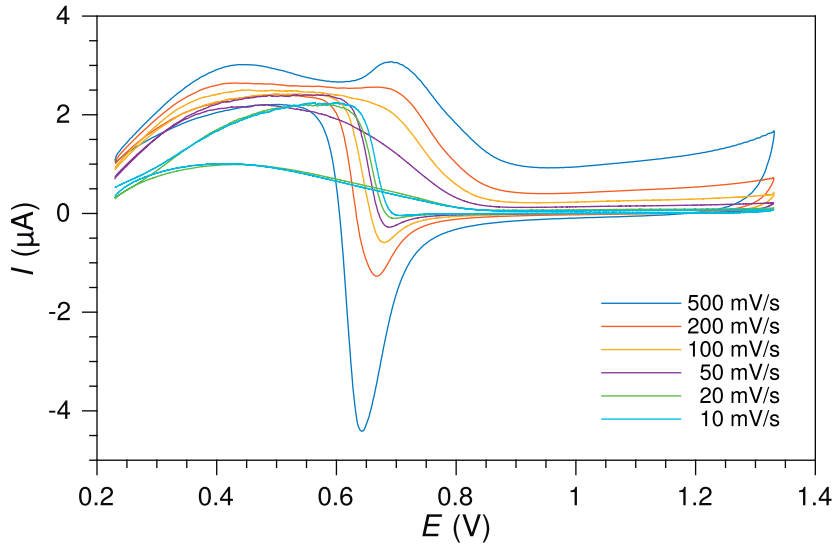

Figure 8.16: Voltammograms at various scan rates on a 100 µm Pd electrode in 0.1 mM $Pd(NO_3)_2$, 1 mM HCOOH and 0.1 M $HClO_4$. Flow rate 5 µL/min

Figure 8.16 shows the cyclic voltammograms on the Pd electrode in the formic acid electrolyte with added Pd^{2+}. Compared to the voltammograms at the same conditions without added Pd^{2+} in figure 8.2, the effect is clear. The

activity towards formic acid oxidation is increased and the peak current at the reverse scan is virtually independent on the scan rate, indicating that the surface reaction is fast, and that the process is only limited by mass transport to the electrode at steady-state. The deactivation of the electrode seems to be much slower, and there is still a significant peak on the forward scan at the slowest scan rate, 10 mV/s, though it is still not good enough to expect good sensitivity at constant potential, as some deactivation still takes place.

Another indication that the reaction is, at least briefly, mass transport controlled under addition of Pd^{2+}, is that the same syringe pump noise as seen with the reversible $Ru(bpy)_3^{2+}$species, and discussed in section 4.4, was seen as perturbations in the current around the reverse scan peak.

Unfortunately, the addition of $Pd(NO_3)_2$ to the microfluidic cell during the experiments had some irreversible effects on the microfluidic cell. The counter electrode, as well as some of the glass in the channel downstream of it, was completely black at the end of the cycling, covered with Pd particles. This is hardly surprising, as it would be kept at highly a cathodic current flows trough the CE to counter the anodic processes on the working electrode, so Pd^{2+} is reduced and deposited. The palladium working electrode showed an increase in the electrochemically active area, as measured qualitatively from the stable cyclic voltammograms before and after the experiment (figure 8.17), by at least three times the original area. A platinum electrode, which was just kept at open circuit during the experiment, showed a significant change from being palladized (figure 8.18), with semi-reversible current peaks at –20 mV 10 times the size of the hydrogen adsorption peaks. The large peaks are probably due to generated hydrogen trapped by palladium on the platinum electrode surface, and the magnitude was found to be close to proportional to the scan rate, meaning the total charge of these peaks are surface area dependent. The current at the lower vertex point is evolution of hydrogen gas. The voltammograms of the palladized electrodes were found to be stable in the given potential region.

Addition of Pd^{2+} can not be used to boost the *in situ* electrochemical detection of methanol oxidation products, due to the effect it would have on the Pt working electrode. However one possible way to boost the sensitivity of the Pd electrode is to treat it with $Pd(NO_3)_2$ *before* the experiment to obtain a more active sense electrode. The Pt working electrode would then need to be protected by keeping it at anodic potentials, using another electrode as a "sacrificial" electrode.

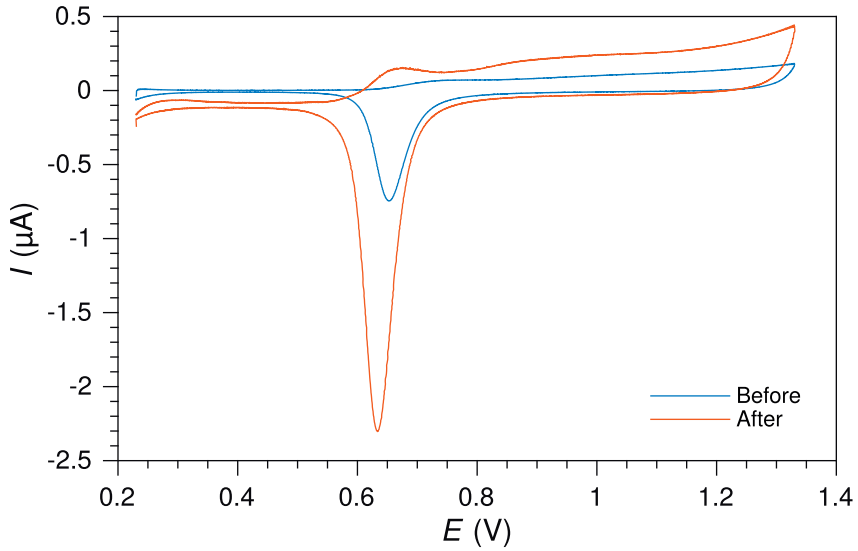

Figure 8.17: Aftermath of addition of Pd^{2+} to the electrolyte. Cyclic voltammetry of the palladized Pd electrode in 0.1 M $HClO_4$ before and after potential cycling and stepping experiments in 0.1 mM Pd^{2+}. The apparent surface area increased threefold. The cathodic current in the double layer region is due to increased oxygen content in the electrolyte at the end of the experiment.

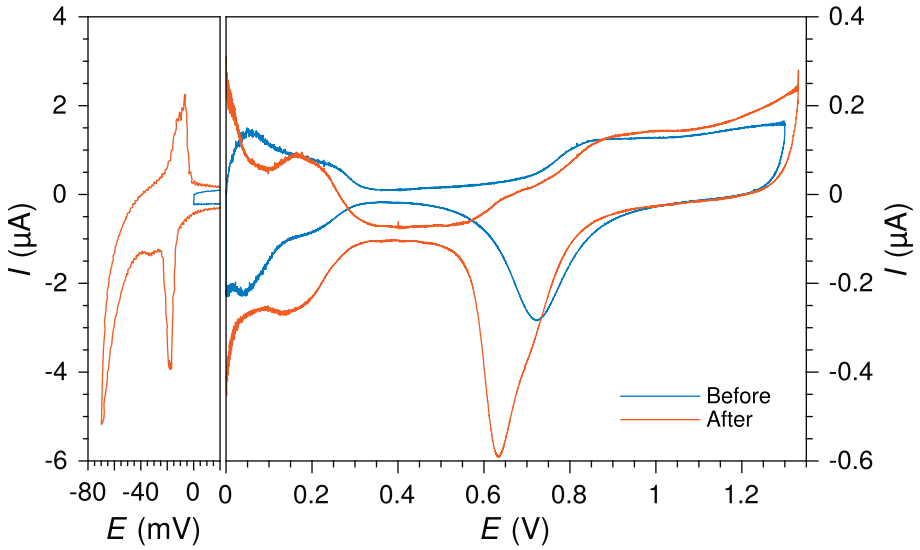

Figure 8.18: Aftermath of addition of Pd^{2+} to the electrolyte. Cyclic voltammetry of palladized Pt electrode in 0.1 M $HClO_4$ before and after potential cycling and stepping experiments in 0.1 mM Pd^{2+}. The increased cathodic current in the double layer region is due to increased oxygen content in the electrolyte at the end of the experiment.

8.8 Potential stepping

Potential stepping is here investigated as an alternative to cyclic voltammetry for measurement of formaldehyde and formic acid. The advantage of stepping is that it may be done faster, and with simpler data analysis than cyclic voltammetry, as the measurement is performed at a constant potential. One downside is that identification of the processes is more difficult, as we don't see the full picture in the same way as in voltammograms. For the detection of formic acid and formaldehyde, the electrode is stepped between the active region, where the organic molecules are oxidized, and the oxide region, where the electrode is reactivated by stripping off adsorbed CO and generating Pd^{2+}.

The experiments in this section were performed in sequences of at least 50 potential steps between 1.43 or 1.33 V and 0.55, 0.44 or 0.33 V, and the measurements were typically stable after 5-10 steps. Cyclic voltammetry at 500 mV/s was performed between each stepping sequence to indicate the condition of the electrode, and as a means of normalizing the electrode between measurements.

It should be noted that potential stepping, especially to higher oxidation potentials, can be damaging to the palladium electrode and decrease the lifetime of the cell. The dissolution of the electrode also keeps the electrode activity high, so in this case it is a necessary evil. One cell was used for about 20 stepping sequences of more than 50 steps each without noticeable damage.

8.8.1 Formic acid

Figure 8.19 shows a section from the potential stepping in 10 mM formic acid. During the oxide step, the current practically drops to zero, as expected for formic acid on palladium oxide. As the potential is stepped down and the palladium oxide is reduced, there is an almost immediate anodic current from formic acid oxidation. The detection current is highest for 0.44 V, and very similar for the 0.55 V and 0.33 V sequences. Pd is still active towards formic acid at lower potentials. The drop-off in the current during the 1 second step is around 10 %.

Figure 8.20 shows an example of the cyclic voltammograms from between the stepping sequences. A secondary effect from the stepping sequences is that is seems to activate the palladium electrode. The peak currents measured after and between the potential stepping were all similar, and higher than in the voltammograms before the stepping. The electrode is also active on the initial forward sweep (after some time at open circuit), and the forward and reverse peak currents are roughly equal at this scan rate. The peak currents and the stepping detection currents are similar, but are slightly below the calculated mass transport limited current of 10 mM formic acid at this flow rate and electrode width from equation 4.17, (24 µA).

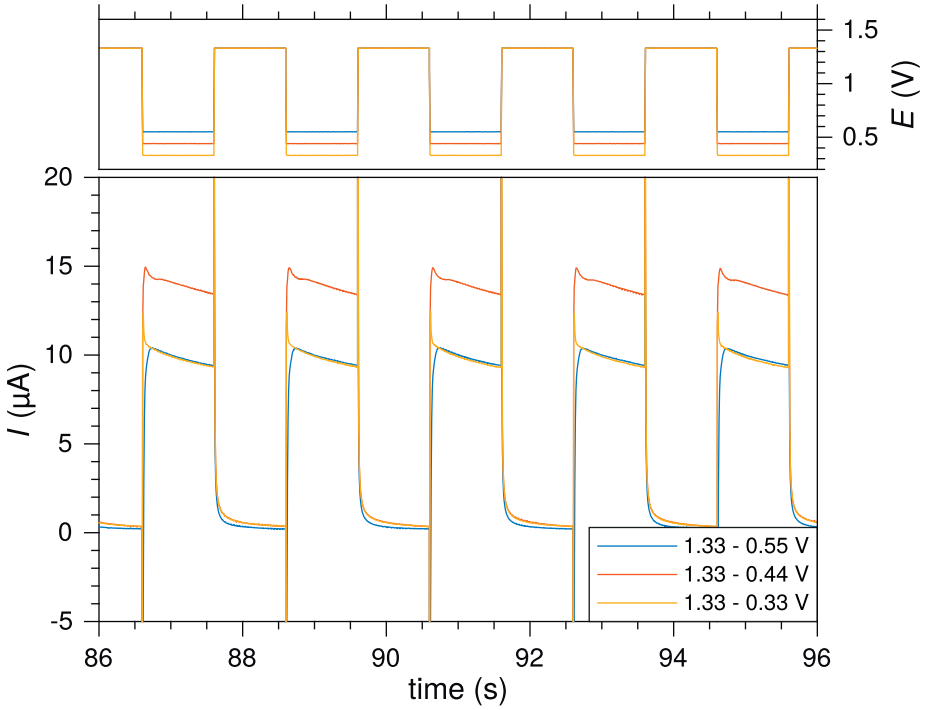

Figure 8.19: Potential stepping on the palladium electrode in 10 mM formic acid at 5 µL/min. Effect of changing the detection potential.

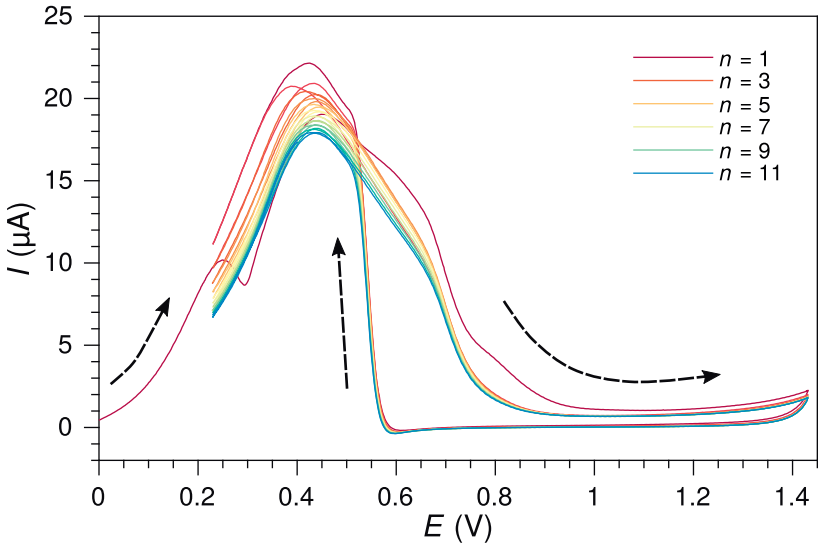

Figure 8.20: Cyclic voltammetry at 500 mV/s in 10 mM formic acid at 5 µL/min, between stepping experiments. Highest peak currents are for the first cycles.

8.8.2 Formaldehyde

Figure 8.21 shows the current response from stepping the Pd electrode in a 10 mM solution of formaldehyde. There is a definite oxidation current for all cases, though it is reduced for the lower detection potentials. Detection currents are at about 0.3 µA for the first sequence, and 0.1 µA for the later two. The first thing to note is that the stepping sequences had an extreme effect on activating the electrode, with the currents in cyclic voltammogram after the first set of stepping sequences increasing by an order of magnitude (not shown). Potential stepping may be a better method of activating the Pd electrode towards formaldehyde oxidation than cyclic voltammetry.

The oxidation current is much higher when stepping to 0.55 V, which is consistent with the low activity of formaldehyde at lower potentials in cyclic voltammetry. After the step down to the active potential, the current quickly peaks at 3.2 µA, before rapidly decreasing down to 1.2 µA over the 1 second step. The current at 0.44 V is only slightly higher than the current at 0.33 V; both are below 0.2 µA.

The typical cyclic voltammogram from between the stepping sequences is shown in figure 8.22. As mentioned above, the potential stepping had a big impact on the activity of the electrode. The initial scan, starting at open circuit (about 0.25 V), indicates that the electrode was initially blocked by CO, as the current remains zero until the stripping peak at 0.9 V. The following reverse scan is also the most active, and the voltammogram then stabilizes towards lower activity after 11 cycles.

8.8.3 Formic acid + formaldehyde

In a 10 mM mixture of both formic acid and formaldehyde, the stepping techniques in figure 8.23 show similar initial detection currents as in 10 mM formic acid, and the main effect of formaldehyde addition seems to be faster deactivation of the Pd electrode. At low potentials, where as previously mentioned the detection current from formaldehyde is low, there is still a very significant contribution from formaldehyde in the deactivation of the electrode. The cyclic voltammogram in figure 8.24 also shows this, with the forward peaks being half the reverse scans even at the high scan rate. The initial forward sweep also shows that the surface is partially blocked by CO, as the peak current at 0.5 V in the forward scan is low, and there is a peak at 0.85 V corresponding to CO-oxidation.

Potential stepping to lower potentials than the active potential region of formaldehyde should allow for oxidation of formic acid to take place on palladium with limited faradaic contribution from any formaldehyde in the solution.

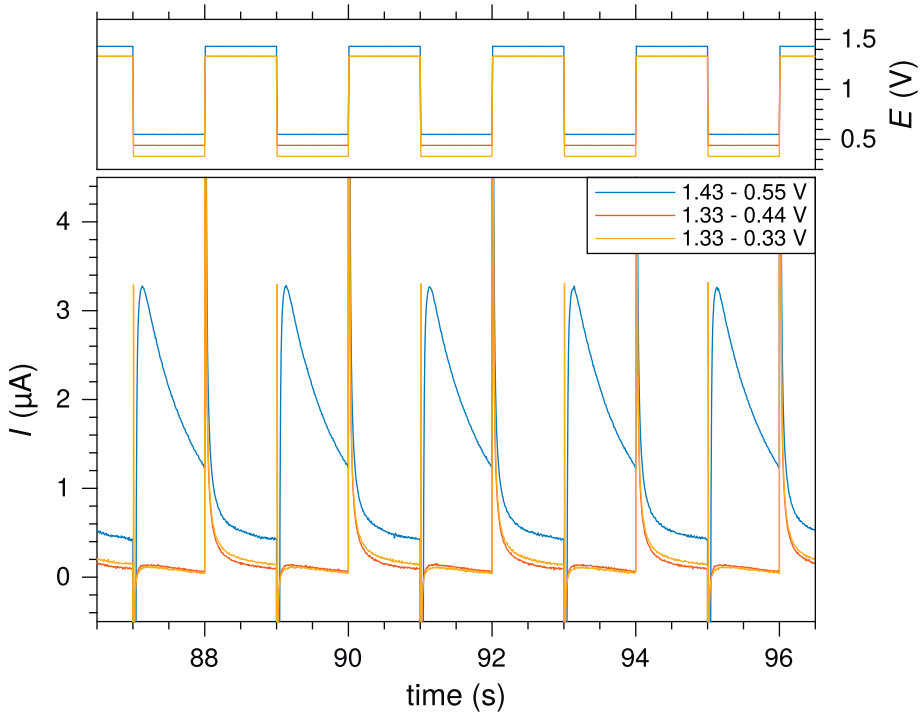

Figure 8.21: Potential stepping in 10 mM formaldehyde at 5 µL/min. Effect of changing the upper potential.

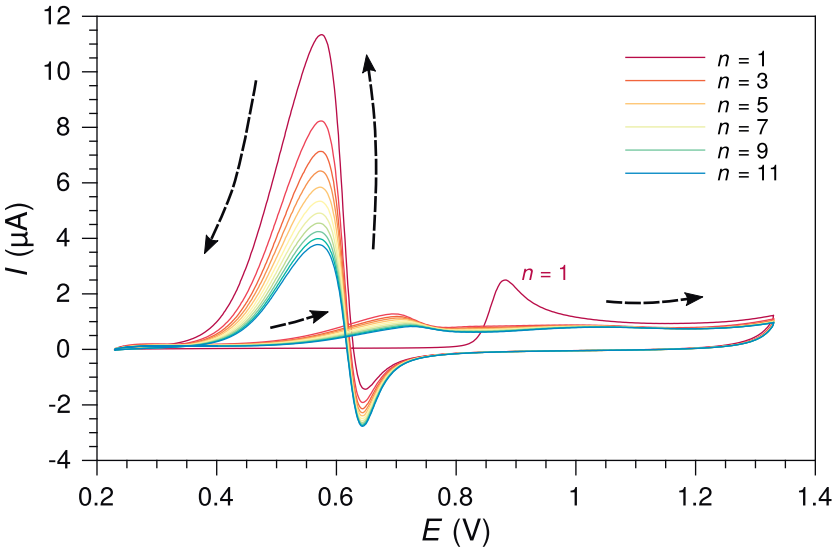

Figure 8.22: Voltammograms from 10 mM formaldehyde at flow rate 5 µL/min and scan rate 500 mV/s, run between the stepping sequences. The first cycle is the most active, then the peak current decreases for the subsequent cycles.

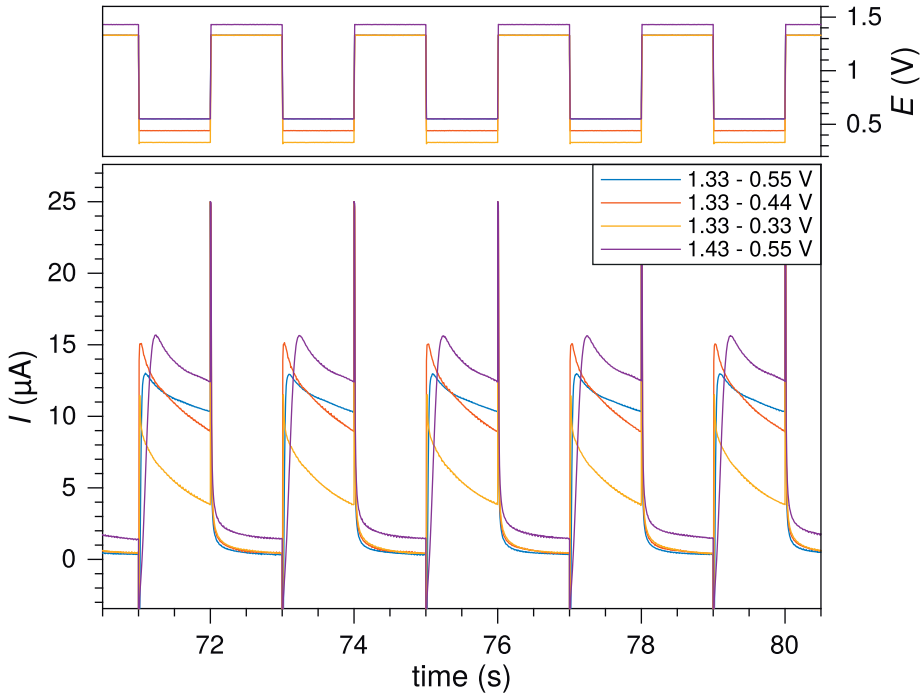

Figure 8.23: Potential stepping in a 10 mM solution of both formic acid and formaldehyde at 5 µL/min. Effect of changing the detection potential.

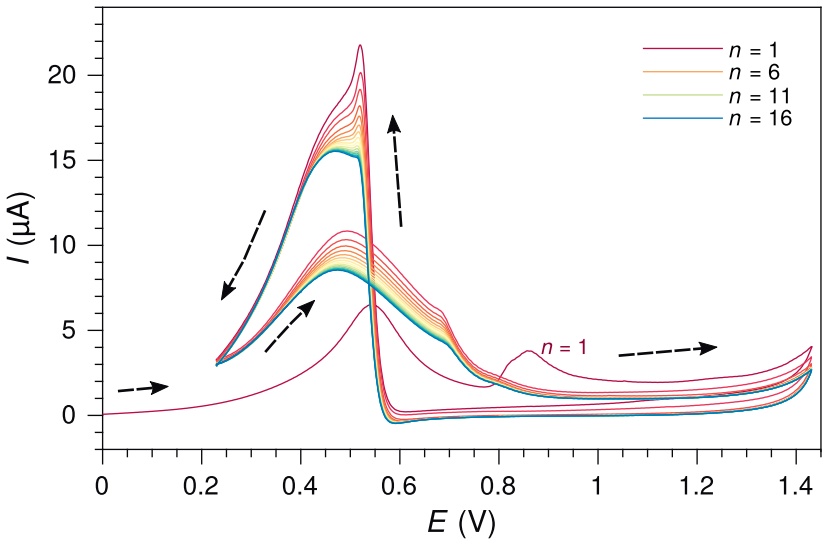

Figure 8.24: Cyclic voltammetry at 500 mV/s in 10 mM formic acid and 10 mM formaldehyde at 5 µL/min, recorded between stepping experiments. Highest peak currents are for the first cycles.

8.9 Conclusion

The palladium electrode is a good candidate for sensing methanol oxidation products because it is active towards formic acid and formaldehyde oxidation at low concentrations, while remaining inactive towards higher concentrations of methanol in the same analyte. However, the oxidation of formic acid and formaldehyde are catalytic reactions as well, and knowledge of these oxidation processes is required to use the Pd electrode as a sensor.

Palladium was found to be relatively quickly deactivated in low concentrations of formic acid, in solutions both with and without additional methanol. The measurements in formic acid showed that the variation in the activity, even in clean solutions with no other organics, is probably too great for quantitative measurements of formic acid content at anything but mass transport limited (i.e. high activity) conditions. At constant potential only a fraction of the available formic acid is oxidized, at least in convective systems. The measurements here agree with the literature on the effect of having palladium(II) ions in solution. Whether added as palladium salts or generated from dissolution of the electrode itself, it was found to be essential in keeping the activity of the electrode high by removing an adsorbed species from the surface. Mass transport limited currents in 1 mM formic acid was found after addition of 0.1 mM Pd^{2+} to the electrolyte, and close to transport limited currents was found by aggressive potential step techniques.

Treatment of the sense electrode with palladium(II) is proposed as a method of boosting the activity of the Pd sense electrode, though this requires protection of the working electrode to avoid modifying that as well.

Formaldehyde was found to be less active on palladium than formic acid, and with a different mechanism leading to at least partial blocking of the electrode surface by CO, which requires potentials above 0.8 V to remove. The activity of formaldehyde at lower potentials is low, and in cyclic voltammetry the electrode is only active directly after reduction of the surface oxide. Whether it is possible to actually quantify formaldehyde in solution is uncertain, especially in addition to more active species like formic acid.

Measurements of formic acid alone, without any significant current from formaldehyde oxidation, could be possible by measurement at lower potentials than the activity region of formaldehyde. Any formaldehyde in the solution would participate in the deactivation of the electrode.

Chapter 9
In situ detection of methanol oxidation products

Abstract

Potential stepping and cyclic voltammetry techniques are utilized for in situ electrochemical detection of formic acid and formaldehyde released from the oxidation of methanol on a smooth Pt electrode. Fast voltammetry is necessary in order to keep the activity of the Pd sense electrode high, which is done here by cyclic voltammetry or potential stepping. The response in the sense current is clearly correlated with the oxidation current at the upstream Pt working electrode. By stepping to lower potentials the response from formaldehyde becomes negligible while the activity of formic acid remains high. The comparisons between the oxidation currents at the Pt working and Pd sense electrodes show that a significant fraction of the methanol oxidized at the smooth Pt electrode is released downstream as formic acid. It also shows that this fraction is different for different regions of the CH_3OH voltammogram.

9.1 Introduction

As was seen in chapter 8, formic acid and formaldehyde oxidation lead to deactivation of the palladium electrode within seconds, even without the presence of higher concentrations of methanol. Continuous measurement of the oxidation products from methanol at a constant potential is thus not feasible as the measurement current will be low, and the effects from changing concentrations and deactivation of the electrode cannot be separated.

It is therefore necessary to constantly reactivate the electrode in order to reliably measure oxidation currents from electroactive oxidation products. This can be done either by cycling the Pd electrode at a relatively fast rate, or by stepping the potential between the oxide region and an electroactive potential.

The obvious limitation by measuring concentration with potentiodynamic techniques is that the time resolution of the measurement is dependent on the speed of the technique applied to the sense electrode. The techniques must be fast, both to increase the resolution of the measurements, and to increase the activity of the electrode. However this also increases the current contributions from surface processes, which contribute to significant background signals in low concentrations of the target species.

The potential stepping in model electrolytes with known concentrations of formic acid and formaldehyde in chapter 8, showed that a measurement of only the formic acid is possible by stepping directly to lower potentials such as 0.33 mV.

In this chapter, potential cycling and stepping techniques on a downstream palladium microband electrode are applied to measure the release of soluble intermediates during methanol oxidation on the smooth platinum electrode located upstream.

9.2 Experimental

The fabrication of microfluidic cells and the general electrochemical setup is described in chapter 2. All measurements in this chapter were performed with 100 µm electrodes, with 100 µm electrode gaps. The electrodes are a Pd electrode (SE) downstream of a Pt (WE) electrode, with a Pt counter electrode downstream of both. Figure 9.1 shows a schematic with the physical dimensions of the microfluidic cell used in these experiments.

In situ detection of methanol oxidation products were performed in a 2 M CH_3OH solution, with 0.1 M $HClO_4$ as the base electrolyte. The flow rate was 5 µL/min for all experiments in this chapter. All potentials were measured vs. a palladium hydride reference electrode, which was charged with hydrogen at a constant current of –5 µA in the base electrolyte at a flow rate of 20 µL/min, and then left to relax for at least 30 minutes before measurements, as described in detail previously. The channel branch with the reference electrode was kept stagnant during the measurements.

Bipotentiostat measurements were done in the *CE to ground* mode of the Biologic VMP3 potentiostat, with common reference and counter electrodes. Both the Pt and Pd electrodes were simultaneously conditioned by cycling at 500 mV/s immediately before measurements to activate the electrodes and ensure a reasonably reproducable starting point.

The Pt working electrode was cycled at 20 mV/s, while the downstream Pd sense electrode was either cycled at 500 mV/s between 0.33 and 1.33 V, or stepped between 1.33 V and 0.33 or 0.55 V, with step lengths of 0.5, 1 or 2 s. Due to the fast deactivation of the sense electrode and the potentiodynamic nature of the measurements, only one data point is presented from each cycle or potential step. For the CV sense measurements this was found by taking the

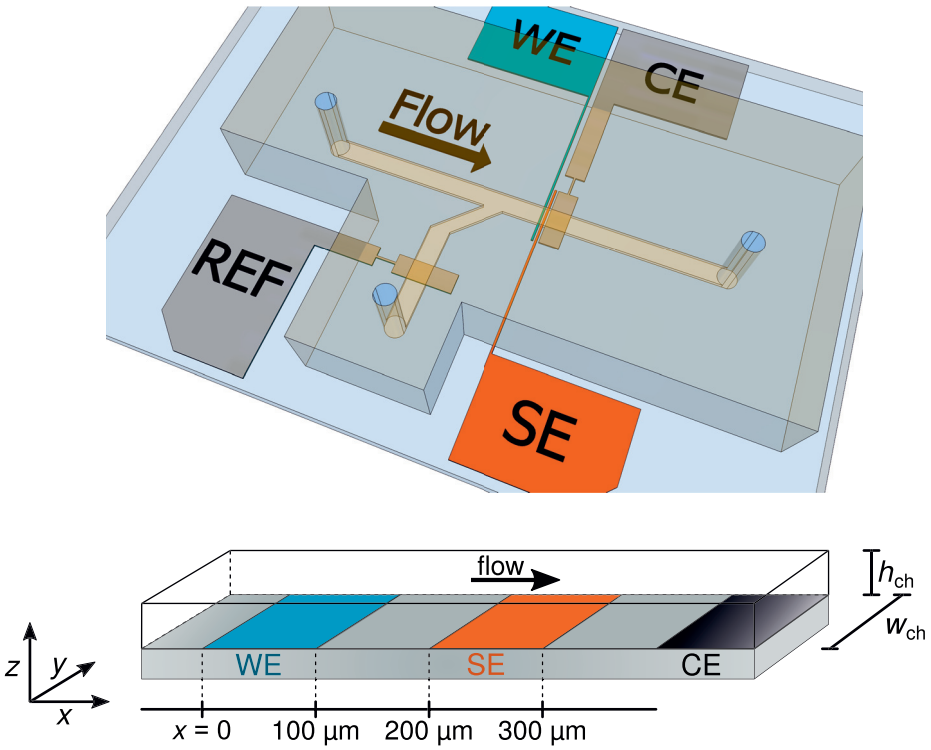

Figure 9.1: Schematic of the microfluidic cell used in the measurements. WE is a 100 µm Pt electrode, and SE is a 100 µm Pd electrode. The electrode gap is also 100 µm. The channel dimensions are $h_{ch} = 55\,\mu m$ and $w_{ch} = 1\,mm$.

mean current in an area following the reverse scan anodic peak from 0.52 to 0.50 mV, where the activity is highest, as shown in figure 9.2. For the potential stepping techniques the mean current was taken from 0.1 to 0.9 s of the lower potential step, or 0.1 to 0.5 s for the 0.5 s steps.

The sense current data points were correlated with the voltammetry performed simultaneously at the WE, using the time at the middle of the averaged region. The slight mass transit lag from the working electrode to the sense electrode was not corrected for. For comparison, average transit time from the working to the sense electrode for the $Ru(bpy)_3^{2+}$species at this flow rate and geometry, was around 200 ms (see section 4.3.4), which corresponds to a 4 mV lag from the WE potential here.

It should be noted that, following on the investigation of the potential distribution in the microchannel in chapter 6, the solution potential over the sense electrode will be shifted as a function of the current on the working electrode. For an anodic current at 7 µA at the working electrode in this electrolyte, the measured potential at the sense electrode will shift by approximately $-10\,mV$.

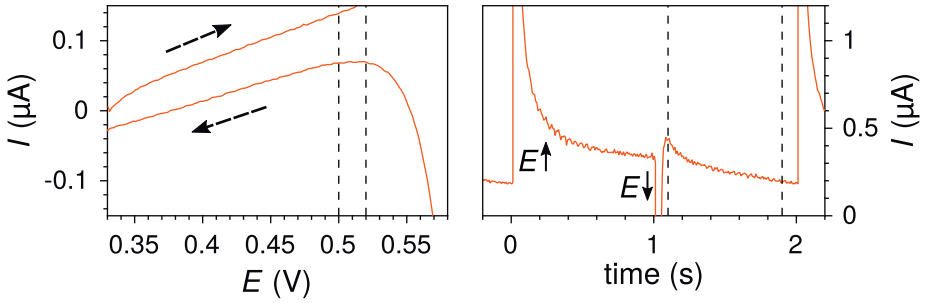

(a) Cyclic voltammetry. **(b)** Potential step.

Figure 9.2: Data sampling from the two in situ detection methods. The current was averaged between the dotted lines, (a) on the reverse scan peak and (b) from 0.1 to 0.9 s into the step to lower potentials.

9.3 Methanol oxidation

Figure 9.3 shows the typical voltammogram on the platinum working electrode during the bipotentiostat experiments below. The concentration was increased to 2 M methanol to maximize the oxidation current, and thus the detection signal.

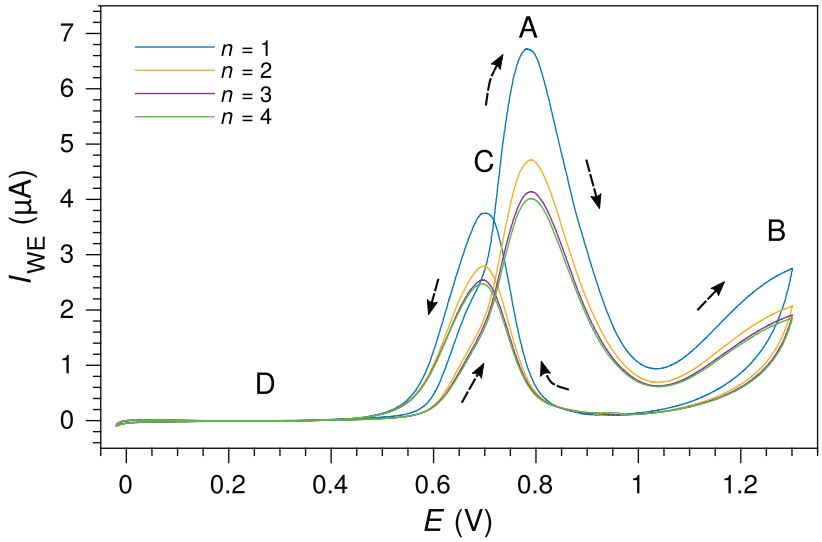

Figure 9.3: Cyclic voltammogram at 20 mV/s on Pt in 2 M methanol. The electrode is cycled at 500 mV/s prior to measurement, and the oxidation current is higher at the initial cycles. The following features are defined in the figure: A - forward scan peak, B - upper vertex, C - reverse scan peak, D - region with negligible oxidation current.

Starting at the lower vertex potential of –0.02 V, the current is negligible in the forward scan until the potential is around 0.55 V (region D), due to complete CO(ads) blocking of the active Pt sites [145]. The anodic current then increases towards the forward scan peak at 0.80 V (point A). Due to the formation of less active platinum oxide, the current then drops, however some methanol is still oxidized on the oxide covered electrode, and the current increases again after 1.05 V, approaching the upper vertex potential at 1.30 V (point B). On the reverse scan, the current is low until the onset of platinum oxide reduction at around 0.90 V, where Pt sites again become available for the methanol adsorption and dehydrogenation. The anodic current then increases until the reverse scan peak at 0.70 V, once again due to CO(ads) blocking the active sites. Below 0.45 V the oxidation current is negligible. Before the cycling at 20 mV/s the platinum electrode was cycled at a higher scanrate, so the electrode oxidation currents were higher during the first cycle in figure 9.3. After 4 cycles the peak currents change by only a few percent.

The oxidation of surface adsorbed CO to CO_2 (or CH_3OH to HCOOH) requires an oxygen donor, so water adsorption is important for the activity at potentials below the platinum oxide region [11].

9.4 CV sense

For the detection by cyclic voltammetry, the Pd SE was cycled at a relatively high rate, 500 mV/s, between 0.33 and 1.33 V. With 4 seconds per cycle on the SE, we get one cycle of the SE per 80 mV of the WE voltammogram, and there are 33 points of measurement for each WE cycle. At low concentrations of formic acid and formaldehyde, the cyclic voltammogram of Pd is very close the CV obtained in blank electrolyte, and the dominating features are formation and reduction of palladium oxide. The most interesting region for sensing of electroactive species is directly after the oxide reduction peak in the reverse scan.

Figure 9.4 shows a comparison of voltammograms with the highest and lowest reverse scan peak currents at the SE during one WE cycle. At most, there is a small positive peak, though this feature is not simple to find for all cycles. A numerical value for the sense current, I'_{SE}, was found by taking the mean current of the region around the reverse scan peak, from 500 to 520 mV (dotted region in figure 9.4) for all the cycles.

In figure 9.5, the detection current is plotted together with the methanol voltammogram recorded simultaneously in the 1st cycle at the WE. The current axes have been manually scaled to compare the currents. The detection current at the downstream Pd sense electrode clearly corresponds well to the oxidation current on the working electrode, though the low resolution makes the features less defined, as e.g. the reverse scan peak is covered by only two data points. There is a general trend, which was also seen for the subsequent cycles, that

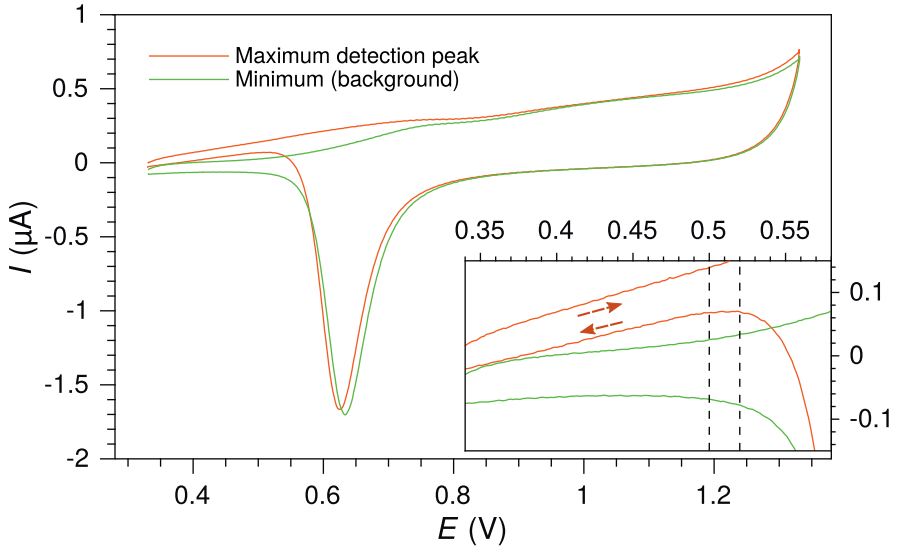

Figure 9.4: Sensing of MeOH oxidation products by cyclic voltammetry at 500 mV/s on Pd downstream of the Pt electrode. Maximum and minimum detection current. The insert shows a closer view of the reverse scan peak area. Dotted lines indicate the region used to output a value for the sense current in this cycle.

the sense current is comparatively lower during the reverse scan peak than the forward scan peak. On the oxidized Pt electrode over 1 V, the current is comparatively higher.

Over the course of several cycles there was also an effect of increased *background* current, i.e. the sense current when the working electrode is in the low current region. The sense current is plotted as a function of time and compared with stepping techniques in section 9.6.

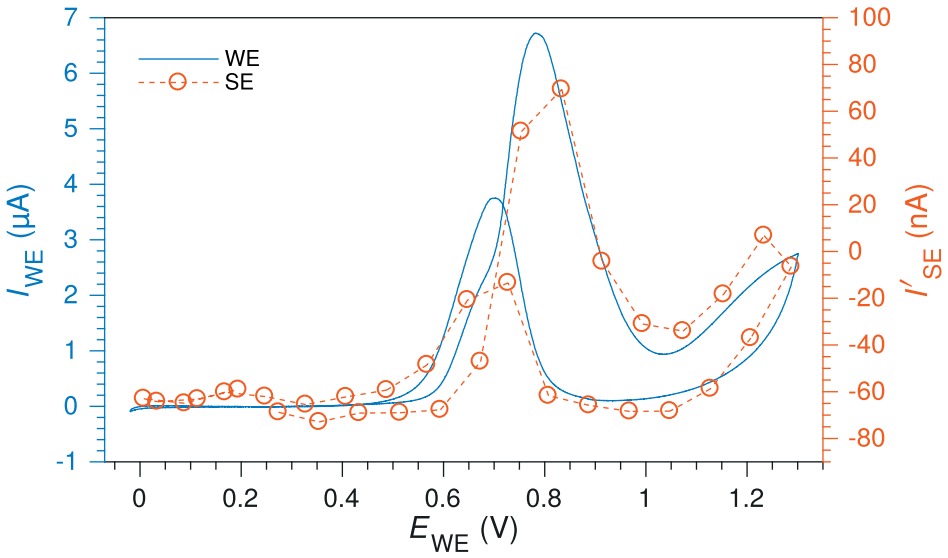

Figure 9.5: Collection voltammogram from sensing by cyclic voltammetry at the Pd sense electrode. 1st WE cycle.

9.5 Stepping sense

To increase the time resolution, and possibly improve the sensitivity of the sensing electrode, a potential step sequence was used here instead of cyclic voltammetry. As discussed on the previous chapter, the sense current found by this method was found to be reproducible in analytes with known concentrations of formic acid and formaldehyde, and to measure close to mass transport limited currents for formic acid oxidation. Several different parameters of the stepping sequences were tested, from 0.5 to 2 second steps, and lower potentials of 0.55 or 0.33 V. The WE was cycled at 20 mV/s, as above. The time resolution for 2 second steps is thus the same as for the cycling sequence above, and 1 second and 0.5 second steps have better resolution.

Figure 9.6 shows the current transients on the SE during the different stepping sequences, comparing the highest response, when the WE is at the forward scan peak (A), with the background response, when the WE is in the region with negligible oxidation current (D). Figure 9.6a was measured during the first cycle on the WE, when the methanol oxidation current is highest, and figure 9.6b was measured during the 4th cycle, when the WE voltammogram is more stable, but also with an increased background signal from absorbed species.

Steps from the oxide region to lower potentials initially give a large negative current from the reduction of palladium oxide, before the oxidation of methanol oxidation products (positive current) becomes dominant. Shorter

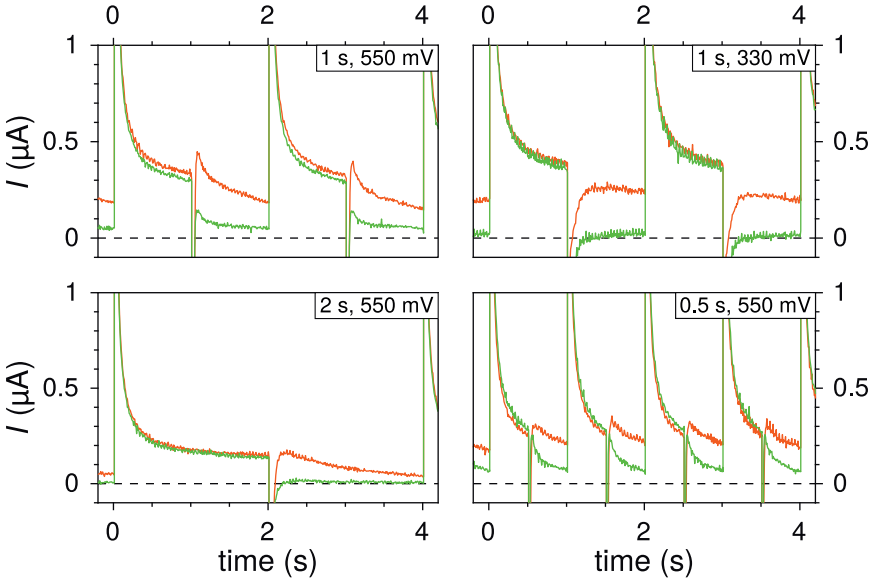

(a) 1st WE cvcle

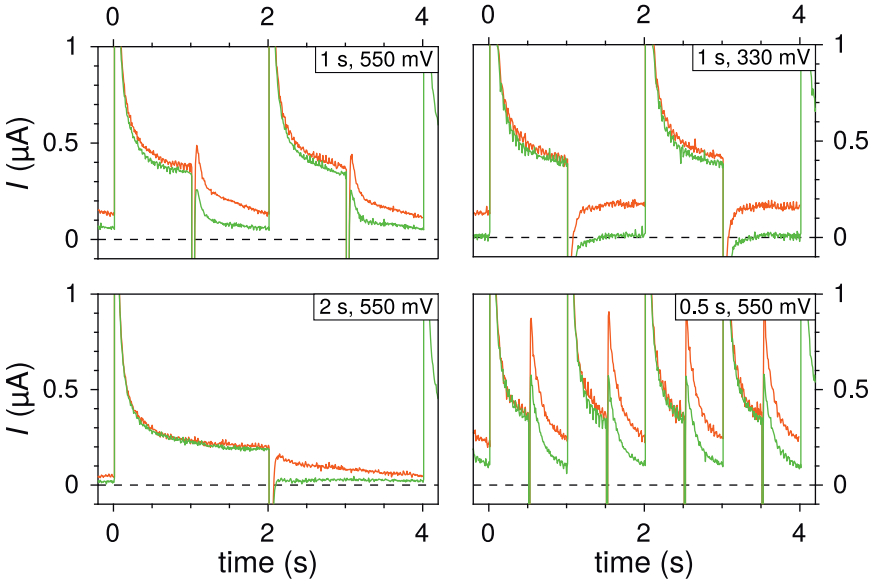

(b) 4th WE cycle

Figure 9.6: Current response from the stepping sequences on the Pd SE. Comparison of the highest detection current (red) and the background detection current (green). The highest sense current is measured during the forward scan peak on the WE (point A in figure 9.3). The background sense current is measured when the WE is not oxidizing methanol, close to the lower vertex (point D in figure 9.3). The step at 0 s is the step up to 1.33 V.

steps and 0.55 V detection potential gives shorter time before the positive peak, and much higher initial peaks before the current drops down. The 2 s steps, or the steps to 0.33 V have much flatter current transients.

Comparing the 1 and 0.5 s steps for the first and fourth WE cycle shows that the initial peaks grow towards the end of the sequence. This is especially prominent in the parts of the sequence when the WE is in the region with negligible oxidation current, and not actively oxidizing methanol. At the end of the 4th WE cycle, the 0.5 s stepping measures an initial peak at over 0.5 µA, even though the methanol oxidation current is negligible at this point. The difference between the current transients for the 0.5 s stepping between figures 9.6a and 9.6b is substantial. This background current comes from accumulation of electroactive species, probably due to absorption and consequent release of methanol from the PDMS, the species are then released back into the electrolyte. The 0.33 V stepping sequence measures very little increase in the background current, as does the 2 s stepping sequence. The likely explanation of this is that formaldehyde is more represented in the background sense current by absorbing and accumulating to a higher degree than formic acid, especially as the stepping to 0.33 V show no increase in the background current. As discussed in the previous chapter, stepping to low potentials leads to negligible formaldehyde oxidation currents on the Pd electrode. No literature data was found on the absorption of formaldehyde and formic acid in PDMS from aqueous electrolytes. The experiments in solutions with known concentrations of these species in chapter 8 showed at least qualitatively that both species do contaminate the PDMS, at least at higher concentrations.

The detection current measured on the SE was correlated to the voltammetry performed on the WE using the time at the middle of the measured region, and is plotted with the WE cyclic voltammogram in figures 9.7 and 9.8. The detection current follows the methanol oxidation current closely, though it is clear that less electroactive products are detected on the reverse methanol oxidation peak than on the forward scan peak, and that even more electroactive products are formed at higher potential, i.e. at the Pt oxide electrode.

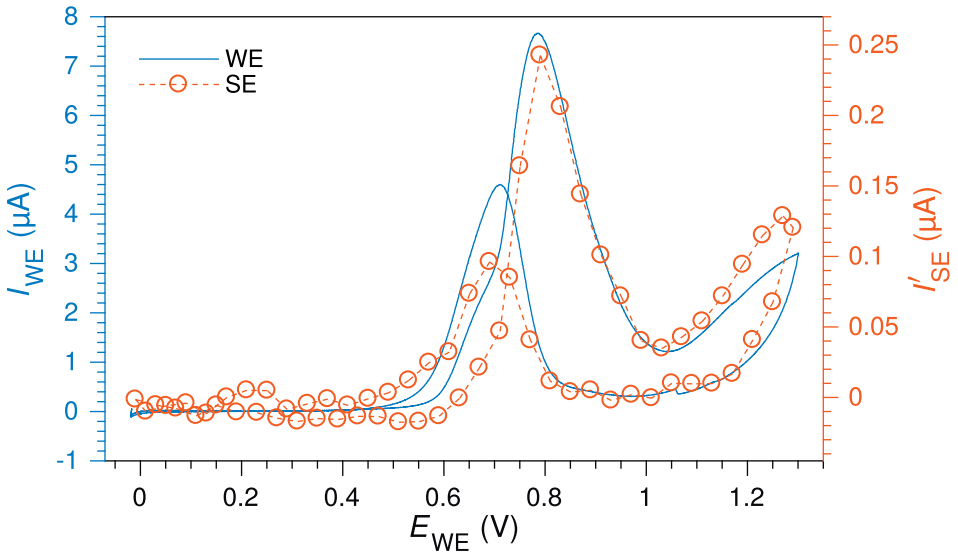

Figure 9.7: Collection voltammogram from the 0.33 V stepping sequence. First cycle.

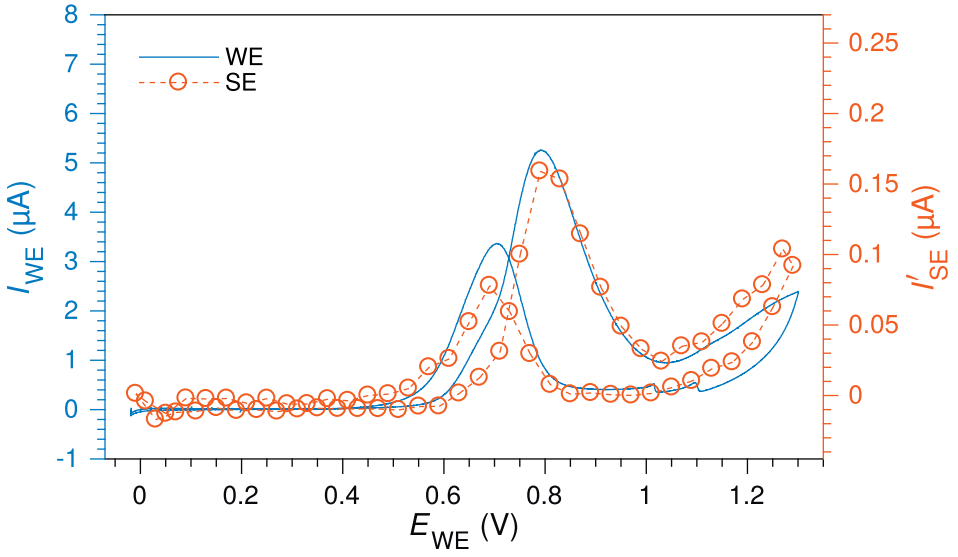

Figure 9.8: Collection voltammogram from the 0.33 V stepping sequence. Fourth cycle.

9.6 Background current

Figure 9.9 shows a comparison of the detection currents measured from the different stepping and cycling methods, and how the measurements evolve in time. The background current is pretty clear from this comparison, increasing quickly for the 0.5 s stepping sequence, with the magnitude of the background currents at the end of the sequence similar in magnitude to the peaks. The background sense current is increasing more slowly for the other cases, and barely increasing for the 0.33 V stepping sequence.

The peak magnitudes, compared to the local background levels, are similar for the 0.5 s and the 0.33 V sequences, slightly lower for the 0.55 V,1 s sequence, and lower for the 2 s and CV sequences.

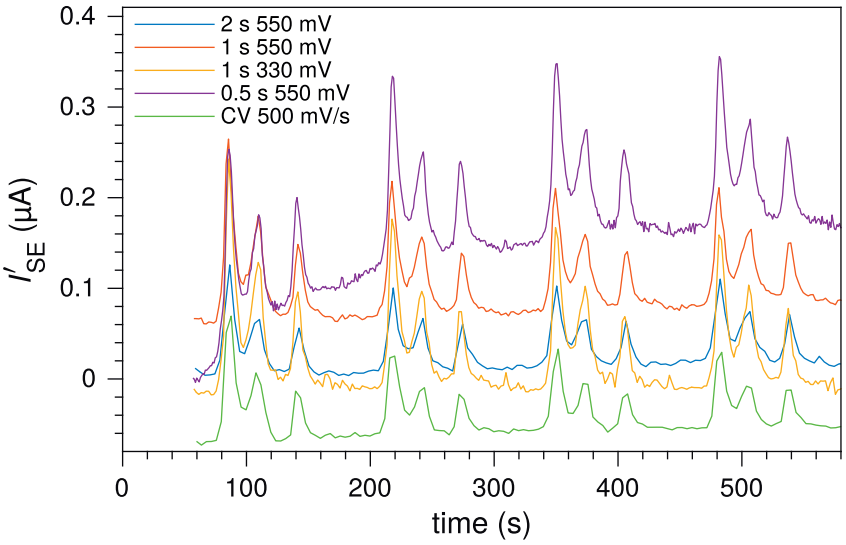

Figure 9.9: Comparison of the averaged detection current for the different stepping sequences. Detection currents are similar, though the increase in background currents are different, especially for the 0.5 s stepping sequence, which was run after recharging and flushing with clean electrolyte. The 0.33 V sequence was actually run directly after the 0.5 s one, and measures barely any background current.

9.7 Cyclic voltammetry of CH_3OH oxidation products

Figure 9.10 shows an attempt to characterize the product species by slower cyclic voltammetry on Pd while keeping the WE at constant potential. Both electrodes were cycled at 500 mV/s as shown in the top plot. The WE potential was held at 815 mV after the last forward scan to make the current as high as

possible, though it drops significantly during the SE cycle. The WE was left at open circuit after the first SE cycle.

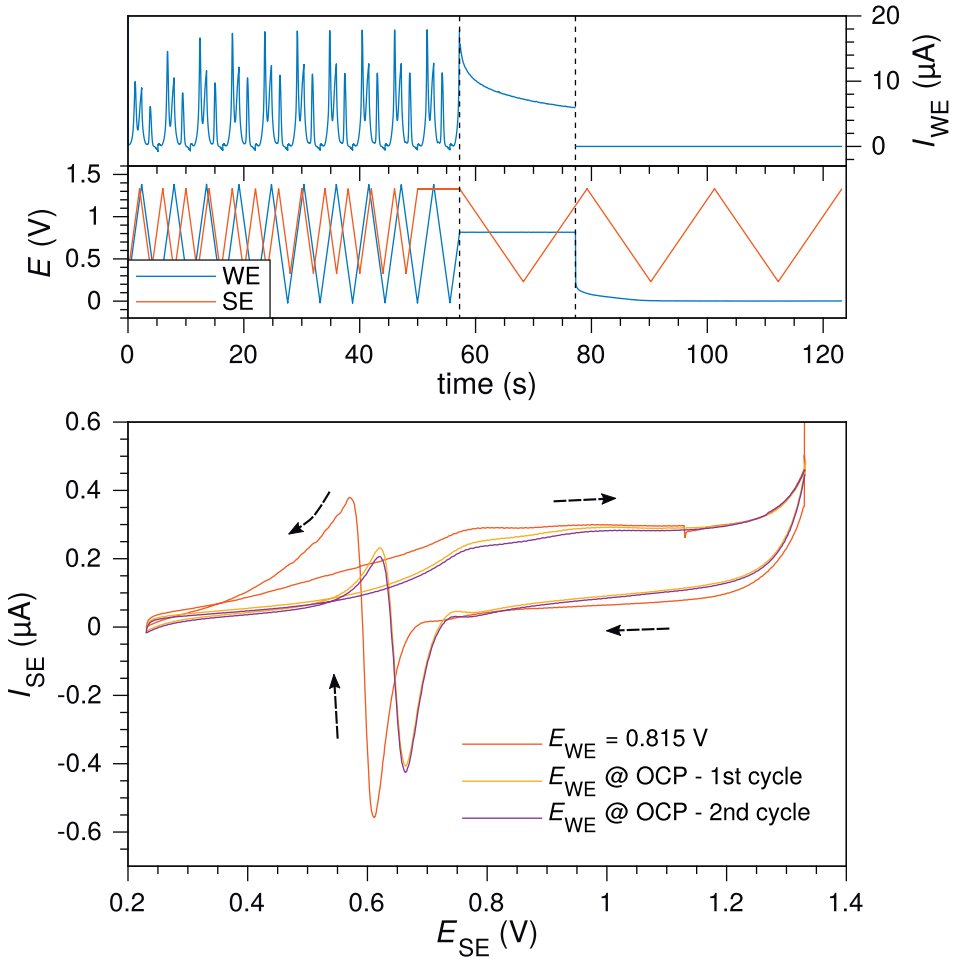

Figure 9.10: Characterization of the methanol oxidation products using cyclic voltammetry at 20 mV/s at Pd SE with the Pt WE at constant potential. Both electrodes were cycled at 500 mV/s before measuring (see E vs t above). WE is kept at constant potential for the first SE cycle(region marked by dotted lines in the top plot), then left at open circuit for the subsequent cycles.

9.8 Concluding discussion

The electrochemical measurement of methanol oxidation products is made difficult by the deactivation of the Pd electrode, even in methanol-free solutions with low concentrations of formic acid. The cyclic voltammetry and potential stepping sequences presented here were designed to overcome these challenges

and provide quantitative information of formic acid and formaldehyde released from the Pt electrode during methanol oxidation.

The potential stepping and CV sense sequences in this chapter show the way towards in situ quantitative sensing, at least for formic acid. As was previously seen, stepping from the oxide region down to 0.33 V gives a negligible faradaic response from formaldehyde, while oxidizing formic acid at rates approaching the mass transport limited current. The measurements on the downstream sense electrode closely match the oxidation current on the working electrode, with the same features as the methanol cyclic voltammogram. One interesting feature is that the fraction of the methanol oxidation current leading to release of formic acid downstream, is not constant during the voltammogram. A larger fraction of formic acid is released during the forward scan peak than the reverse, and an even larger fraction is sensed in the oxide region close to the upper vertex potential. The fraction of the methanol oxidized at the smooth platinum electrode which is released downstream as formic acid is substantial.

Due to the slow oxidation of methanol on the smooth platinum electrode, the amount of detectable product species is comparable to submillimolar concentrations at best, even in solutions of 2 M methanol. Some further experimental work involving the potential stepping on Pd in lower concentrations of formic acid and formaldehyde, as well as boosting the sensitivity of the sense electrode by electrodeposition of more palladium, is recommended to complement these measurements and increase the knowledge on using palladium as a sense electrode. The exact effect of methanol on the Pd electrode is also not completely known, and while there is a negligible faradaic effect unless the electrode is cycled to potentials above 1.3 V, it may still affect the activity and deactivation of the sense electrode towards the other species.

Many of the attempted sequences show a significant increase in the background levels of the sense signal. While the effect could be explained by absorption of especially formaldehyde into the channel slab, the interaction between the PDMS and the organic species is not completely clear. This application of microfluidic cells would greatly benefit from a move to more electrochemically compatible materials for the cell.

The technique used here can be used to investigate the effect of different parameters on the methanol oxidation reaction mechanism. The methanol concentration, supporting electrolyte and mass transport are parameters which are in immediate reach. Modification of the platinum by either electrochemical deposition of other noble metals such as ruthenium, or experiments on supported catalyst particles are also possible. It may also be possible to operate the microfluidic cell at elevated temperatures. This technique may also be combined with other methods such as on-line DEMS.

9.9 Conclusion

A method of using the downstream palladium electrode as a sense electrode for the soluble and electroactive products of the methanol oxidation reaction, is presented. Stepping the potential of the palladium electrode between 0.33 and 1.33 V isolates the oxidation of formic acid with negligible contributions from formaldehyde oxidation. The method shows that the fraction of the methanol oxidation reaction on the smooth palladium electrode leading to release of formic acid is substantial.

Chapter 10
Conclusions

The aim of this thesis was to develop the microfluidic flow electrochemical cell to complement conventional large-volume cells, by offering an alternative with improved dynamics. Second, the objective has been to utilize this in investigations of the methanol oxidation reaction.

Microfluidic electrochemical cells have some very interesting properties that can be employed in electrochemical and electrocatalytic research. Fabrication of microfluidic cells by lithographic methods is fast, inexpensive and reliable, and noble metal thin-film microband electrodes of high quality can be made by electron beam evaporation, and cells with multiple electrodes of different materials can be made. Due to the fast prototyping, a microfluidic electrochemical cell design can go from concept to a fully operational cell in less than a week.

The geometry of the microfluidic electrochemical cells can be tailored towards different attractive mass transport processes, such as high collection efficiency and fast mass transit between multiple electrodes. In this work, mass transit times down to 3 ms were demonstrated.

The internal palladium hydride thin-film reference electrode was found to be a much better alternative to more conventional reference electrodes for use in the microfluidic electrochemical cell. The main advantage is in the simplicity in fabrication and operation, and that the reference electrolyte is non-contaminating to the analyte. One disadvantage with the palladium hydride thin-film reference electrode is that the longevity is not as high as some of the alternatives. The longevity of this reference electrode is typically around 5 hours, which is acceptable for many electrochemical experiments, but would prevent continuous experiments on longer time scales. The practical utility of the palladium hydride reference electrode is implied by its use in all the microfluidic electrochemical experiments in this thesis.

One of the challenges with performing electrochemical experiments in microfludic cells, is that the restricted volume leads to a high solution resistance,

causing inaccuracies in the measured potentials when currents are applied between electrodes. By placing the reference electrode upstream of the working electrodes, the potential distribution becomes significantly more manageable.

The methanol oxidation reaction on a smooth platinum electrode was studied by analysis of the soluble and electroactive intermediates released from the electrode, using a palladium electrode located downstream. A potential step technique was demonstrated to measure formic acid at a rate close to the mass transport limited rate, while the current contribution from formaldehyde was negligible. The fraction of the methanol oxidized at the smooth platinum electrode that is released as formic acid is found to be substantial.

10.1 Further work

Microfluidic flow cells were in this thesis demonstrated as a powerful tool for electrochemical measurements, as an alternative to large volume cells with rotating or wall-jet electrodes. Some suggestions for further use of this type of cells in electrochemical experiments are listed here.

- The microfluidic flow electrochemical cell would benefit significantly from a move to more suitable channel materials than PDMS, due to the absorption of gases and organic molecules in the latter. Fluoropolymers may be good candidates for this.

- The microfluidic electrochemical cell with the palladium hydride reference electrode can be useful in many other cases in addition to the methanol oxidation reaction studied in this thesis. Especially where the excellent mass transport properties can enable novel experimental techniques.

- Investigations of soluble intermediates from the methanol oxidation reaction in the microfluidic cell with different parameters, such as methanol concentration, supporting electrolyte cell geometry and flow rate.

- Modification of the electrode materials using electrochemical deposition, supported catalysts or by sputtering of alloys are possible, enabling further study of electrocatalytic reactions such as the methanol oxidation reaction.

- Operating the microfluidic flow electrochemical cell at elevated temperatures should be possible, and would unlock a very important parameter in electrocatalytic investigations. The palladium hydride electrode could work at higher temperatures, though the effect of temperature on the reference potential would need studying, as the hydrogen solubility in the α-phase changes.

- Combination of the microfluidic flow electrochemical cell with other measurement techniques such as DEMS, FTIR, Raman or EQCM could be possible.

Bibliography

[1] E. V. Fanavoll, D. A. Harrington, S. Sunde, G. Singh, and F. Seland. "A microfluidic electrochemical cell with integrated PdH reference electrode for high current experiments." *Electrochimica Acta* 225 (2017), pp. 69–77. DOI: 10.1016/j.electacta.2016.11.147.

[2] S. Chu and A. Majumdar. "Opportunities and challenges for a sustainable energy future." *Nature* 488.7411 (2012), pp. 294–303. DOI: 10.1038/nature11475.

[3] M. Winter and R. J. Brodd. "What Are Batteries, Fuel Cells, and Supercapacitors?" *Chemical Reviews* 104.10 (2004), pp. 4245–4270. DOI: 10.1021/cr020730k.

[4] S. P. S. Badwal, S. S. Giddey, C. Munnings, A. I. Bhatt, and A. F. Hollenkamp. "Emerging electrochemical energy conversion and storage technologies." *Frontiers in Chemistry* 2 (2014), p. 79. DOI: 10.3389/fchem.2014.00079.

[5] J. Kothandaraman, A. Goeppert, M. Czaun, G. A. Olah, and G. K. S. Prakash. "Conversion of CO_2 from Air into Methanol Using a Polyamine and a Homogeneous Ruthenium Catalyst." *Journal of the American Chemical Society* 138.3 (2016), pp. 778–781. DOI: 10.1021/jacs.5b12354.

[6] G. A. Olah, G. K. S. Prakash, and A. Goeppert. "Anthropogenic Chemical Carbon Cycle for a Sustainable Future." *Journal of the American Chemical Society* 133.33 (2011), pp. 12881–12898. DOI: 10.1021/ja202642y.

[7] J. Larminie and A. Dicks. "Direct Methanol Fuel Cells." In: *Fuel Cell Systems Explained*. 2nd ed. John Wiley & Sons, Ltd,., 2003, pp. 141–161. ISBN: 9781118878330. DOI: 10.1002/9781118878330.ch6.

[8] J.-M. Leger, C. Coutanceau, and C. Lamy. "Electrocatalysis for the Direct Alcohol Fuel Cell." In: *Fuel Cell Catalysis, A Surface Science Approach*. Ed. by M. T. M. Koper. John Wiley & Sons, Inc., 2008, pp. 343–373. ISBN: 9780470463772. DOI: 10.1002/9780470463772.ch11.

[9] T. Iwasita. "Electrocatalysis of methanol oxidation." *Electrochimica Acta* 47.22 (2002), pp. 3663–3674. DOI: 10.1016/S0013-4686(02)00336-5.

[10] J. L. Cohen, D. J. Volpe, and H. D. Abruna. "Electrochemical determination of activation energies for methanol oxidation on polycrystalline platinum in acidic and alkaline electrolytes." *Phys. Chem. Chem. Phys.* 9.1 (2007), pp. 49–77. DOI: 10.1039/B612040G.

[11] T. Iwasita, X. H. Xia, H.-D. Liess, and W. Vielstich. "Electrocatalysis of Organic Oxidations: Influence of Water Adsorption on the Rate of Reaction." *The Journal of Physical Chemistry B* 101.38 (1997), pp. 7542–7547. DOI: 10.1021/jp971376a.

[12] T. Iwasita and F. Nart. "Identification of methanol adsorbates on platinum: An in situ FT-IR investigation." *Journal of Electroanalytical Chemistry and Interfacial Electrochemistry* 317.1 (1991), pp. 291–298. DOI: 10.1016/0022-0728(91)85022-H.

[13] W. Lin, J. Wang, and R. F. Savinell. "On-Line FTIR Spectroscopic Investigations of Methanol Oxidation in a Direct Methanol Fuel Cell." *Journal of The Electrochemical Society* 144.6 (1997), pp. 1917–1922. DOI: 10.1149/1.1837721.

[14] S. Wilhelm, T. Iwasita, and W. Vielstich. "COH and CO as adsorbed intermediates during methanol oxidation on platinum." *Journal of Electroanalytical Chemistry and Interfacial Electrochemistry* 238.1 (1987), pp. 383–391. DOI: 10.1016/0022-0728(87)85187-2.

[15] H. Baltruschat. "Differential electrochemical mass spectrometry." *Journal of the American Society for Mass Spectrometry* 15.12 (2004), pp. 1693–1706. DOI: 10.1016/j.jasms.2004.09.011.

[16] T. Iwasita-Vielstich. "Progress in the Study of Methanol Oxidation by In Situ, Ex Situ and On-Line Methods." In: *Advances in Electrochemical Science and Engineering*. Ed. by H. Gerischer and C. W. Tobias. Wiley-VCH Verlag GmbH, 1990, pp. 127–170. ISBN: 9783527616756. DOI: 10.1002/9783527616756.ch3.

[17] V. Bagotzky, Y. Vassiliev, and O. Khazova. "Generalized scheme of chemisorption, electrooxidation and electroreduction of simple organic compounds on platinum group metals." *Journal of Electroanalytical Chemistry and Interfacial Electrochemistry* 81.2 (1977), pp. 229–238. DOI: 10.1016/S0022-0728(77)80019-3.

[18] A. Abd-El-Latif and H. Baltruschat. "Formation of methylformate during methanol oxidation revisited: The mechanism." *Journal of Electroanalytical Chemistry* 662.1 (2011), pp. 204–212. DOI: 10.1016/j.jelechem.2011.06.031.

[19] G. M. Whitesides. "The origins and the future of microfluidics." *Nature* 442.7101 (2006), pp. 368–373. DOI: 10.1038/nature05058.

[20] D. B. Weibel, A. C. Siegel, A. Lee, A. H. George, and G. M. Whitesides. "Pumping fluids in microfluidic systems using the elastic deformation of poly(dimethylsiloxane)." *Lab Chip* 7.12 (2007), pp. 1832–1836. DOI: 10.1039/B714664G.

[21] X. Fu, N. Mavrogiannis, S. Doria, and Z. Gagnon. "Microfluidic pumping, routing and metering by contactless metal-based electro-osmosis." *Lab Chip* 15.17 (2015), pp. 3600–3608. DOI: 10.1039/C5LC00504C.

[22] R. Niu, P. Kreissl, A. T. Brown, G. Rempfer, D. Botin, C. Holm, T. Palberg, and J. de Graaf. "Microfluidic pumping by micromolar salt concentrations." *Soft Matter* 13.7 (2017), pp. 1505–1518. DOI: 10.1039/C6SM02240E.

[23] M. A. Unger, H.-P. Chou, T. Thorsen, A. Scherer, and S. R. Quake. "Monolithic Microfabricated Valves and Pumps by Multilayer Soft Lithography." *Science* 288.5463 (2000), pp. 113–116. DOI: 10.1126/science.288.5463.113.

[24] A. K. Au, H. Lai, B. R. Utela, and A. Folch. "Microvalves and Micropumps for BioMEMS." *Micromachines* 2.2 (2011), pp. 179–220. DOI: 10.3390/mi2020179.

[25] N. Sundararajan, D. Kim, and A. A. Berlin. "Microfluidic operations using deformable polymer membranes fabricated by single layer soft lithography." *Lab Chip* 5.3 (2005), pp. 350–354. DOI: 10.1039/B500792P.

[26] D. Sinton. "Energy: the microfluidic frontier." *Lab on a Chip* 14.17 (2014), pp. 3127–3134. DOI: 10.1039/C4LC00267A.

[27] S. A. M. Shaegh, N.-T. Nguyen, and S. H. Chan. "A review on membraneless laminar flow-based fuel cells." *International Journal of Hydrogen Energy* 36.9 (2011), pp. 5675–5694. DOI: 10.1016/j.ijhydene.2011.01.063.

[28] E. R. Choban, L. J. Markoski, A. Wieckowski, and P. J. Kenis. "Microfluidic fuel cell based on laminar flow." *Journal of Power Sources* 128.1 (2004), pp. 54–60. DOI: 10.1016/j.jpowsour.2003.11.052.

[29] R. S. Jayashree, L. Gancs, E. R. Choban, A. Primak, D. Natarajan, L. J. Markoski, and P. J. A. Kenis. "Air-Breathing Laminar Flow-Based Microfluidic Fuel Cell." *Journal of the American Chemical Society* 127.48 (2005), pp. 16758–16759. DOI: 10.1021/ja054599k.

[30] S. Hashemi, M. Neuenschwander, P. Hadikhani, M. Modestino, and D. Psaltis. "Membrane-less micro fuel cell based on two-phase flow." *Journal of Power Sources* 348 (2017), pp. 212–218. DOI: 10.1016/j.jpowsour.2017.02.079.

[31] E. Kjeang, N. Djilali, and D. Sinton. "Microfluidic fuel cells: A review." *Journal of Power Sources* 186.2 (2009), pp. 353–369. DOI: 10.1016/j.jpowsour.2008.10.011.

[32] E. Kjeang, R. Michel, D. A. Harrington, N. Djilali, and D. Sinton. "A Microfluidic Fuel Cell with Flow-Through Porous Electrodes." *Journal of the American Chemical Society* 130.12 (2008), pp. 4000–4006. DOI: 10.1021/ja078248c.

[33] E. Kjeang, J. McKechnie, D. Sinton, and N. Djilali. "Planar and three-dimensional microfluidic fuel cell architectures based on graphite rod electrodes." *Journal of Power Sources* 168.2 (2007), pp. 379–390. DOI: 10.1016/j.jpowsour.2007.02.087.

[34] D. G. Rackus, M. H. Shamsi, and A. R. Wheeler. "Electrochemistry, biosensors and microfluidics: a convergence of fields." *Chemical Society Reviews* 44.15 (2015), pp. 5320–5340. DOI: 10.1039/C4CS00369A.

[35] J. Wang. "Electrochemical detection for microscale analytical systems: a review." *Talanta* 56.2 (2002), pp. 223–231. DOI: 10.1016/S0039-9140(01)00592-6.

[36] J. Khandurina and A. Guttman. "Bioanalysis in microfluidic devices." *Journal of Chromatography A* 943.2 (2002), pp. 159–183. DOI: 10.1016/S0021-9673(01)01451-0.

[37] T. A. Webster and E. D. Goluch. "Electrochemical detection of pyocyanin in nanochannels with integrated palladium hydride reference electrodes." *Lab on a Chip* 12.24 (2012), pp. 5195–5201. DOI: 10.1039/C2LC40650K.

[38] E. Kjeang, B. Roesch, J. McKechnie, D. A. Harrington, N. Djilali, and D. Sinton. "Integrated electrochemical velocimetry for microfluidic devices." *Microfluidics and Nanofluidics* 3.4 (2006), pp. 403–416. DOI: 10.1007/s10404-006-0128-1.

[39] C. Amatore, M. Belotti, Y. Chen, E. Roy, C. Sella, and L. Thouin. "Using electrochemical coupling between parallel microbands for in situ monitoring of flow rates in microfluidic channels." *Journal of Electroanalytical Chemistry* 573.2 (2004), pp. 333–343. DOI: 10.1016/j.jelechem.2004.07.020.

[40] P. Watts and S. J. Haswell. "Microfluidic combinatorial chemistry." *Current Opinion in Chemical Biology* 7.3 (2003), pp. 380–387. DOI: 10.1016/S1367-5931(03)00050-4.

[41] S. M. MacDonald, J. D. Watkins, S. D. Bull, I. R. Davies, Y. Gu, K. Yunus, A. C. Fisher, P. C. B. Page, Y. Chan, C. Elliott, and F. Marken. "Two-phase flow electrosynthesis: Comparing N-octyl-2-pyrrolidone–aqueous and acetonitrile–aqueous three-phase boundary reactions." *Journal of Physical Organic Chemistry* 22.1 (2009), pp. 52–58. DOI: 10.1002/poc.1424.

[42] P. He, P. Watts, F. Marken, and S. J. Haswell. "Self-Supported and Clean One-Step Cathodic Coupling of Activated Olefins with Benzyl Bromide Derivatives in a Micro Flow Reactor." *Angewandte Chemie International Edition* 45.25 (2006), pp. 4146–4149. DOI: 10.1002/anie.200600951.

[43] O. Scialdone, C. Guarisco, A. Galia, G. Filardo, G. Silvestri, C. Amatore, C. Sella, and L. Thouin. "Anodic abatement of organic pollutants in water in micro reactors." *Journal of Electroanalytical Chemistry* 638.2 (2010), pp. 293–296. DOI: 10.1016/j.jelechem.2009.10.031.

[44] O. Scialdone, A. Galia, and S. Sabatino. "Electro-generation of H_2O_2 and abatement of organic pollutant in water by an electro-Fenton process in a microfluidic reactor." *Electrochemistry Communications* 26 (2013), pp. 45–47. DOI: 10.1016/j.elecom.2012.10.006.

[45] J. D. Holladay, E. O. Jones, M. Phelps, and J. Hu. "Microfuel processor for use in a miniature power supply." *Journal of Power Sources* 108.1 (2002), pp. 21–27. DOI: 10.1016/S0378-7753(01)01011-4.

[46] D. T. Whipple, E. C. Finke, and P. J. A. Kenis. "Microfluidic Reactor for the Electrochemical Reduction of Carbon Dioxide: The Effect of pH." *Electrochemical and Solid-State Letters* 13.9 (2010), B109–B111. DOI: 10.1149/1.3456590.

[47] I. Dumitrescu, D. F. Yancey, and R. M. Crooks. "Dual-electrode microfluidic cell for characterizing electrocatalysts." *Lab on a Chip* 12.5 (2012), pp. 986–993. DOI: 10.1039/C2LC21181E.

[48] M. J. Anderson and R. M. Crooks. "High-Efficiency Generation-Collection Microelectrochemical Platform for Interrogating Electroactive Thin Films." *Analytical Chemistry* 86.19 (2014), pp. 9962–9969. DOI: 10.1021/ac502869j.

[49] M. J. Anderson, N. Ostojic, and R. M. Crooks. "Microelectrochemical Flow Cell for Studying Electrocatalytic Reactions on Oxide-Coated Electrodes." *Analytical Chemistry* (2017). DOI: 10.1021/acs.analchem.7b03016. Online early access.

[50] E. B. Graper. "Evaporation characteristics of materials from an electron beam gun II." *Journal of Vacuum Science & Technology A: Vacuum, Surfaces, and Films* 5.4 (1987), pp. 2718–2723. DOI: 10.1116/1.574727.

[51] C. Metzner and B. Scheffel. "Special aspects concerning the electron beam deposition of multi-component alloys." *Surface and Coatings Technology* 146 (2001), pp. 491–497. DOI: 10.1016/S0257-8972(01)01460-8.

[52] M. T. Y. Paul, B. B. Yee, D. R. Bruce, and B. D. Gates. "Hexagonal Arrays of Cylindrical Nickel Microstructures for Improved Oxygen Evolution Reaction." *ACS Applied Materials & Interfaces* 9.8 (2017), pp. 7036–7043. DOI: 10.1021/acsami.6b14129.

[53] F. Tan, J. P. Metters, and C. E. Banks. "Electroanalytical applications of screen printed microelectrode arrays." *Sensors and Actuators B: Chemical* 181 (2013), pp. 454–462. DOI: 10.1016/j.snb.2013.02.034.

[54] F. E. Galdino, J. P. Smith, S. I. Kwamou, D. K. Kampouris, J. Iniesta, G. C. Smith, J. A. Bonacin, and C. E. Banks. "Graphite Screen-Printed Electrodes Applied for the Accurate and Reagentless Sensing of pH." *Analytical Chemistry* 87.23 (2015), pp. 11666–11672. DOI: 10.1021/acs.analchem.5b01236.

[55] J. Kim, X. Song, K. Kinoshita, M. Madou, and R. White. "Electrochemical Studies of Carbon Films from Pyrolyzed Photoresist." *Journal of The Electrochemical Society* 145.7 (1998), pp. 2314–2319. DOI: 10.1149/1.1838636.

[56] A. Singh, J. Jayaram, M. Madou, and S. Akbar. "Pyrolysis of Negative Photoresists to Fabricate Carbon Structures for Microelectromechanical Systems and Electrochemical Applications." *Journal of The Electrochemical Society* 149.3 (2002), E78–E83. DOI: 10.1149/1.1436085.

[57] L. M. Moretto, A. Mardegan, M. Cettolin, and P. Scopece. "Pyrolyzed Photoresist Carbon Electrodes for Trace Electroanalysis of Nickel(II)." *Chemosensors* 3.2 (2015), pp. 157–168. DOI: 10.3390/chemosensors3020157.

[58] D. A. Markov, E. M. Lillie, S. P. Garbett, and L. J. McCawley. "Variation in diffusion of gases through PDMS due to plasma surface treatment and storage conditions." *Biomedical Microdevices* 16.1 (2014), pp. 91–96. DOI: 10.1007/s10544-013-9808-2.

[59] P. N. Nge, C. I. Rogers, and A. T. Woolley. "Advances in Microfluidic Materials, Functions, Integration, and Applications." *Chemical Reviews* 113.4 (2013), pp. 2550–2583. DOI: 10.1021/cr300337x.

[60] K. Ren, J. Zhou, and H. Wu. "Materials for Microfluidic Chip Fabrication." *Accounts of Chemical Research* 46.11 (2013), pp. 2396–2406. DOI: 10.1021/ar300314s.

[61] K. Ren, W. Dai, J. Zhou, J. Su, and H. Wu. "Whole-Teflon microfluidic chips." *Proceedings of the National Academy of Sciences of the United States of America* 108.20 (2011), pp. 8162–8166. DOI: 10.1073/pnas.1100356108.

[62] N. Bhattacharjee, A. Urrios, S. Kang, and A. Folch. "The upcoming 3D-printing revolution in microfluidics." *Lab Chip* 16 (10 2016), pp. 1720–1742. DOI: 10.1039/C6LC00163G.

[63] S. Waheed, J. M. Cabot, N. P. Macdonald, T. Lewis, R. M. Guijt, B. Paull, and M. C. Breadmore. "3D printed microfluidic devices: enablers and barriers." *Lab Chip* 16 (11 2016), pp. 1993–2013. DOI: 10.1039/C6LC00284F.

[64] N. Markovic and P. N. Ross. "The effect of specific adsorption of ions and underpotential deposition of copper on the electro-oxidation of methanol on platinum single-crystal surfaces." *Journal of Electroanalytical Chemistry* 330.1 (1992), pp. 499–520. DOI: 10.1016/0022-0728(92)80327-Z.

[65] H. Kita, Y. Gao, T. Nakato, and H. Hattori. "Effect of hydrogen sulphate ion on the hydrogen ionization and methanol oxidation reactions on platinum single-crystal electrodes." *Journal of Electroanalytical Chemistry* 373.1 (1994), pp. 177–183. DOI: 10.1016/0022-0728(94)03314-5.

[66] W. L. Robb. "Thin Silicone Membranes–Their Permeation Properties and Some Applications." *Annals of the New York Academy of Sciences* 146.1 (1968), pp. 119–137. DOI: 10.1111/j.1749-6632.1968.tb20277.x.

[67] J. P. Montoya. *Membrane Gas Exchange. Using Hollow Fiber Membranes to Separate Gases from Liquid and Gaseous Streams*. White Paper. MedArray, Inc., 2010. URL: https://www.permselect.com/membranes (visited on 2017-10-01).

[68] P. He. "Conversion of Staircase Voltammetry to Linear Sweep Voltammetry by Analog Filtering." *Analytical Chemistry* 67.5 (1995), pp. 986–992. DOI: 10.1021/ac00101a029.

[69] B. Hai, Y. V. Tolmachev, K. A. Loparo, C. Zanelli, and D. Scherson. "Cyclic versus Staircase Voltammetry in Electrocatalysis: Theoretical Aspects." *Journal of The Electrochemical Society* 158.2 (2011), F15–F19. DOI: 10.1149/1.3512914.

[70] M. Ingdal. "Micro-fluidic flow cells for studies of electrochemical reactions." MA thesis. Norwegian University of Science and Technology, NTNU, 2014.

[71] T. Holm, M. Ingdal, E. V. Fanavoll, S. Sunde, F. Seland, and D. A. Harrington. "Mass-transport impedance at channel electrodes: accurate and approximate solutions." *Electrochimica Acta* 202 (2016), pp. 84–89. DOI: 10.1016/j.electacta.2016.03.096.

[72] T. Holm, M. Ingdal, J. R. Strobl, E. V. Fanavoll, S. Sunde, F. Seland, and D. A. Harrington. "Generator-Sensor Impedance at Double Channel Electrodes." *Electrochimica Acta* 229 (2017), pp. 452–457. DOI: 10.1016/j.electacta.2017.01.075.

[73] P. Vanýsek. "Electrochemical series." In: *CRC Handbook of Chemistry and Physics, 98th Edition (Internet Version 2018)*. Ed. by J. R. Rumble. Boca Raton, FL: CRC Press/Taylor and Francis, 2017.

[74] A. B. Ofstad, M. S. Thomassen, J. L. Gomez de la Fuente, F. Seland, S. Møller-Holst, and S. Sunde. "Assessment of Platinum Dissolution from a Pt/C Fuel Cell Catalyst: An Electrochemical Quartz Crystal Microbalance Study." *Journal of the Electrochemical Society* 157.5 (2010), B621–B627. DOI: 10.1149/1.3327890.

[75] B. Conway. "Electrochemical oxide film formation at noble metals as a surface-chemical process." *Progress in Surface Science* 49.4 (1995), pp. 331–452. DOI: 10.1016/0079-6816(95)00040-6.

[76] G. Jerkiewicz, G. Vatankhah, J. Lessard, M. P. Soriaga, and Y.-S. Park. "Surface-oxide growth at platinum electrodes in aqueous H_2SO_4: Reexamination of its mechanism through combined cyclic-voltammetry, electrochemical quartz-crystal nanobalance, and Auger electron spectroscopy measurements." *Electrochimica Acta* 49.9 (2004), pp. 1451–1459. DOI: 10.1016/j.electacta.2003.11.008.

[77] D. Pletcher, R. Greff, R. Peat, L. Peter, and J. Robinson. Woodhead Publishing, 2011. Chap. 6, 11, pp. 206, 368. ISBN: 978-1-898563-80-8.

[78] S. Trasatti and O. Petrii. "Real surface area measurements in electrochemistry." *Journal of Electroanalytical Chemistry* 327.1 (1992), pp. 353–376. DOI: 10.1016/0022-0728(92)80162-W.

[79] T. Biegler, D. Rand, and R. Woods. "Limiting oxygen coverage on platinized platinum; Relevance to determination of real platinum area by hydrogen adsorption." *Journal of Electroanalytical Chemistry and Interfacial Electrochemistry* 29.2 (1971), pp. 269–277. DOI: 10.1016/S0022-0728(71)80089-X.

[80] J. Bett, K. Kinoshita, K. Routsis, and P. Stonehart. "A comparison of gas-phase and electrochemical measurements for chemisorbed carbon monoxide and hydrogen on platinum crystallites." *Journal of Catalysis* 29.1 (1973), pp. 160–168. DOI: 10.1016/0021-9517(73)90214-5.

[81] G. G. Barna, S. N. Frank, and T. H. Teherani. "A Scan Rate Dependent Determination of Platinum Areas." *Journal of The Electrochemical Society* 129.4 (1982), pp. 746–749. DOI: 10.1149/1.2123963.

[82] M. Grdeń, M. Łukaszewski, G. Jerkiewicz, and A. Czerwiński. "Electrochemical behaviour of palladium electrode: Oxidation, electrodissolution and ionic adsorption." *Electrochimica Acta* 53.26 (2008), pp. 7583–7598. DOI: 10.1016/j.electacta.2008.05.046.

[83] L.-L. Fang, Q. Tao, M.-F. Li, L.-W. Liao, D. Chen, and Y.-X. Chen. "Determination of the Real Surface Area of Palladium Electrode." *Chinese Journal of Chemical Physics* 23.5 (2010), p. 543. DOI: 10.1088/1674-0068/23/05/543-548.

[84] A. Czerwiński. "The adsorption of carbon oxides on a palladium electrode from acidic solution." *Journal of Electroanalytical Chemistry* 379.1 (1994), pp. 487–493. DOI: 10.1016/0022-0728(94)87173-6.

[85] M. Shao, J. H. Odell, S.-I. Choi, and Y. Xia. "Electrochemical surface area measurements of platinum- and palladium-based nanoparticles." *Electrochemistry Communications* 31 (2013), pp. 46–48. DOI: 10.1016/j.elecom.2013.03.011.

[86] S. Henning, J. Herranz, and H. A. Gasteiger. "Bulk-Palladium and Palladium-on-Gold Electrocatalysts for the Oxidation of Hydrogen in Alkaline Electrolyte." *Journal of The Electrochemical Society* 162.1 (2015), F178–F189. DOI: 10.1149/2.1081501jes.

[87] T. Holm, S. Sunde, F. Seland, and D. A. Harrington. "A semianalytical method for simulating mass transport at channel electrodes." *Journal of Electroanalytical Chemistry* 745 (2015), pp. 72–79. DOI: doi.org/10.1016/j.jelechem.2015.03.019.

[88] C. J. Geankoplis. *Transport Processes and Separation Process Principles: Includes Unit Operations*. 4th ed. Prentice Hall Professional technical reference. Prentice Hall Professional Technical Reference, 2003, p. 52. ISBN: 0-13-101367-X.

[89] K. V. Sharp, R. J. Adrian, J. G. Santiago, and J. I. Molho. "Liquid Flows in Microchannels." In: *MEMS: Introduction and Fundamentals*. Ed. by M. Gad-el-Hak. The CRC Press Series in Mechanical and Aerospace Engineering. CRC Press, 2005. Chap. 10, pp. 10-1–10-53. ISBN: 978-0-8493-9137-8.

[90] H. Bruus. "Governing Equations in Microfluidics." In: *Microscale Acoustofluidics*. Ed. by T. Laurell and A. Lenshof. The Royal Society of Chemistry, 2015. Chap. 1, p. 13. ISBN: 978-1-84973-671-8. DOI: 10.1039/9781849737067-00001.

[91] H. Bruus. *Theoretical Microfluidics*. Oxford: Oxford University Press, 2008. Chap. 2, pp. 48–51. ISBN: 978-0-19-923508-7.

[92] J. A. Cooper and R. G. Compton. "Channel Electrodes — A Review." *Electroanalysis* 10.3 (1998), pp. 141–155. DOI: 10.1002/(SICI)1521-4109(199803)10:3<141::AID-ELAN141>3.0.CO;2-F.

[93] V. G. Levich. *Physicochemical hydrodynamics*. Prentice-Hall international series in the physical and chemical engineering sciences. Englewood Cliffs, NJ: Prentice-Hall, 1962. ISBN: 978-0136744405.

[94] C. M. Brett and A. M. C. O. Brett. "Hydrodynamic Electrodes." In: *Electrode Kinetics: Principles and Methodology*. Ed. by C. Bamford and R. Compton. Vol. 26. Comprehensive Chemical Kinetics. Elsevier Science Publishers B.V., 1986. Chap. 5. ISBN: 0-444-42550-0. DOI: 10.1016/S0069-8040(08)70029-3.

[95] *Microstepping Tutorial*. Technical report. Zaber Technologies Inc, 2014. URL: https://www.zaber.com/microstepping-tutorial (visited on 2017-10-01).

[96] N.-T. Nguyen and Z. Wu. "Micromixers—a review." *Journal of Micromechanics and Microengineering* 15.2 (2005), R1. DOI: 10.1088/0960-1317/15/2/R01.

[97] C. H. Hamann, A. Hamnett, and W. Vielstich. *Electrochemistry*. Wiley, 2007, p. 93. ISBN: 978-3-527-31069-2.

[98] N. M. Contento and P. W. Bohn. "Electric field effects on current-voltage relationships in microfluidic channels presenting multiple working electrodes in the weak-coupling limit." *Microfluidics and Nanofluidics* 18.1 (2014), pp. 131–140. DOI: 10.1007/s10404-014-1424-9.

[99] E. Bitziou, M. E. Snowden, M. B. Joseph, S. J. Leigh, J. A. Covington, J. V. Macpherson, and P. R. Unwin. "Dual electrode micro-channel flow cell for redox titrations: Kinetics and analysis of homogeneous ascorbic acid oxidation." *Journal of Electroanalytical Chemistry* 692 (2013), pp. 72–79. DOI: 10.1016/j.jelechem.2012.12.014.

[100] C. Bonnaud, I. Billard, N. Papaiconomou, E. Chainet, and J. C. Lepretre. "Rationale for the implementation of reference electrodes in ionic liquids." *Physical Chemistry Chemical Physics (PCCP)* 18.11 (2016), pp. 8148–8157. DOI: 10.1039/C5CP07652H.

[101] N. M. Contento, S. P. Branagan, and P. W. Bohn. "Electrolysis in nanochannels for in situ reagent generation in confined geometries." *Lab on a Chip* 11.21 (2011), pp. 3634–3641. DOI: 10.1039/C1LC20570F.

[102] H. Yang, S. K. Kang, C. A. Choi, H. Kim, D.-H. Shin, Y. S. Kim, and Y. T. Kim. "An iridium oxide reference electrode for use in microfabricated biosensors and biochips." *Lab on a Chip* 4.1 (2004), pp. 42–46. DOI: 10.1039/B309899K.

[103] B. J. Polk, A. Stelzenmuller, G. Mijares, W. MacCrehan, and M. Gaitan. "Ag/AgCl microelectrodes with improved stability for microfluidics." *Sensors and Actuators B: Chemical* 114.1 (2006), pp. 239–247. DOI: 10.1016/j.snb.2005.03.121.

[104] J. Schnitker, D. Afanasenkau, B. Wolfrum, and A. Offenhäusser. "Planar reference electrodes on multielectrode arrays for electrochemical measurements of ionic currents." *Physica Status Solidi A* 210.5 (2013), pp. 892–897. DOI: 10.1002/pssa.201200850.

[105] T. Matsumoto, A. Ohashi, and N. Ito. "Development of a micro-planar Ag/AgCl quasi-reference electrode with long-term stability for an amperometric glucose sensor." *Analytica Chimica Acta* 462.2 (2002), pp. 253–259. DOI: 10.1016/S0003-2670(02)00334-3.

[106] A. Yakushenko, D. Mayer, J. Buitenhuis, A. Offenhausser, and B. Wolfrum. "Electrochemical artifacts originating from nanoparticle contamination by Ag/AgCl quasi-reference electrodes." *Lab on a Chip* 14.3 (2014), pp. 602–607. DOI: 10.1039/C3LC51029H.

[107] I.-Y. Huang and R.-S. Huang. "Fabrication and characterization of a new planar solid-state reference electrode for {ISFET} sensors." *Thin Solid Films* 406.1–2 (2002), pp. 255–261. DOI: 10.1016/S0040-6090(01)01783-7.

[108] G. Inzelt. "Pseudo-reference Electrodes." In: *Handbook of Reference Electrodes*. Ed. by G. Inzelt, A. Lewenstam, and F. Scholz. Berlin, Heidelberg: Springer, 2013, pp. 331–332. ISBN: 978-3-642-36188-3. DOI: 10.1007/978-3-642-36188-3.

[109] E. V. Dydek, M. V. Petersen, D. G. Nocera, and K. F. Jensen. "Electrode Placement and Fluid Flow Rates in Microfluidic Electrochemical Devices." *Journal of the Electrochemical Society* 159.11 (2012), H853–H856. DOI: 10.1149/2.007211jes.

[110] J. Zhou, K. Ren, Y. Zheng, J. Su, Y. Zhao, D. Ryan, and H. Wu. "Fabrication of a microfluidic Ag/AgCl reference electrode and its application for portable and disposable electrochemical microchips." *Electrophoresis* 31.18 (2010), pp. 3083–3089. DOI: 10.1002/elps.201000113.

[111] J. S. Mayell and S. H. Langer. "Effect of dilute chloride ion on platinum electrodes." *Journal of Electroanalytical Chemistry* 7.4 (1964), pp. 288–296. DOI: 10.1016/0022-0728(64)80102-9.

[112] J. Bittles and E. Littauer. "Anodic corrosion and passivation of Pt in Cl-solutions." *Corrosion Science* 10.1 (1970), pp. 29–41. DOI: 10.1016/S0010-938X(70)80095-6.

[113] E. Iannone. *Labs on Chip: Principles, Design and Technology*. CRC Press, 2014, p. 857. ISBN: 978-1-4665-6073-4.

[114] H. Thomas, R. Heide, and A. Terfort. "Thin film reference electrodes for aqueous and organic media." *Sensors and Actuators B: Chemical* 171–172 (2012), pp. 155–164. DOI: 10.1016/j.snb.2012.02.071.

[115] M. W. Shinwari, D. Zhitomirsky, I. A. Deen, P. R. Selvaganapathy, M. J. Deen, and D. Landheer. "Microfabricated Reference Electrodes and their Biosensing Applications." *Sensors* 10.3 (2010), p. 1679. DOI: 10.3390/s100301679.

[116] F. D. Manchester, A. San-Martin, and J. M. Pitre. "The H-Pd (hydrogen-palladium) System." *Journal of Phase Equilibria* 15.1 (1994), pp. 62–83. DOI: 10.1007/BF02667685.

[117] A. J. Bard, R. Parsons, and J. Jordan. *Standard Potentials in Aqueous Solution*. Monographs in Electroanalytical Chemistry and Electrochemistr. Taylor & Francis, 1985. ISBN: 9780824772918.

[118] D. J. G. Ives and G. J. Janz. *Reference electrodes, theory and practice.* Academic Press, 1961, pp. 112–116. DOI: 10.1021/ed039pA134.

[119] T. Imokawa, K.-J. Williams, and G. Denuault. "Fabrication and Characterization of Nanostructured Pd Hydride pH Microelectrodes." *Analytical Chemistry* 78.1 (2006), pp. 265–271. DOI: 10.1021/ac051328j.

[120] L. Nyholm. "Electrochemical techniques for lab-on-a-chip applications." *Analyst* 130.5 (2005), pp. 599–605. DOI: 10.1039/B415004J.

[121] M. Pumera, A. Merkoçi, and S. Alegret. "New materials for electrochemical sensing VII. Microfluidic chip platforms." *Trends in Analytical Chemistry* 25.3 (2006), pp. 219–235. DOI: 10.1016/j.trac.2005.08.005.

[122] R. S. Martin, P. D. Root, and D. M. Spence. "Microfluidic technologies as platforms for performing quantitative cellular analyses in an in vitro environment." *Analyst* 131.11 (2006), pp. 1197–1206. DOI: 10.1039/B611041J.

[123] "Electrical Conductivity of Aqueous Solutions." In: *CRC Handbook of Chemistry and Physics, 98th Edition (Internet Version 2018)*. Ed. by J. R. Rumble. Boca Raton, FL: CRC Press/Taylor and Francis, 2017.

[124] S. P. Forry, J. R. Murray, M. L. A. V. Heien, L. E. Locascio, and R. M. Wightman. "Probing Electric Fields Inside Microfluidic Channels during Electroosmotic Flow with Fast-Scan Cyclic Voltammetry." *Analytical Chemistry* 76.17 (2004), pp. 4945–4950. DOI: 10.1021/ac049591s.

[125] A. Bîrzu, J. Coleman, and I. Z. Kiss. "Highly disparate activity regions due to non-uniform potential distribution in microfluidic devices: Simulations and experiments." *Journal of Electroanalytical Chemistry* 726 (2014), pp. 27–35. DOI: 10.1016/j.jelechem.2014.05.002.

[126] *About Lock-In Amplifiers*. Application Note. Stanford Research Systems. URL: http://www.thinksrs.com/support/app.htm (visited on 2017-10-01).

[127] T. Iwasita, F. C. Nart, and W. Vielstich. "An FTIR Study of the Catalytic Activity of a 85:15 Pt:Ru Alloy for Methanol Oxidation." *Berichte der Bunsengesellschaft für physikalische Chemie* 94.9 (1990), pp. 1030–1034. DOI: 10.1002/bbpc.19900940930.

[128] P. Christensen, A. Hamnett, J. Munk, and G. Troughton. "An in situ FTIR study of the electrochemical oxidation of methanol at small platinum particles." *Journal of Electroanalytical Chemistry* 370.1 (1994), pp. 251–258. DOI: 10.1016/0022-0728(93)03168-O.

[129] J. Munk, P. Christensen, A. Hamnett, and E. Skou. "The electrochemical oxidation of methanol on platinum and platinum + ruthenium particulate electrodes studied by in-situ FTIR spectroscopy and electrochemical mass spectrometry." *Journal of Electroanalytical Chemistry* 401.1 (1996), pp. 215–222. DOI: 10.1016/0022-0728(95)04314-4.

[130] T. Yajima, H. Uchida, and M. Watanabe. "I-Situ ATR-FTIR Spectroscopic Study of Electro-oxidation of Methanol and Adsorbed CO at Pt-Ru Alloy." *The Journal of Physical Chemistry B* 108.8 (2004), pp. 2654–2659. DOI: 10.1021/jp037215q.

[131] H. Wang, T. Löffler, and H. Baltruschat. "Formation of intermediates during methanol oxidation: A quantitative DEMS study." *Journal of Applied Electrochemistry* 31.7 (July 2001), pp. 759–765. DOI: 10.1023/A:1017539411059.

[132] H. Wang, C. Wingender, H. Baltruschat, M. Lopez, and M. Reetz. "Methanol oxidation on Pt, PtRu, and colloidal Pt electrocatalysts: a DEMS study of product formation." *Journal of Electroanalytical Chemistry* 509.2 (2001), pp. 163–169. DOI: 10.1016/S0022-0728(01)00531-9.

[133] Z. Jusys and R. J. Behm. "Methanol Oxidation on a Carbon-Supported Pt Fuel Cell Catalyst – A Kinetic and Mechanistic Study by Differential Electrochemical Mass Spectrometry." *The Journal of Physical Chemistry B* 105.44 (2001), pp. 10874–10883. DOI: 10.1021/jp011510y.

[134] Z. Jusys, J. Kaiser, and R. Behm. "Composition and activity of high surface area PtRu catalysts towards adsorbed CO and methanol electrooxidation – A DEMS study." *Electrochimica Acta* 47.22 (2002), pp. 3693–3706. DOI: 10.1016/S0013-4686(02)00339-0.

[135] D. E. Bidstrup and C. J. Geankoplis. "Aqueous Molecular Diffusivities of Carboxylic Acids." *Journal of Chemical & Engineering Data* 8.2 (1963), pp. 170–173. DOI: 10.1021/je60017a004.

[136] A. Capon and R. Parsons. "The oxidation of formic acid on noble metal electrodes. Part 2. A comparison of the behaviour of pure electrodes." *Journal of Electroanalytical Chemistry and Interfacial Electrochemistry* 44.2 (1973), pp. 239–254. DOI: 10.1016/S0022-0728(73)80250-5.

[137] A. Capon and R. Parsons. "The oxidation of formic acid on noble metal electrodes. Part 4. Platinum + palladium alloys." *Journal of Electroanalytical Chemistry and Interfacial Electrochemistry* 65.1 (1975), pp. 285–305. DOI: 10.1016/0368-1874(75)85124-0.

[138] A. Pavese, V. Solis, and M. Giordano. "Oxidation of formic acid on palladium anodes in acidic medium. Effect of Pd(II) ions." *Electrochimica Acta* 32.8 (1987), pp. 1213–1216. DOI: 10.1016/0013-4686(87)80037-3.

[139] V. Solis, T. Iwasita, A. Pavese, and W. Vielstich. "Investigation of formic acid oxidation on palladium in acidic solutions by on-line mass spectroscopy." *Journal of Electroanalytical Chemistry and Interfacial Electrochemistry* 255.1 (1988), pp. 155–162. DOI: 10.1016/0022-0728(88)80011-1.

[140] A. Pavese, V. Solis, and M. Giordano. "Electrocatalytic oxidation of formic acid on Pd + Pt alloys of different bulk composition in acidic medium." *Journal of Electroanalytical Chemistry and Interfacial Electrochemistry* 245.1 (1988), pp. 145–156. DOI: 10.1016/0022-0728(88)80066-4.

[141] A. Pavese and V. Solís. "Comparative investigation of formic acid and formaldehyde oxidation on palladium by a rotating ring-disc electrode and on-line mass spectroscopy in acidic solutions." *Journal of Electroanalytical Chemistry and Interfacial Electrochemistry* 301.1 (1991), pp. 117–127. DOI: 10.1016/0022-0728(91)85463-Y.

[142] M. I. Manzanares, A. G. Pavese, and V. M. Solis. "Comparative investigation of formic acid and formaldehyde electro-oxidation on palladium in acidic medium." *Journal of Electroanalytical Chemistry and Interfacial Electrochemistry* 310.1 (1991), pp. 159–167. DOI: 10.1016/0022-0728(91)85259-R.

[143] D. Rand and R. Woods. "A study of the dissolution of platinum, palladium, rhodium and gold electrodes in 1 M sulphuric acid by cyclic voltammetry." *Journal of Electroanalytical Chemistry and Interfacial Electrochemistry* 35.1 (1972), pp. 209–218. DOI: 10.1016/S0022-0728(72)80308-5.

[144] S. H. Cadle. "Ring-Disk Electrode Study of Palladium Dissolution." *Journal of The Electrochemical Society* 121.5 (1974), pp. 645–648. DOI: 10.1149/1.2401877.

[145] F. Seland, D. A. Harrington, and R. Tunold. "Fast methanol oxidation on polycrystalline Pt." *Electrochimica Acta* 52.3 (2006), pp. 773–779. DOI: 10.1016/j.electacta.2006.06.010.

List of Tables

List of Figures